



NRL/MR/6720--99-8341

Advanced Radiation Theory Support Annual Report 1998, Final Report

*Radiation Hydrodynamics Branch
Plasma Physics Division*

April 27, 1999

19990512 005

Approved for public release; distribution unlimited.

REPORT DOCUMENTATION PAGE			Form Approved OMB No. 0704-0188	
Public reporting burden for this collection of information is estimated to average 1 hour per response, including the time for reviewing instructions, searching existing data sources, gathering and maintaining the data needed, and completing and reviewing the collection of information. Send comments regarding this burden estimate or any other aspect of this collection of information, including suggestions for reducing this burden, to Washington Headquarters Services, Directorate for Information Operations and Reports, 1215 Jefferson Davis Highway, Suite 1204, Arlington, VA 22202-4302, and to the Office of Management and Budget, Paperwork Reduction Project (0704-0188), Washington, DC 20503.				
1. AGENCY USE ONLY (Leave Blank)	2. REPORT DATE April 27, 1999	3. REPORT TYPE AND DATES COVERED Final Report		
4. TITLE AND SUBTITLE Advanced Radiation Theory Support Annual Report 1998, Final Report			5. FUNDING NUMBERS	
6. AUTHOR(S) Radiation Hydrodynamics Branch				
7. PERFORMING ORGANIZATION NAME(S) AND ADDRESS(ES) Naval Research Laboratory Washington, DC 20375-5320			8. PERFORMING ORGANIZATION REPORT NUMBER NRL/MR/6720-99-8341	
9. SPONSORING/MONITORING AGENCY NAME(S) AND ADDRESS(ES) Defense Threat Reduction Agency 6801 Telegraph Road Alexandria, VA 22310			10. SPONSORING/MONITORING AGENCY REPORT NUMBER	
11. SUPPLEMENTARY NOTES This research was sponsored by the Defense Threat Reduction Agency under Job Order Titles, "Advanced Radiation Theory Support," MIPR No. 98-2051, "Multi-Shell PRS Theory Development," MIPR No. 98-2174-923.				
12a. DISTRIBUTION/AVAILABILITY STATEMENT Approved for public release; distribution unlimited.			12b. DISTRIBUTION CODE A	
13. ABSTRACT (Maximum 200 words) This report describes the work of the Radiation Hydrodynamics Branch during FY 98 in support of the DTRA PRS program. Critical issues covered are: (1) Large initial radius Z-pinch load behavior on Saturn, Double Eagle, DECADE QUAD, and Z pulsed power machines, (2) Analyzing temperature and density radial temperature gradients in Z-pinch plasmas, (3) Analysis of time resolved and time integrated Z-pinch data, (4) Spectroscopic PRS analysis, (5) Radiation magneto-hydrodynamic code development and assessment, (6) Analysis of nested wire array loads, and (7) Basic tradeoffs of L-shell versus K-shell radiators.				
14. SUBJECT TERMS Decade Quad Radiation MHD Transport coefficients			15. NUMBER OF PAGES 152	
Z-pinch physics Plasma radiation source Large radius implosions			16. PRICE CODE	
Rayleigh-Taylor instability Diagnostic line ratios Long time implosions				
17. SECURITY CLASSIFICATION OF REPORT UNCLASSIFIED	18. SECURITY CLASSIFICATION OF THIS PAGE UNCLASSIFIED	19. SECURITY CLASSIFICATION OF ABSTRACT UNCLASSIFIED	20. LIMITATION OF ABSTRACT UL	

CONTENTS

Executive Summary	v
I. Large Radius Implosions: Planning, Diagnosing and Evaluating	1
II. Detailed Analysis of Aluminum Pinches Driven by the Z Generator	27
III. Plasma Spectroscopy of Pulsed Power Driven Z-pinch Titanium Plasmas	57
IV. Decade Quad Load Performance Assessment	69
V. Wire Dynamics Model with Application to Nested Arrays	89
VI. Two-Dimensional Simulations	119
VII. D-T Fusion in 40 and 60 MA Z-Pinches	125

EXECUTIVE SUMMARY

This report describes the theory support of DSWA's Plasma Radiation Source (PRS) program carried out by NRL's Radiation Hydrodynamics Branch (Code 6720) in FY 1998. Included is work called for in MIPR 98-2051, 6720 Radiation Theory Support.

In addition to its BREMS usage, DTRA began the DECADE program with the intention of using the BREMS-designed DECADE accelerator to drive a PRS load. This option originally envisioned that an inductive storage machine, which employs a plasma opening switch (POS) to provide a fast rise time current pulse, be used to implode conventional small radius PRS loads. Because the POS has been unable to perform its task, this put BREMS usage at risk and imperiled the PRS program. However to achieve DTRA's longstanding PRS goals, it was recognized early on in NRL's theory program (see for example, NRL memorandum 6722-94-7459) that minimizing electrical stresses in more powerful machines will require scaling to longer implosion time and larger radius loads. In turn, larger radii loads raise the issue of having adequate current to offset the problems of increased asymmetry and instability that otherwise arise at large radius. These problems are just now beginning to be addressed and resolved. It was decided by DTRA, in an effort to use its preexisting DECADE hardware, to begin investigating the feasibility of driving PRS loads with long risetime current pulses that do not require a POS, and that can, therefore, deliver their energy to a PRS load rather than to the POS. Using the preexisting DECADE hardware may not be the optimal machine design for managing the tradeoff between electrical stress and energy delivery to achieve optimal load performance at large radius (Decade is a 300 ns risetime machine; a 200 ns machine would have been lower risk). However it was recognized by Code 6720 and DTRA that this decision would be a step in the right direction. The DOE community is also interested in optimizing the performance of long current risetime implosions because a better understanding of the tradeoffs involved with having the ability to couple large amounts of energy into a PRS load while minimizing electrical stresses is an essential design consideration for the next generation of pulsed power machines.

In order to utilize the available stored energy in a long pulse machine like DECADE or DECADE QUAD, it is necessary to implode from much larger radii than have been utilized

conventionally in the past. In this regard, Code 6720 has focussed its efforts over the last several years on analyzing and evaluating the results of experiments on existing machines with a special emphasis on evaluating the feasibility of increasing x-ray yields and improving simulation fidelity using large radius PRS loads. Mainly, the data clearly show that one must go up in peak current if one is to successfully go out in radius. This report describes some of the progress that was made this year in proceeding along the path towards achieving these yield and fidelity goals at large radius with judicious guidance being provided by proper experiments, diagnostics, and analysis. The analyses have relied on theoretical ideas that have been developed over the years and that serve as a foundation for interpreting and designing experiments. In this report the subjects discussed are, section by section:

(1) If PRS loads are to perform effectively at large radii, then certain minimum load requirements on the generator and load designs must be met. Some of these requirements are known and some need to be discovered. The load design discoveries that were made this year from titanium wire experiments on the Sandia National Laboratory Z facility are described. In general the trends observed in these experiments are in accord with the theoretical guidance upon which they were based. The results from these experiments, which were 2 cm in initial radius, should help dispel one of the long-standing myths in this field; namely, that large radius loads are too unstable to implode successfully, where success in this discussion is defined in terms of kilovolt x-ray output and not in terms of the degree of cylindrical-ness of the pinch. The best yield of 125 kJ of K-shell x rays at 4.7 to 6 KeV were obtained from a titanium shot, that was only barely able to reach the theoretically required implosion. This experimental impediment should be removed in the future.

Because the initial mass distribution of a wire array is well characterized, and initially symmetric, Code 6720 has been a strong advocate of employing wire arrays as opposed to gas puffs to assess experimentally the consequences of going to larger radii loads. In this regard, we have been promoting the use of molybdenum L-shell emitting wire arrays as an intermediate load that produces high energy photons that lie between the K shells of aluminum and argon. General theoretical guidelines for designing L-shell radiating loads are described and employed in the design of Molybdenum experiments. The results from the molybdenum Double eagle experiments demonstrated the success of these guidelines, showing that we could successfully predict where

the kilovolt yield could be optimized as a function of load mass. They also indicated the need for a similar set of experiments on the higher current Saturn machine, where higher velocity implosions could be achieved. The design for these future molybdenum Saturn experiments is proposed.

A recent analysis of the Saturn variable-mass and variable-radius, high wire number, series of experiments is described that confirms the accuracy of the original K-shell yield scaling predictions made by Code 6720. This analysis also reveals the necessity, by way of the K-shell yield, of keeping the wire number high in order to achieve as high a symmetry during the implosion as possible. In particular, the variable-radius experiments demonstrated that one could go out in radius successfully on a short risetime machine such as Saturn if the wire number was kept large enough.

(2) In this section, a methodology is described whereby a one-dimensional, cylindrical plasma, Collisional Radiative Equilibrium (CRE) model containing detailed configuration atomic structure for the Li-, He-, and H-like ionic stages of Al and Mg is used to infer the electron temperature and ion density profiles that were present during stagnation in Al/Mg mixture experiments that were performed on the Z machine. We have evolved the state-of-the-art of this methodology over the years from initially inferring only a radially averaged density and temperature to the point where now radial gradients in temperature and density can be inferred from a stagnated Z-pinch plasma. This methodology continues to evolve and has increasingly become an important diagnostic tool for quantitatively exploring Z-pinch behavior. Applying this methodology to the Al/Mg Z experiments reveals the increasing roles that opacity and gradient structure play in affecting K-shell emission as the load mass is necessarily increased for high current (19 MA) machines like Z. The experimental radial density and temperature information ascertained by this methodology is justifiably promoted as a means of benchmarking and improving multidimensional radiative magneto-hydrodynamic calculations. This analysis technique also demonstrates the valuable extra diagnostic information obtained with two elements present in the load emitting a richer x-ray spectrum than a single element plasma.

(3) It is important to know the the limits of validity of an ionization dynamics and/or radiation transport model when it is used in a calculation to analyze experimental Z-pinch results. To help

clarify this validity issue, numerical simulations are carried out to compare K- and L-shell soft x-ray emission as a function of the ionization dynamic model. The compared models include: (1) a time- dependent non-equilibrium (NEQ) model, (2) a CRE model, and (3) a Local Thermodynamic Equilibrium (LTE) model. For all three ionization dynamic models, both an optically thin and an optically thick (probability of escape) calculation are performed. Because the optically thick NEQ model is the most comprehensive of the three, its results are used for assessing the validity of the other models. This analysis is performed by simulating a titanium experiment on the Z machine. The ionization dynamic comparison reveals that the radiative emission and atomic populations of the titanium plasma are strongly non-LTE. Results are presented for the total and K-shell radiation yields, and emission spectra as a function of photon energy.

(4) In this section we evaluate the future performance on DECADE QUAD of the large radius argon loads that have been developed for Double Eagle and Saturn. These are evolutionary loads in that the knowledge attained from their usage on Double Eagle and Saturn will allow us to mitigate the risks associated with large radius implosions and to ultimately design loads that make DECADE QUAD a successful argon PRS machine. In particular, the 7 cm diameter uniform fill loads used in the Double Eagle and Saturn long pulse experiments are assessed in terms of their future performance on DECADE QUAD. This assessment is accomplished by projecting DECADE QUAD argon K-shell yields by scaling up in energy from the experimental Saturn and Double Eagle yields. This projection is conservative, in the sense that the loads may well be in a regime where the yield scales as energy squared, and it eliminates numerous questionable model dependences that are typically present when making predictions of a future machines performance. It should be very encouraging to the PRS community that the Double Eagle long pulse argon K-shell yields scales with energy to over 40 kJ of K-shell emission on DECADE QUAD. Future large radius experiments on Saturn and Double Eagle are proposed and discussed.

(5) X-ray powers from tungsten Z-pinch loads have been increased by employing nested wire array configurations as opposed to single arrays. Two dimensional r-z radiation MHD modeling of the Rayleigh Taylor instability for nested wire implosions on Z captured some of the dynamics and trends observed in power increase and pulsewidth decrease. However, these 2-D codes are unable to qualitatively predict the observed trend that optimal x-ray power occurred when the inner array

had less mass than the outer array. A plausible reason for this inability is that the fluid codes do not allow the mass from the outer array to interpenetrate the mass of the inner array. In addition, they do not account for the current commutation that takes place as the outer array overtakes and then interpenetrates the inner array. To begin to model these effects, we have developed wire dynamics models (WDM) that treat the individual wire segments of an array load as a self-consistent electrical and mechanical ensemble. The nested wire array is likely to be an important PRS design option that allows us to move further out in initial load radius in order to take full advantage of the energy reservoirs of DECADE and DECADE QUAD. For this reason the WDM is a valuable tool that will aid us in understanding the general dynamics of nested wire array implosions. In this section the WDM model is discussed in conjunction with an analysis of the nested wire array shots on Z.

(6) Our two-dimensional radiation MHD code, PRISM, has been used extensively in the past to study novel load designs, the Rayleigh-Taylor instability, zippering, and non-uniform gas puff distributions. The radiation transport model employed in these earlier studies assumed that either the plasma is transparent to radiation or that a local probability of escape model can be used to model some of the self-absorption physics. This year, in an effort to upgrade our 2D radiation transport capabilities, we included a radiation diffusion model into PRISM. This method works well in both the LTE limit and in the thin limit but has problems in the regime between the two extremes. Unlike the DOE models, which advance a radiation temperature, we obtained the radiation energy density using the Code 6720 atomic physics tables. These tables predict energy densities that are more indicative of typical Z-pinch collisional radiative conditions as opposed to radiation temperature LTE based conditions. In section 6, we describe the radiation diffusion transport features that have recently been added to PRISM. Also discussed are PRISM model results for Double Eagle in the long pulse mode.

(7) With the "Z" facility operational and the expectation of even more powerful Z-pinch devices in the future, there is renewed interest in exploring the feasibility of creating nuclear fusion conditions in a Z-pinch. Experiments performed on Sandia's Saturn facility (7-8 MA) produced up to 3×10^{12} neutrons. For peak currents in excess of Z's 20 MAs, the magnetic field may be sufficient to confine the α particles. In this section we examine theoretically a number of configurations which might be employed to produce D-T fusion using next generation 20, 40, and 60 MA pulsed power machines.

The designs consist of a pure D-T shell, a D-T shell combined with a CH pusher, and a D-T shell combined with a CH pusher and a magnetic interlayer. This analysis represents the beginnings of a foundation upon which future direct drive Z-pinch fusion concepts can be explored.

I. LARGE RADIUS IMPLOSIONS:

PLANNING, DIAGNOSING, AND EVALUATING

A. Introduction

There are power-flow advantages in designing pulsed-power generators that implode large radius loads, since increased power flow is needed for scaling to higher x-ray yields, powers, and photon energies. However, if PRS loads are to perform effectively at large radii, then certain minimum requirements on the generator and load designs must be met. Some are known, some are presently being discovered, and some may still need to be discovered. In this section, we will describe some of the load design discoveries that were made this year from titanium and molybdenum wire experiments that were first planned on the basis of our present theoretical understanding and then carried out on Z and Double EAGLE accelerators, respectively. These experiments confirmed the theoretical guidance on which they were based. Further confirmation was obtained from an analysis of aluminum x-ray data that was taken on Saturn several years ago in two series of large wire number experiments.

In part B of this section, a discussion is given of a small number of titanium wire shots that were conducted on the Z accelerator at Sandia National Laboratories. These shots produced more K-shell x rays at 4.7 to 5 keV energies than had previously been obtained on Saturn at 1.6 to 1.8 keV from aluminum arrays. They demonstrated the first successful application of previously derived energy and yield scaling ideas. Moreover, this success was achieved in experiments using arrays of 2 cm radius. No previous, small-wire-number, z-pinch loads had successfully been made to radiate significant amounts of kilovolt x rays while imploding from such a large initial radius. The results from these experiments should help to dispel one of the long-standing myths in this field; namely, that large radius loads are too unstable to implode successfully, where success is defined in terms of kilovolt x-ray output and not in terms of the degree of cylindricalness of the pinch. They suggest that further successes will be achieved in the future as other PRS mythologies are dispelled.

In part C of this section, a brief discussion is given to load design considerations for L-shell radiators, elements that radiate from the neon- and fluorine-like ionization stages rather than the helium- and hydrogen-like stages. This discussion is then carried over into part D of this section, where some molybdenum load designs that were proposed for the Double EAGLE and Saturn generators are discussed. The results of the Double EAGLE experiments demonstrated that we could successfully predict where the kilovolt yields could be optimized as a function of load mass. They also indicated the need for a similar set of experiments on the higher current Saturn machine, where higher velocity implosions could be achieved. These higher η implosions are predicted to significantly improve both load performance and simulation fidelity.

In part E, the results of an analysis of aluminum large-wire-number experiments on the Saturn accelerator are presented in which either the mass of the array was varied for a fixed initial radius or the array radius was varied for a fixed mass. They demonstrate that K-shell yield scaling and radius scaling are significantly dependent on the quality of the experiments that are carried out as much as they are on the quality of the theoretical considerations, i.e., they depend on the symmetry of the implosions that are achieved experimentally. Finally, these load design and analysis issues are summarized in part F.

B. Titanium Load Design for the 20-MA Z Accelerator

Atomic number scaling theory was used to determine the load parameters for a number of (the first ever) titanium shots to be performed on the Z generator. This determination was guided both by theoretical considerations and by past experience with aluminum load designs on the Saturn and Double EAGLE accelerators, and it proved to be accurate. Several factors had to be taken into account in order to successfully scale from aluminum to titanium loads. For one, the minimum kinetic energy requirements are higher for titanium than aluminum, but precisely how much higher was yet to be determined. At a bare minimum, it is known that they must be six times higher per atom, and it is also known that L-shell radiation losses will increase this number. Since good L-shell models do not yet exist, it was not possible to accurately predict the precise L-shell influence to be expected in the experiments. Two, it was also known that a minimum amount of array mass and implosion symmetry would be needed to achieve the densities on axis that are required for rapid kinetic energy thermalization and for efficient x-ray production. And three, recent work has shown that a sufficiently large number of fine wires must be used in order to guarantee that a fairly uniform plasma shell is formed when the wires explode so that a minimum implosion symmetry and stability can be achieved.

The minimum energy requirements for aluminum were determined from past theoretical work and confirmed experimentally. To rapidly ionize into the K-shell, one must promote the rapid conversion of implosion kinetic energy into plasma thermal and ionization energies. For this conversion to terminate in the K-shell, each ion must carry a minimum kinetic energy, E_{min} , which is dependent on the atomic number, Z , of the load. E_{min} has been determined theoretically to scale as $E_{min} = 1.012Z^{3.662} \text{ eV/ion.}^1$ For titanium, $Z = 22$ and $E_{min} \cong 84 \text{ keV/ion}$. If an ion's kinetic energy can be converted rapidly and entirely into stationary plasma energy with negligible energy losses due to x-ray emission, then a minimal implosion velocity, $(v_{imp})_{min}$ can be determined from the equation, $(1/2)m_i(v_{imp})_{min}^2 = E_{min}$ (where m_i is the ion mass). This equation yields the value, $58 \text{ cm}/\mu\text{sec}$. Theory has shown that a plasma radiates efficiently from the K-shell in units of E_{min} . Thus, it is convenient to define the dimensionless energy, $\eta \equiv (1/2)m_i v_{imp}^2 / E_{min}$. The first requirement on titanium load design for the Z accelerator was that η be larger than 1.5 in order to allow for some of the L-shell radiation losses that were expected in these experiments. It was anticipated that η must, in fact, be larger than 2 or 3. The experiments described below support this anticipation.

The mass requirements for the titanium loads were also set by Z scaling arguments and by past experience with aluminum wire loads on Saturn. Early calculations of aluminum implosions with predominantly kinetic energy inputs and a fixed final implosion velocity² had shown a relatively sharply defined transition between two K-shell yield scaling regimes, an m^2 and an m regime, where m is the mass-per-length of the imploding aluminum plasma. The mass at which this transition occurs is termed the mass breakpoint, m_{BP} . It was found to be a function of η and simple arguments suggested that it scaled as $Z^{5.96} \exp(20.6/Z^{0.9})$.² Later calculations,^{1,3} which varied the viscosity and heat conductivity in order to obtain phenomenological agreement with the stagnation state of the plasma in small-wire-number experiments, showed that the mass breakpoint was also a strong function of the quality of the experimental implosion dynamics. The aluminum mass breakpoints calculated in Ref. (2) using classical transport coefficients are a factor of 6 less than those calculated in Ref. (1) using enhanced transport coefficients. The dependence of the mass breakpoint on asymmetry dynamical factors such as arise in the design of gas puff,

small wire number, or large radius/small mass experiments makes it a theoretical concept that can only be approximated experimentally. However, good experiments yield good approximations. The significance of the $m = m_{BP}(\eta)$ curve for aluminum experiments on Saturn⁴ and in the calculations of Ref. [2] was that it defined the upper boundary of a region in (m, v_{imp}) space in which the efficient emission of K-shell x-rays could be expected. The mass of the titanium loads was chosen by requiring that these loads fall in or close to this region.

The pure titanium shots that were planned are displayed in Figure 1 relative to two mass breakpoint curves and to an $\eta = 2$ and $\eta = 4$ curve for titanium. The mass breakpoint curve labeled soft in Figure 1 is scaled from the mass breakpoint curves of Refs. [1] and [3], which are shifted by a factor of six from the mass breakpoint curve labeled hard. This latter curve was determined in Ref. [2] from 1-D implosion calculations that employed classical transport coefficients. These calculations produced tight pinches with x-ray power pulses slightly less than 1 nanosecond in duration. Since pulse duration is a function of wire number, experimentally determined breakpoint curves for titanium are expected to lie between the two breakpoint curves shown for $\eta \geq 4$ depending on the wire number of the experiments. For the low- η regime ($\eta < 4$), Ref. [5] makes the point that it is of limited utility to quantify the breakpoint boundary because it depends too much on the type of experiment that is modeled, e.g., on whether one is modeling a wire array as opposed to a uniform density gas puff experiment. This reference does show that, in general, the breakpoint occurs at much higher masses than are given by the soft implosion curve that is extrapolated below the $\eta = 4$ line in Figure 1. Moreover, the unknown experimental role of L-shell radiation losses on efficient conversion of implosion kinetic energy into K-shell x rays, makes the minimum η value for achieving efficient conversion additionally uncertain.

Three considerations were made in selecting the shots in Figure 1: (1) the influence of plasma asymmetries and instabilities was minimized by fixing the initial array diameter at 40 mm, (2) the placement of the mass breakpoint curve was tested by carrying out a mass scan using 20.3 μm diameter wires, and (3) the effects of pinch quality were investigated by carrying out a wire number scan from 80 to 160 wires and by making a comparison of similar arrays with and without nickel cladding. Since reductions in the array mass lead to higher implosion velocities, they also move the implosions closer to the mass breakpoint curve as shown in Figure 1.

The yields that were observed in each shot are listed in Figure 1 next to the shots. The wire numbers are in parentheses next to the yields. It was expected that the smallest mass shot would produce the largest K-shell yield because it had the closest proximity to the mass breakpoint curve. This expectation is borne out by the yield data. The dip in yield from 92 to 75 kJ in going from 140 wires to 80 wires is a wire-number effect since the smaller massed, higher velocity implosion using 80 wires should otherwise have produced more x rays than the 140 wire shot.

As Figure 2 shows, the large K-shell yields in these experiments came mainly from the helium-like ionization stage even though one might have expected more hydrogen-like emission if the L-shell losses had not been so large in these low- η experiments. The two inverted triangles that are located on the $\eta = 4$ curve show the array masses that are needed to achieve this higher η value on the Z accelerator. A low mass of 0.55 mg/cm is required for implosions from an initial radius of 20 mm, while a higher mass of 0.75 mg/cm can be imploded from a 25 mm radius. To maintain implosion quality from such large radii, small mass loads, however, requires a large number of smaller diameter titanium wires than were available for these initial experiments. This experimental impediment will hopefully be eliminated in the near future leading perhaps to a doubling or more

of yield in the 4.7 to 6.0 keV energy interval.

C. Basic Tradeoffs of K- vs. L-shell Radiators

At present, the most efficient method known for generating large yields of x-rays in the 1-10 keV photon energy range is by the implosion of a carefully selected load to form a dense Z-pinch plasma on a high-current generator. By "large yields" we mean hundreds of joules to hundreds of kilojoules. To date, the best results have been obtained by selecting a load so that the K-shell ions (He- and H-like stages) of the load element are produced in abundance and radiate copiously. The principal resonance lines of these stages as well as the associated radiative recombination continua generate the bulk of the desired radiation. The most frequently employed elements producing the most satisfactory results have been neon,⁶⁻⁸ aluminum,⁹⁻¹³ argon,¹⁴⁻¹⁶ and titanium.¹⁷

Of these four elements, two are noble gases whose incorporation into a load is accomplished by the use of gas puffs produced by fast valves coupled to specially designed supersonic nozzles. Al and Ti, on the other hand, are drawn into arrays of fine wires to form the initial load configuration, whose mass and position is thereby known exactly and subject to accurate control and modification. Although the initial mass distribution of a gas puff load can be measured interferometrically, controlling that distribution is problematic. Such effects as zippering¹⁴ and gas fill-in away from the nozzle hamper efforts to both set the desired initial mass distribution and correlate the experimental x-ray data to any systematic modification of the initial load conditions or to any single, clearcut implosion dynamics.

The use of wire loads rather than gas puffs has become even more desirable in light of recent results,¹⁰⁻¹³ which demonstrate that the use of more and finer wires, more closely spaced, can produce enhancements in both x-ray power and yield when compared with pinches produced from loads at the same initial radius, with the same mass, but using fewer and coarser wires. It is now firmly believed that the superior results with large numbers of wires in large diameter array loads (ranging up to almost 200) derive from the creation of an initially axisymmetric, relatively uniform plasma shell rather than individual wire plasmas. The better implosion and pinch quality results in some cases in better on-axis mass participation¹³ in the K-shell radiation, leading to higher yield as well as higher power.

Currently, K-shell Ne is a major source of 1 keV x-rays as is Ar for those of 3 keV energy. Obviously, the benefits of wire array loads cannot be realized for x-ray production in those specific energy ranges if the K-shell stages are to be used as the radiators. If we wish to use wire arrays rather than gas puffs to provide more control and knowledge of the initial mass distribution, better implosion quality, and yield reproducibility, other ionic stages of other elements must be considered. For any K-shell radiating element, one can produce L-shell photons of the same energy by employing another element of much higher atomic number. The purpose of this subsection is to explore the basic energetics of such a choice, which provides initial scoping considerations but cannot replace the diagnostic necessity for developing detailed L-shell models.

For present purposes we concentrate on the Ne- and F-like ionization stages of the L-shell. These are the easiest to reach experimentally. Also, much theoretical and experimental atomic data exists for these stages due to x-ray laser research. In the data that is presented below, for ionization potentials we have relied mostly on Ref. (18), for Ne-like energy levels, on Ref. (19), for F-like data, Refs. (20) and (21). When specific energy levels were not available, we assume that they bear the same relationship to the ionization potentials of the Ne- and F-like stages as do the known

levels of Fe, Se, and Ag. Very high accuracy is not required to make a basic comparison of the K and L shells.

To provide a framework and guidance for designing and interpreting Z-pinch experiments aimed at efficient production of K-shell x-rays, the η parameter was defined and developed.² This basic dimensionless quantity springs from the fact that, for each element, an irreducible minimum of energy is needed to strip one atom to the K-shell and heat the liberated electrons to a temperature conducive to efficient radiation of K-shell photons. η is defined as the implosion kinetic energy per atom divided by this minimum energy. Obviously, an η can also be defined and developed for the L shell, and this is accomplished by using the atomic data sources cited above, Refs. (18)-(21). Stripping to the L shell is herein defined as achieving an ionization balance of half Ne-like and half F-like.

The basic data appears in Table I. Each K-shell radiating element of atomic number Z_K has an L-shell radiating counterpart (atomic number Z_L) whose L-shell lines are at the same energy $h\nu$, in keV. The stripping/heating energy, also in keV, E_{minK} , is given for the K-shell element as well as the energy needed to strip its L-shell counterpart (E_{minL}) to the L-shell stages which radiate photons at the same energy.

TABLE 1

Z_K	Z_L	$h\nu$	E_{minK}	E_{minL}
10	28	1.0	4.9	12
13	36	1.7	12.8	35
16	42	2.7	26	68
18	47	3.3	42	111
22	54	4.8	89	215
30	74	7.9	286	709

To simplify these results without serious error, one may keep in mind the *approximate* number 2.6. Given a K-shell element of atomic number Z , to find the atomic number of the element which radiates the same energy photons in its L shell, take $2.6Z$. Example, silver ($Z=47$) radiates L-shell photons of the same energy as the K shell of Ar ($Z=18$). Also, unfortunately, the stripping/heating energy E_{minL} of the L-shell element is about 2.6 times that of its K-shell counterpart. Of course, the corresponding L-shell ion is 2.6 times as heavy as the K-shell one, so that if the same mass load is used, 2.6 times fewer L-shell ions will be present in the load. Note, this counterbalances the factor of 2.6 more energy needed to strip/heat the L-shell element. Therefore, if the same mass load is used, the effective η for the L shell will be the same as for the K shell of the lower atomic number element which radiates photons of the same energy. In other words, to get the same η for the L shell, one should use the same mass load. This means 2.6 times fewer ions, which embodies the possibility of mass starvation. This possibility might be compensated by the superior achievable implosion quality obtainable by replacing K-shell gas puffs with L-shell wires and also by the greater emissivity of the L-shell radiators.

Of course, the L shell has a more complex pattern of spectral lines with different opacities than those of the K shell. Thus, upon burning through the Ne- and F-like stages, the pinch will radiate harder photons from the succeeding O- and N-like stages, leading to greater simulation fidelity as well as higher photon energies. In this sense, the L shell is advantageous relative to the K shell, where burnthrough results in concentrations of the non-radiating bare nucleus. Also, there are different individual ionization thresholds and corresponding ionization cross sections. Radiative cooling will be different, probably greater than prevails in K-shell experiments, and will affect the pinch dynamics and increase compressibility. The initial experiments conducted on Double EAGLE and Saturn will therefore begin to answer the basic question: *can the advantages of wires over gas puffs, the more complex atomic structure and the greater number of ionization stages of the L shell be realized on existing machines to overcome the energetic disadvantage of having to use about 2.6 times fewer radiators to obtain the η needed to reach the Ne- and F-like stages?* For machines like DECADE and Z, the answer has a good chance of being yes. As the next subsection shows, for machines like Double EAGLE, the answer is no. If these experiments on the different machines are to be usefully evaluated, detailed atomic modeling of the L shells of the target elements will be essential. The development of reliable L-shell models is also needed to improve the chances of success in scaling to higher fidelity x-ray simulation through higher current machines and higher atomic number, L-shell loads.

D. Molybdenum Load Design for the Double EAGLE Accelerator

A series of five molybdenum wire shots were proposed this year for Double EAGLE. There were two main motivations for these experiments. Firstly, a one-to-one correspondence exists between L-shell radiators, which radiate from the neon-like and fluorine-like ionization stages, and K-shell radiators, which radiate from the helium-like and hydrogen-like ionization stages. The correspondence is between elements that radiate into roughly the same spectral energy bin. For example, krypton radiates the same color neon- and fluorine-like photons as aluminum radiates helium- and hydrogen-like photons. Silver is similarly in correspondence with argon. Thus, for every gas puff radiator, there is a wire array option. Secondly, when an element ionizes through the hydrogen-like ionization stage, there are no more bound electrons and x-ray emission decreases abruptly. On ionizing through the fluorine-like stage, however, emission rates continue to go up and higher energy photons are emitted. Thus, there is increased potential for improving simulation fidelity when this burn-through occurs.

To effectively replace a K-shell radiator with an L-shell radiator, however, one difficulty must be overcome. It is illustrated by two sets of calculations whose results are displayed in Figures 3 and 4. When the kinetic energy generated by an implosion is too low, resulting in small η values, the K-shell radiator will generally outperform the corresponding L-shell radiator. This behavior is illustrated in Figure 3 for two low- η , aluminum and krypton, implosions. As the mass of the imploded load is increased, the yield from both elements increases; however, the K-shell yield for aluminum always remains greater than that of krypton. This behavior is related to krypton's higher atomic number, since in equal mass aluminum and krypton plasmas, there would be more aluminum ions that can radiate than krypton ions. When η is increased (Figure 4), this behavior changes, and is indicative of the intrinsically greater emissivity of krypton ions compared to aluminum ions. The message in Figures 3 and 4 is that one must give L-shell plasmas a greater kick than is needed for K-shell plasmas in order to tap into an L-shell ion's greater emissivity. As Figure 4 illustrates, the

payoff should be well worth the effort.

Theory suggests that the design of L-shell loads can be patterned off the design of their corresponding K-shell loads. To test this theory, a set of five molybdenum wire shots were planned for Double EAGLE using the eta values and mass breakpoint curve of sulfur, which is the K-shell counterpart for molybdenum. The soft breakpoint and the $\eta = 2$ curves of the sulfur K-shell are drawn in Figure 5. Two sets of solid circles (large and small) for a given load mass represent the molybdenum shots in Figure 5. The two sets arise from an uncertainty in the Double EAGLE circuit model. The molybdenum η values are taken to be the same as the corresponding sulfur η values and carry the implicit design requirement that Double EAGLE's energy coupling to each molybdenum load be the same as Double EAGLE's coupling to the same massed sulfur load.

The masses chosen for the molybdenum loads were expected to span an interval in which the highest L-shell yield would occur. The Double EAGLE experiments confirmed this expectation. As in Figure 1, the numbers adjacent to the circles are the experimentally observed yields; the numbers in parentheses are the wire numbers in each shot. Peak yield occurred inside the region for efficient sulfur K-shell emission and for the mass whose implosion velocity brought it closest to the mass breakpoint curve, as expected. Double EAGLE did not have sufficient current drive to operate in a high- η sulfur regime and yields were low. The Saturn generator would not have this limitation. The solid circles in the upper right of Figure 1 represent a series of proposed molybdenum shots for Saturn for arrays of 24 mm diameter. The number in parentheses next to each circle is the wire number of the shot. All arrays consist of 0.35 mil wires. Based on the aluminum/krypton calculations (Figures 3 and 4), dramatic yield increases should be expected for these shots as compared to the Double EAGLE shots both because of the higher η values and because of the greater wire numbers and load masses.

E. An Analysis of Variable Mass and Variable Radius Experiments on the Saturn Accelerator

Several years ago, a series of variable-wire-number aluminum experiments that had been carried out on the Saturn generator were followed up by two further series of shots. In one, the radius of the aluminum arrays was held at 12 mm and the mass of the arrays was varied by changing the wire number for a few shots and the wire size in the other shots. In the other series of shots, the array mass and wire-number were held essentially fixed and the array radius was varied. In both series, wire number was high (≥ 93) and wire size was small (≤ 0.8 mil). These load parameters are in contrast to the earlier 24, 30, and 42 wire number aluminum shots on Saturn that utilized wire sizes up to 2.5 mil.¹³ The increased wire number had a significant impact on the quality of the implosions, and, together with the titanium experiments described above, they support the conclusion that there is a need to reorient the PRS program away from short to longer risetime machines and towards larger radius implosions.

The variable-mass experiments that are analyzed consist of eight shots, which are listed in the following table:

The goal of the experiments was to maintain a high and constant wire number for all shots, but, because the smallest aluminum wire size available commercially is 0.4 mil, the arrays with masses of 204 and 298 $\mu\text{g}/\text{cm}$ could only be constructed with fewer than 192 wires. The other mass variations were made by varying the wire size from 0.4 to 0.8 mil. Because all arrays in this series had the same initial array diameter (24 mm), the mass increases produced corresponding

Table 1: Saturn Variable Mass Al-wire Experiments ($r_i=12$ mm)

Shot	Array Mass ($\mu\text{g/cm}$)	# Wires	Yield (kJ)	η	Pulsewidth (ns)	Pinch-size (mm)
2241	204	93	62.9	13.8	4.4	0.5
2231	298	136	62.1	10.4	4.8	0.5
2232	416	190	48.8	7.7	7.6	0.6
2238	420	192	36.0	7.7	6.0	0.6
2235	656	192	54.2	5.0	5.2	0.5
2233	945	192	29.8	3.3	13.6	0.5
2234	1286	192	18.6	2.3	12.4	0.5
2237	1680	192	18.0	1.4	11.0	0.5

reductions in the implosion velocities, or in the η values that could be reached. These values were estimated by calculating the early run-in of a plasma shell using a 0-D model of the Saturn circuit. The calculations were stopped once the radius of the shell reached one-tenth (1.2 mm) of its initial value. The etas calculated by this method are listed in Table 1.

In the planning and evaluation of the 24, 30, and 42 wire shots of the previous Saturn experiments,^{4,13} it proved instructive to locate the shots in (m, v_{imp}) space relative to the mass breakpoint curve that had been calculated in Ref. [1], which we denote as the soft breakpoint curve. Here m is the mass per length of a wire array and v_{imp} is the estimated maximum velocity reached by the array in an implosion. The mass breakpoints represent the load masses where the K-shell yields were calculated to make a sharp transition from an m^2 scaling into an m scaling regime for different, given implosion velocities. The soft breakpoint curve had been calculated by increasing the heat conductivity and artificial viscosity coefficients so as to soften the calculated implosions in order to obtain a closer match to ion densities that were being inferred from analyses of low-wire-number (≤ 42) and gas-puff z-pinch experiments. This curve approximately defines an upper boundary for the region in (m, v_{imp}) space in which the efficient conversion of kinetic energy into K-shell x rays is predicted, and has been observed, to occur. It represents the locus of implosion velocities where the maximum K-shell yields are calculated to occur for low-wire-number, given mass, arrays. For the low-wire-number, aluminum, Z-pinch shots conducted on the Saturn accelerator,⁴ the largest yielding shots were found in the near proximity of this curve.

The softening of the implosions in Ref. [1] was found to shift the mass breakpoint by approximately a factor of six from the curve that was originally calculated,² which we denote as the hard breakpoint curve. In the original calculations, Braginskii transport coefficients were used along with the un-enhanced artificial viscosity of Schulz.²² The pinches that were calculated using these classical values for closure of the plasma fluid equations reached much higher densities on axis and produced much higher powers than the low-wire-number experimental pinches. However, with the advent of large-wire-number loads, dramatic increases in peak K-shell powers from aluminum pinches¹⁰ as well as dramatic narrowing of the x-ray pulsewidths have been observed as the number of wires was increased. In these experiments, both the array mass and the array diameter were held

fixed. Both of these trends indicate that the pinches were approaching plasma compressions on axis that much more closely approximated those originally modelled in the 1-D calculations of Ref. [2]. The high-wire-number, variable-mass, experiments of Table 1 provide further confirmation of this behavior.

As with the 24, 30, and 42 wire experiments, the yield behavior of the shots in Table 1 can be instructively evaluated when plotted in (m, v_{imp}) space (see Figure 6), in this case relative to both the hard and soft mass breakpoint curves. The shots in Table 1, represented as solid circles in Figure 6, were located using the relation, $v_{imp} = 29.4\sqrt{\eta}$, valid for aluminum. The shot yields are listed next to each circle and the wire number of each shot is enclosed in parentheses next to each yield. The $\eta = 2$ curve, which is drawn in Figure 6, provides a reference velocity near and below which K-shell yields are expected to be low [see Ref. (5)]. This expectation is borne out by the data. Most importantly, in these experiments, the yields are found to peak near the hard breakpoint curve rather than near the soft boundary curve as in the 24 wire experiments [see Ref. (4)].

The slow falloff of the yields as the array mass is increased and as the shots move away from the hard breakpoint curve is another feature of these experiments that approximates the yield behavior calculated in Ref. (2) for $\eta \geq 4$. This yield falloff was more severe in the low-wire-number Saturn experiments. These experiments fall in or near what has been termed the wire-plasma regime, where the individual wires explode but too slowly to merge early in time to form an approximate plasma shell that approximates the initial condition used in all calculations. The lack of merger is both a wire number and a wire size effect. In the low-wire-number Saturn experiments, a correlation was noted between the yield behavior that was observed and the relative amount of overlap between the wire explosion and the array implosion dynamics.²³ When the wires are too thick, they are incompletely evaporated as the run-in begins. This behavior may be a contributing factor to the yield and conversion efficiency falloff at large mass in Figure 6.

In all but two of the shots in Table 1, sufficient data was taken to allow spatially and temporally averaged temperatures and densities to be inferred as a function of the variations in the array mass. From these densities and from the time-averaged pinch sizes listed in Table 1, the average array mass fraction participating in the K-shell emission can also be inferred. When the yields, pulsewidths, peak powers together with these inferred quantities are plotted as a function of array mass, they tell a consistent story about the dynamics of producing K-shell x rays (see Figures 7-12) that is in accord with the calculational results presented in Refs. (2) and (5).

Three z-pinch behaviors are evident from Figures 7-12. High yields, short pulsewidths, high densities, relatively constant K-shell temperatures, and high peak powers are generated in the high- η regime (theoretically from Ref. (2), $\eta \geq 4$). Low yields, long pulsewidths, low densities, relatively constant K-shell temperatures, and low peak powers are generated in the low- η , larger wire size, regime (theoretically from Ref. (5), $\eta \sim 2 - 3$). A third behavior, characteristic of the unpredictability of z-pinch is also seen in these figures; namely, that the two shots at $\sim 420\mu\text{g}/\text{cm}$ fall mysteriously off of the trend line defined by shots 2241, 2231, and 2235, which surround shots 2232 and 2238. For the $420\mu\text{g}/\text{cm}$ shots, the yields, densities, and peak powers all fall below the corresponding high- η quantities, while the pulsewidths are longer than the high- η pulsewidths.

The sharp transition between high- and low- η regimes seen in the yield, pulsewidth, power, and density data is missing from the mass fraction data of Figure 12. Thus, Figure 12 illustrates another important feature of the high- η implosions. While increasingly larger amounts of the array mass can be induced to radiate in the K-shell as the kinetic energy being thermalized on axis goes

up, the rate at which the thermalized energy is emitted depends on the degree of compression achieved. The 420 $\mu\text{g}/\text{cm}$ shots, for some unknown reason, did not compress as well as the other high- η shots, and, hence, they did not radiate as much as these other shots even though the less dense pinch subsequently had more inertial confinement and radiated for a slightly longer period of time. The very small values of K-shell mass participation in the low- η regimes also shows the important role that gradients play in these emissions. The general feature that has been diagnosed in the high-wire-number Saturn shots is that they produce a pinch on axis with a hot core and a progressively cooler, surrounding plasma.^{12,24-26} Without the hot core, the low- η shots would not radiate as effectively since the implosion energy would be otherwise spread out in the plasma and dissipated as L-shell and axial kinetic energy losses. The low mass fractions in these experiments show the important role that gradients play, even at high η values.

In the second series of large-wire-number shots, the array mass was held constant and the array radius was varied. These shots are listed in Table 2. With the exception of a few wire breakages, the wire number was kept fixed at 136 and the array mass at 298 $\mu\text{g}/\text{cm}$. Note that shot 2231 is common to the both the variable-mass and variable-radius experiments. By fixing the mass at 298 $\mu\text{g}/\text{cm}$ while increasing the radius from 0.875 to 2.0 cm, the implosions are made to span a range of high η values from 8.1 to 14.6, all of which lie below the hard breakpoint curve of Figure 6. In each of these shots, the same sized, 10 μm , wires were used. Thus, the wire number could not be increased with radius, causing the interwire gap spacing to increase as the radius was increased.

Saturn Variable Radius Al-wire Experiments ($m_{arr} \cong 295 \mu\text{g}/\text{cm}$)

Shot	Array Radius (cm)	Gap (mm)	Yield (kJ)	η	Pulsewidth (ns)	Pinch-size (mm)
2239	0.875	0.4	55.1	8.1	4.4	0.4
2243	0.875	0.41	55.8	8.1	4.4	0.4
2231	1.2	0.55	62.1	10.5	4.8	0.5
2228	1.6	0.74	60.3	13.2	5.2	0.5
2240	1.6	0.77	55.2	13.2	6.0	0.5
2230	2.0	0.95	83.7	14.6	6.2	0.5-

In the variable-wire-number experiments, in which both the mass and radius were held fixed, it was noted that peak power decreases as gap spacing increases. Thus, the shots in Table 2 do not purely indicate the effects on K-shell yields that increases in η have at fixed mass. Interwire gap effects are also included in the yield, pulsewidth, temperature, density, peak power, and mass fraction data that were obtained for these shots and that are displayed in Figures 13-18. Since the η increase occurs within the predicted region for efficient conversion of kinetic energy to kilovolt x rays, the yields should continue to increase, as they do (Figure 13), until the mass breakpoint curve is reached. As in the variable-mass shots, two of the variable-radius shots (2228 and 2240) lie anomalously below the upward trend line that connects the other surrounding shots. Because of the one-to-one correspondence between radius and gap spacing in these experiments, one can

plot the measured and inferred quantities as functions of either the array radius or the gap spacing, although they essentially depend on both. Only the yields are presented as a function of radius. The other quantities are plotted as a function of gap so that comparisons can be made to similar figures that were drawn in the variable-wire-number experiments (see Ref. (25)).

As Figures 13, 14, and 17 show, the increase in yields appears to correlate more with increases in pulsewidth than to peak power increases. The increases in pulsewidth, in turn, correlate with increases in gap spacing as they did in the variable-wire-number experiments. On the other hand, the relative flatness in the power data is indicative of the competing effects that the larger η values would have in increasing the power output as opposed to the gap increases that would decrease power. The flatness of the inferred densities as a function of gap spacing is another manifestation of these competing effects. As seen in Figures 7 and 9, higher yields are correlated with higher densities; whereas, as an analysis of the variable-wire-number data showed, densities go down as gap spacing goes up.

A third consideration for interpreting these experiments involves the decreased symmetry and stability that occurs in addition to the increased η values and interwire gap spacings as the arrays get larger. Again, the limited data from these experiments is suggestive, but not definitive, of both plus and minus effects. On the plus side, Figures 14, 16, and 18 together suggest that the pinches from large radii have gentler temperature gradients, longer inertial confinement, and therefore, more K-shell mass participation. The softening of temperature gradients and increased mass participation both contribute to increased yields [see, in particular, Ref. (13)]. If the softening of the pinch occurs as a result of increased instability growth, then, in this case, the effect on yields is a positive even though the effect on peak power is a negative.

F. Summary

The Saturn variable-mass and variable-radius, high-wire-number, series of experiments showed the necessity, by way of the yield behavior of these shots in addition to power and pulsewidth behavior, of keeping the wire number high in order to achieve as high a symmetry during the implosion as possible. These implosions lead to higher compressibility and higher densities on axis than are achievable in low-wire-number implosions. Higher densities are a prerequisite for achieving the rapid rates of excitation and ionization that are needed for high yield, high photon energy production.

The variable-radius experiments, in particular, demonstrated that one could go out in radius successfully even on a short risetime machine such as Saturn if the wire number was kept high enough. To go out in radius while maintaining a high wire number and small interwire gap spacings, however, requires either very fine (and therefore very breakable) wires or an increase in load mass. Increases in load mass, in turn, require increases in the current drive. However, by going to longer current risetimes, which is possible by going out in radius, one can take some of the stress out of the pulse-power generator design and deliver more energy to the load. All of these factors work together since one also gets larger numbers of radiating ions and higher yields by going to higher mass loads.

Finally, we note that the titanium experiments on Z confirm the above ideas. They produced the highest yields ever at 4.8 to 6.0 keV, by imploding from a large (by past standards) radius (2 cm) with a high current machine. These yields should go up further when finer titanium wires

are available for load design. Such wires will permit more wires to be used, which will enable the implosions to start from a larger than 2 cm radius. Since fine molybdenum wires are already available, experiments on Saturn and Z with this element are also projected to be big winners.

REFERENCES

1. J. W. Thornhill, K. G. Whitney, C. Deeney, and P. D. LePell, "Phenomenological Modeling of Turbulence in Z-pinch Implosions", *Phys. Plasmas* **1**, 321 (1994).
2. K. G. Whitney, J. W. Thornhill, J. P. Apruzese, and J. Davis, "Basic considerations for scaling Z-pinch x-ray emission with atomic number", *J. Appl. Phys.* **67**, 1725 (1990).
3. K. G. Whitney, J. W. Thornhill, J. P. Apruzese, J. Davis, C. Deeney, P. D. LePell, and B. H. Failor, "Optimization of x-ray emission in Z-pinch implosions: Theory versus Experiment", *Phys. Plasmas* **2**, 2590 (1995).
4. K. G. Whitney, J. W. Thornhill, J. L. Giuliani, Jr., J. Davis, L. A. Miles, E. E. Nolting, V. L. Kenyon, W. A. Speicer, J. A. Draper, C. R. Parsons, P. Dang, R. B. Spielman, T. J. Nash, J. S. McGurn, L. E. Ruggles, C. Deeney, R. R. Prasad, and L. Warren, "Optimization of K-shell emission in aluminum z-pinch implosions: Theory versus experiment", *Phys. Rev. E* **50**, 2166 (1994).
5. J. W. Thornhill, K. G. Whitney, J. Davis, and J. P. Apruzese, "Investigation of K-shell emission from moderate-Z, low- η (-velocity), Z-pinch implosions", *J. Appl. Phys.* **80**, 710 (1996).
6. C. Deeney, T. J. Nash, R. B. Spielman, J. F. Seaman, J. S. McGurn, D. O. Jobe, M. F. Vargas, T. L. Gilliland, R. C. Mock, K. W. Struve, K. G. Whitney, P. E. Pulsifer, J. P. Apruzese, J. W. Thornhill, and J. Davis, "Improved large diameter wire array implosions from increased wire array symmetry and on-axis mass participation", *Phys. of Plasmas* **5**, 2431 (1998).
7. W. D. Schulz, *J. Mathe. Phys.* **5**, 133 (1964).
8. T. W. L. Sanford, G. O. Allshouse, B. M. Marder, T. J. Nash, R. C. Mock, R. B. Spielman, J. F. Seamen, J. S. McGurn, D. Jobe, T. L. Gilliland, M. Vargas, K. W. Struve, W. A. Stygar, M. R. Douglas, M. K. Matzen, J. H. Hammer, J. S. De Groot, J. L. Eddleman, D. L. Peterson, D. Mosher, K. G. Whitney, J. W. Thornhill, P. E. Pulsifer, and J. P. Apruzese, "Improved Azimuthal Symmetry Greatly Increases X-ray Power from Wire-array Z-pinchs", *Phys. Rev. Lett.* **77**, 5063 (1996).
9. K. G. Whitney, J. W. Thornhill, R. B. Spielman, T. J. Nash, J. S. McGurn, L. E. Ruggles, and M. C. Coulter, in "Proceedings of the Third International Conference on Dense Z-pinchs, London, 1993", edited by M. Haines and A. Knight, *AIP Conference Proceedings* **299**, p. 429.
10. T. W. L. Sanford, T. J. Nash, R. C. Mock, R. B. Spielman, J. F. Seamen, J. S. McGurn, T. L. Gilliland, M. Vargas, K. G. Whitney, J. W. Thornhill, P. E. Pulsifer, and J. P. Apruzese, "Time-dependent Electron Temperature Diagnostics for High-power, Aluminum Z-pinch Plasmas", *Rev. Sci. Instrum.*, **68**, 852 (1997).
11. T. W. L. Sanford, R. C. Mock, T. J. Nash, K. G. Whitney, P. E. Pulsifer, J. P. Apruzese, D. Mosher, D. L. Peterson, and M. G. Haines, "Systematic trends in x-ray emission characteristics of variable-wire-number, fixed-mass, aluminum-array, Z-pinch implosions", *Phys. of Plasmas*, to be published, (1999).
12. K. G. Whitney, J. W. Thornhill, P. E. Pulsifer, J. P. Apruzese, T. W. L. Sanford, T. J. Nash, R. C. Mock, and R. B. Spielman, "Analyzing Time-resolved Spectroscopic Data from an Azimuthally Symmetric, Aluminum-wire Array, Z-pinch Implosion", *Phys. Rev. E* **56**, 3540 (1997).

13. J. P. Apruzese, P. E. Pulsifer, J. Davis, R. W. Clark, K. G. Whitney, J. W. Thornhill, T. W. L. Sanford, G. A. Chandler, C. Deeney, D. L. Fehl, T. J. Nash, R. B. Spielman, W. A. Stygar, K. W. Struve, R. C. Mock, T. L. Gilliland, D. O. Jobe, J. S. McGurn, J. F. Seamen, J. A. Torres, and M. Vargas, "K-shell radiation physics in the ultrahigh optical depth pinches of the Z generator", *Phys. of Plasmas* **5**, 4476 (1998).

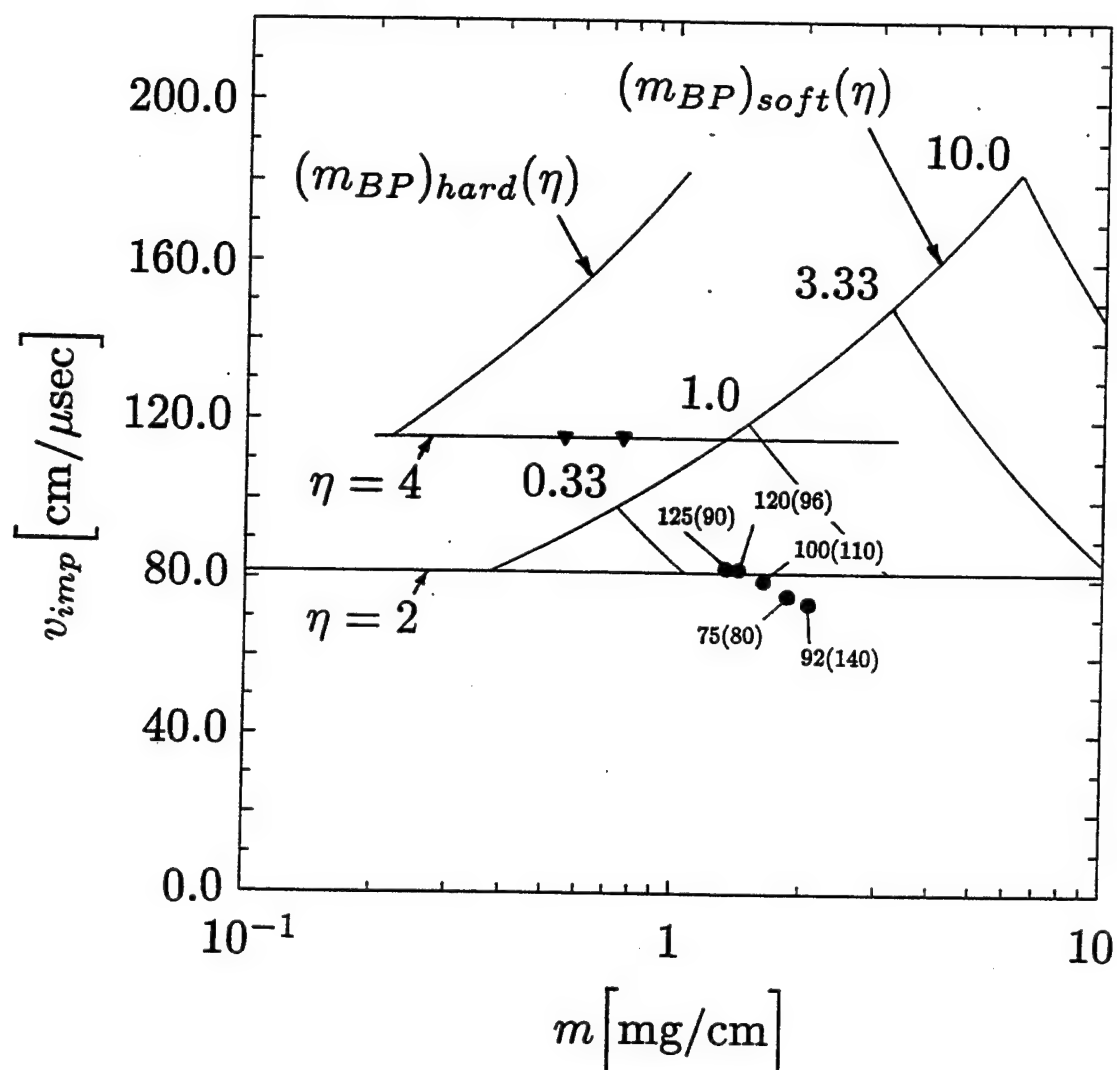


Figure 1

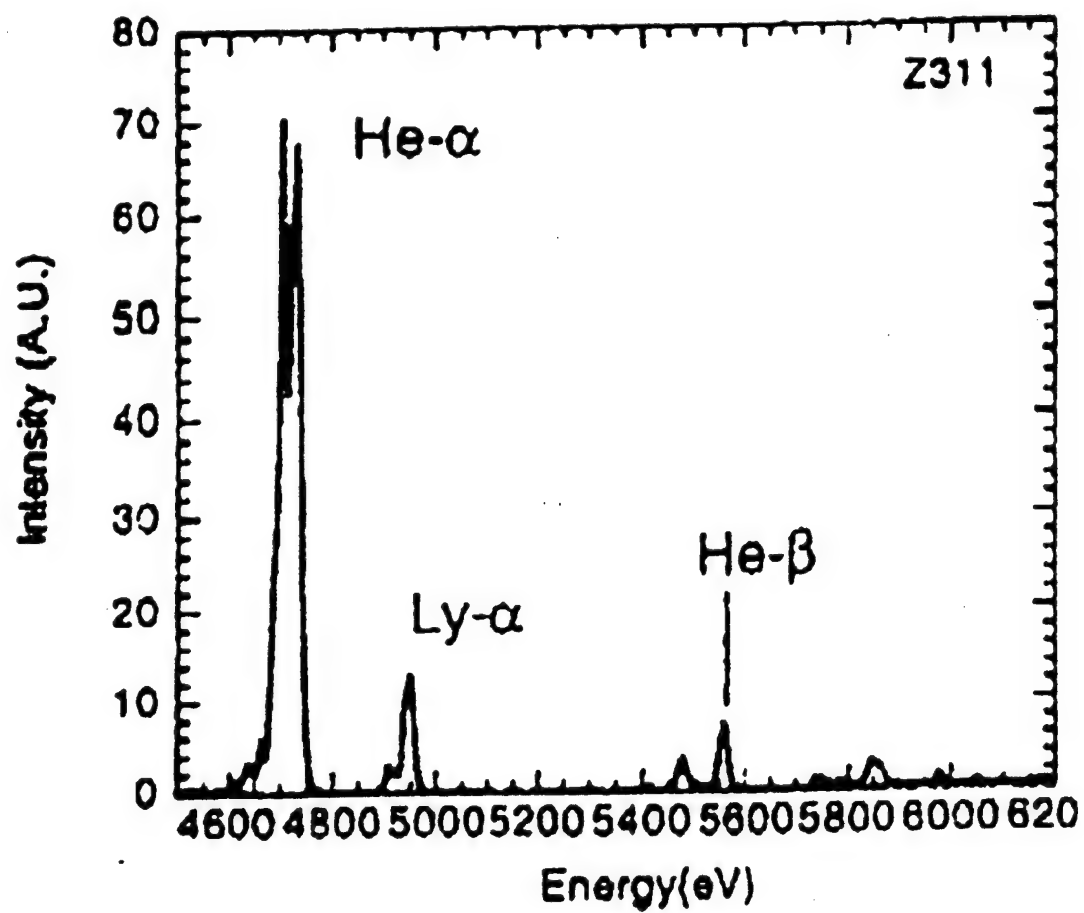


Figure 2

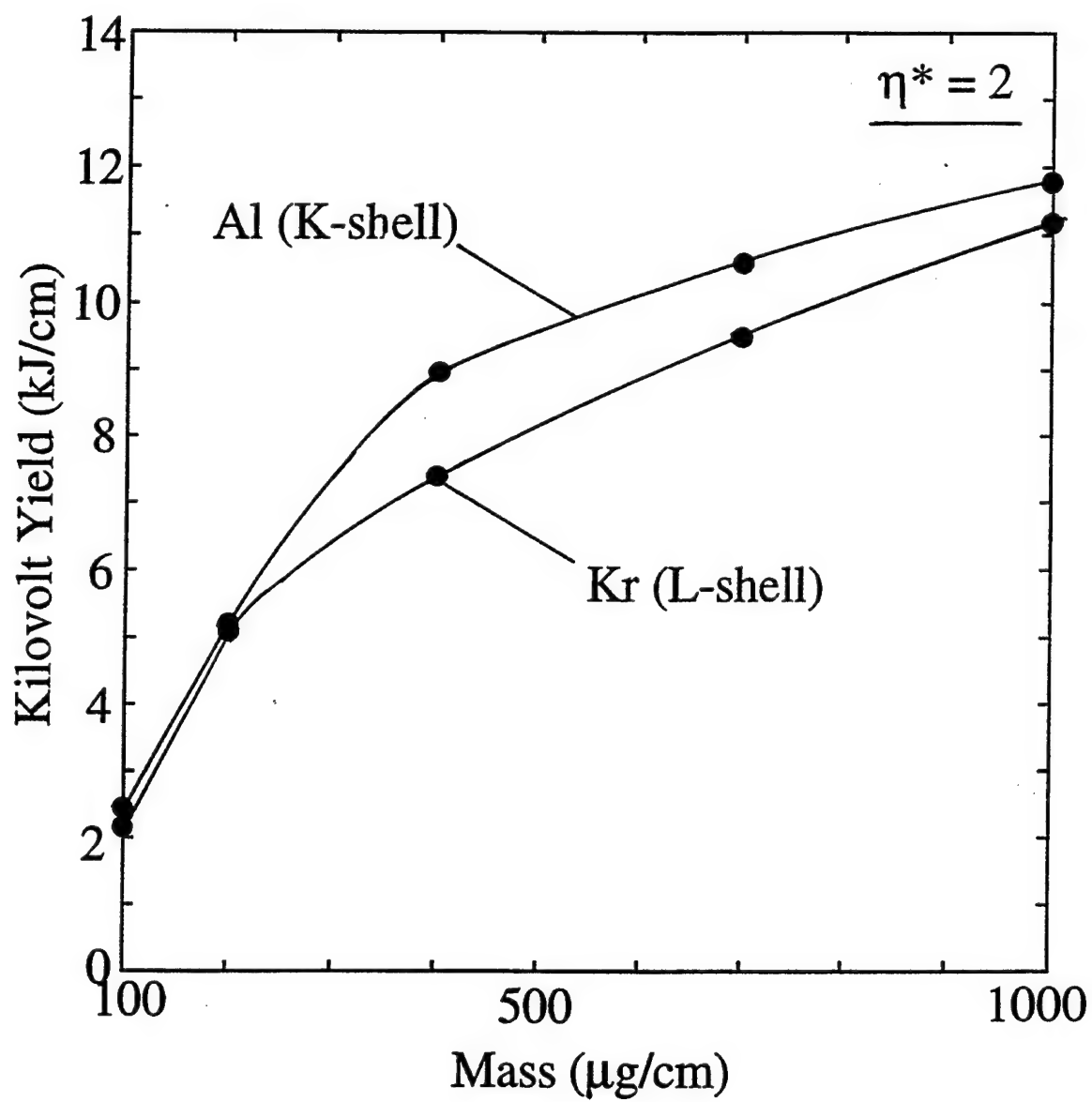


Figure 3

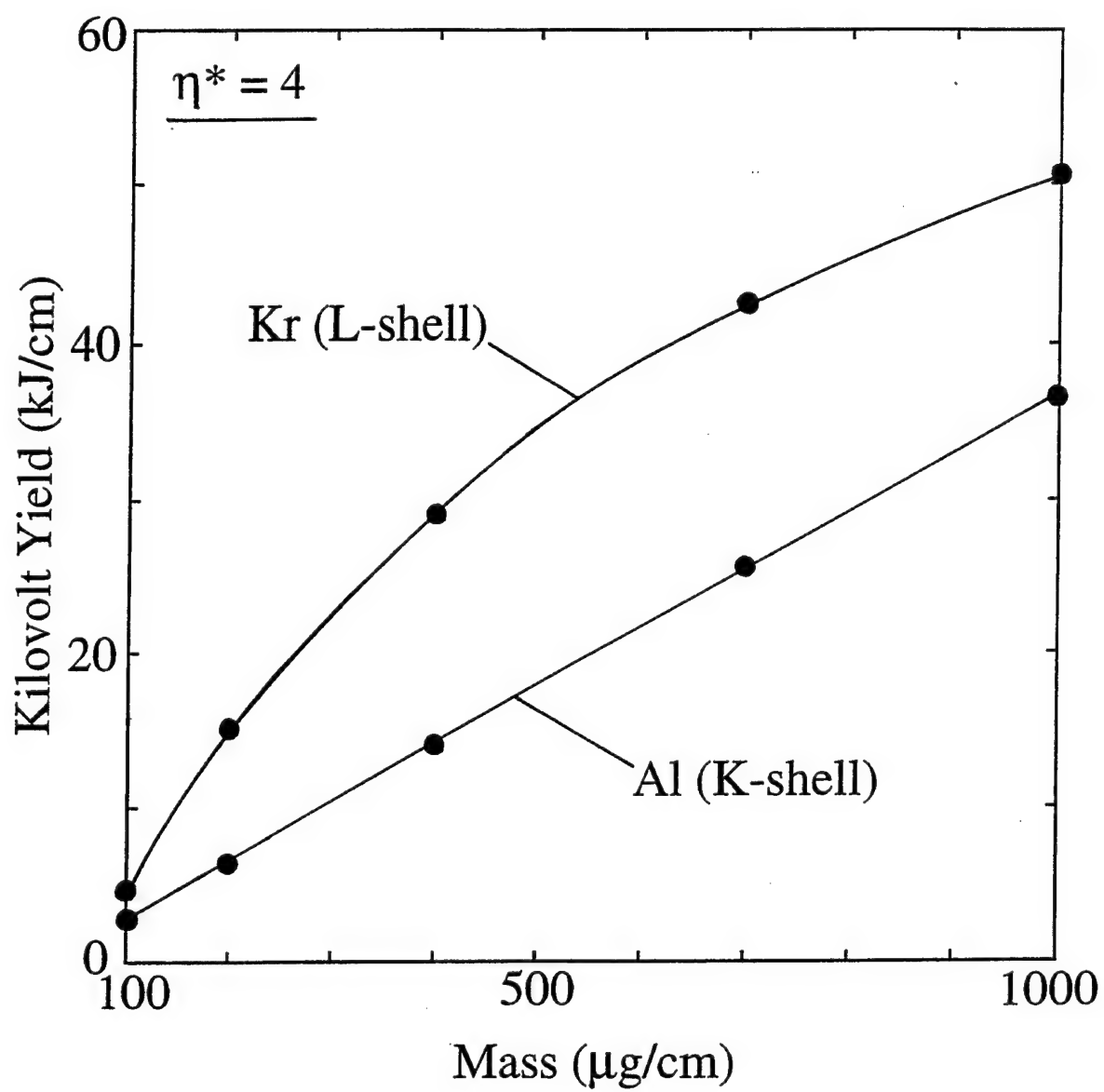


Figure 4

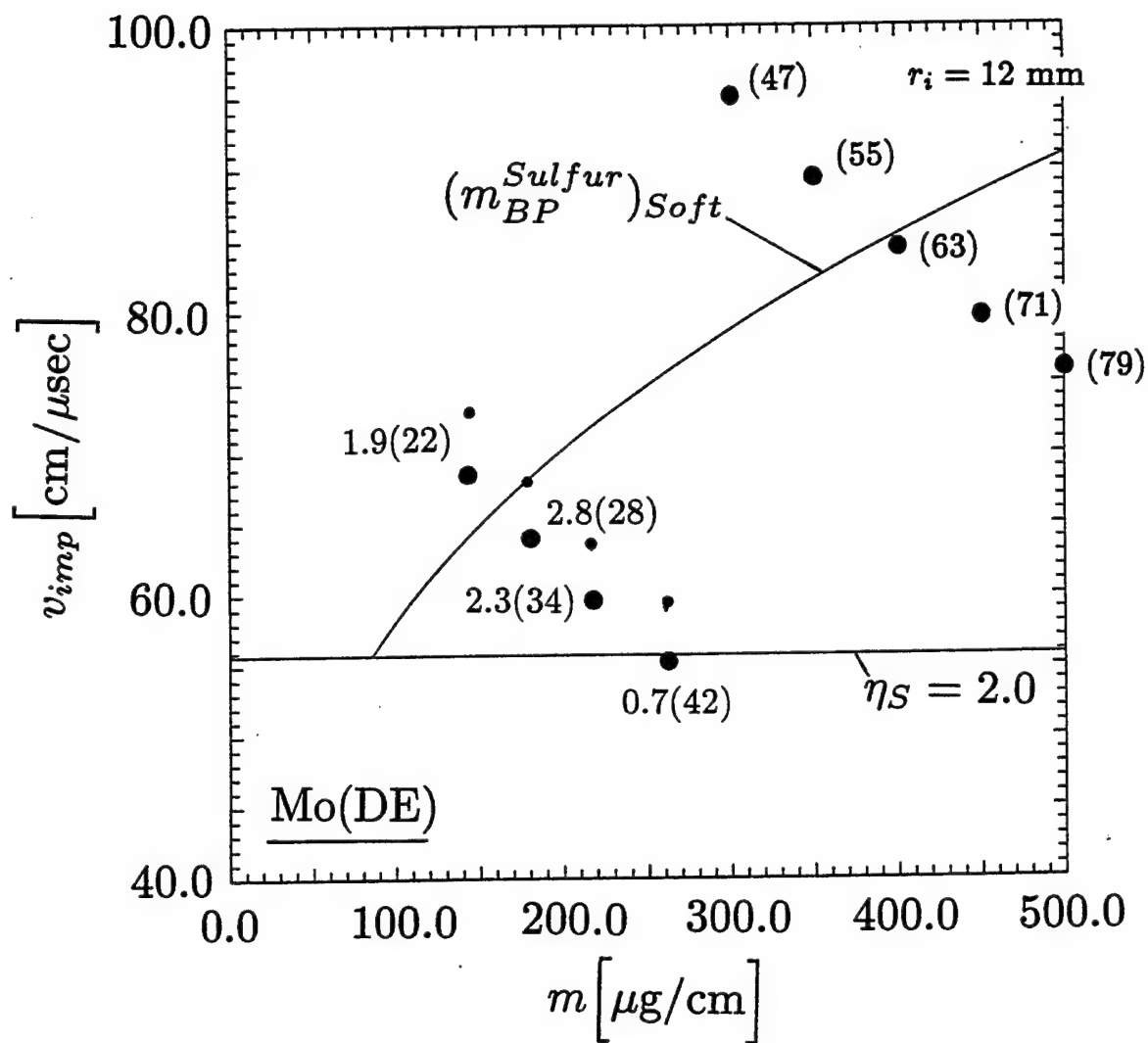


Figure 5

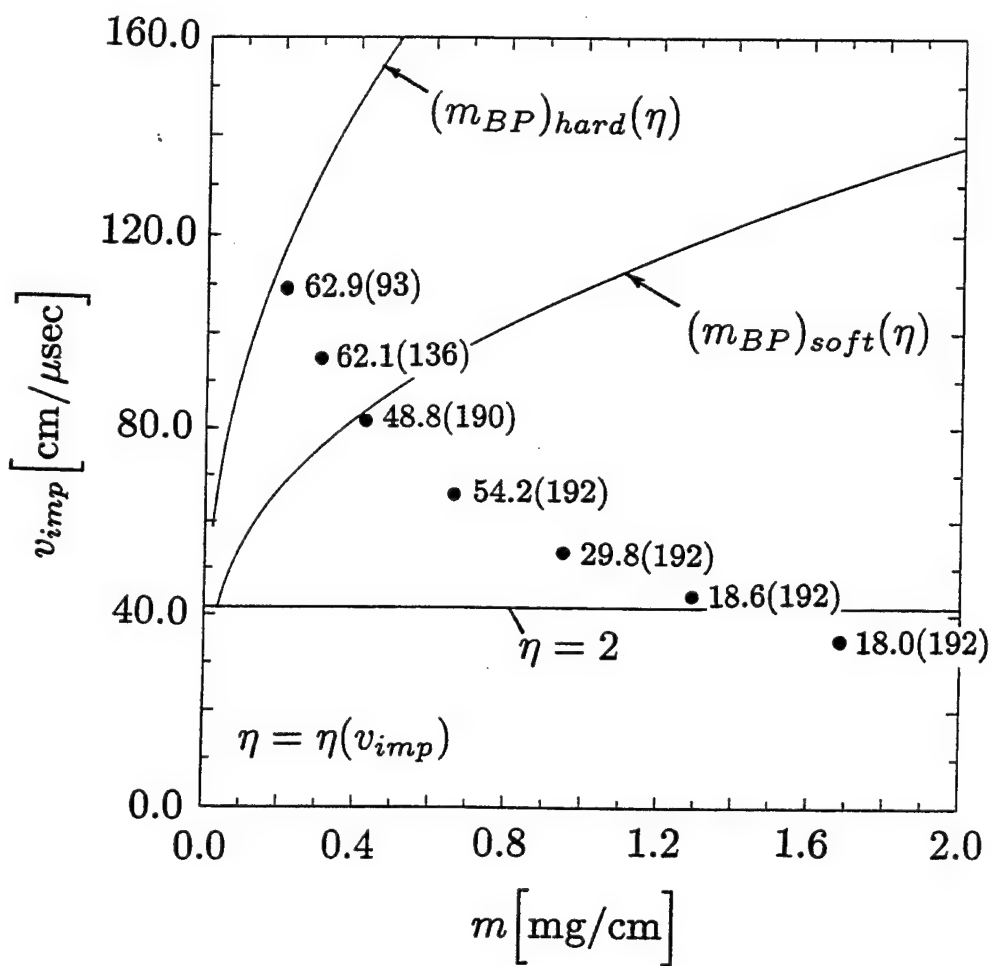


Figure 6

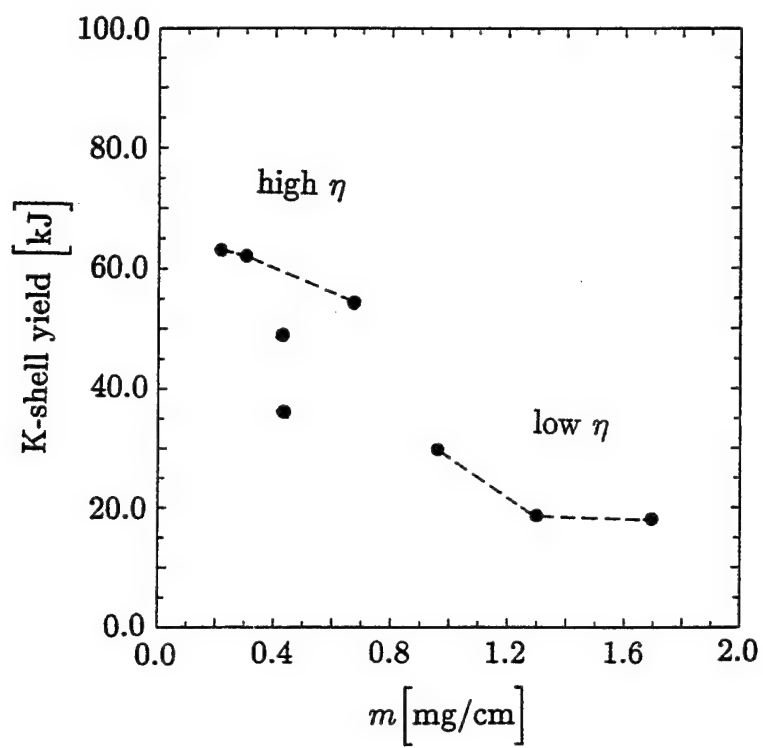


Figure 7

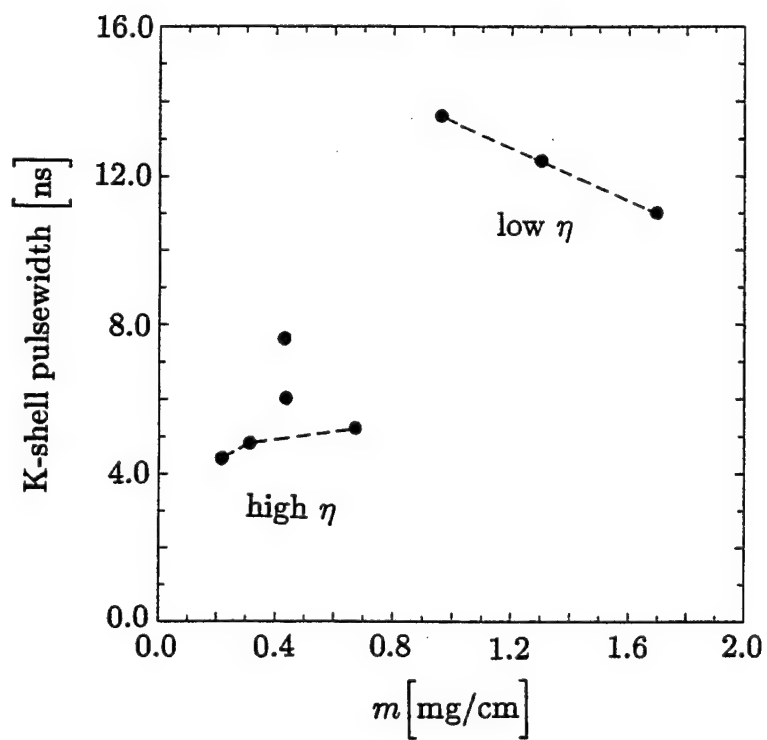


Figure 8

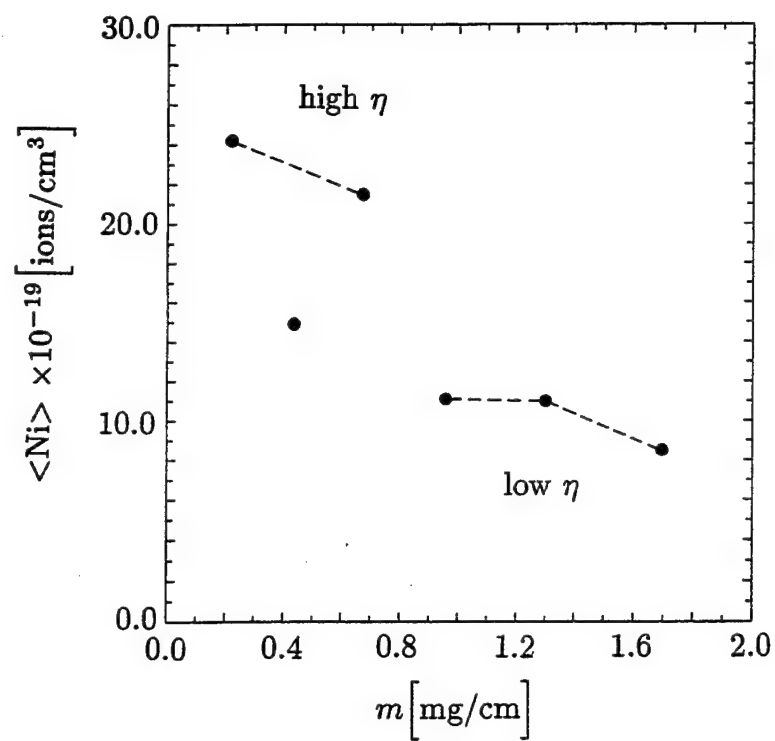


Figure 9

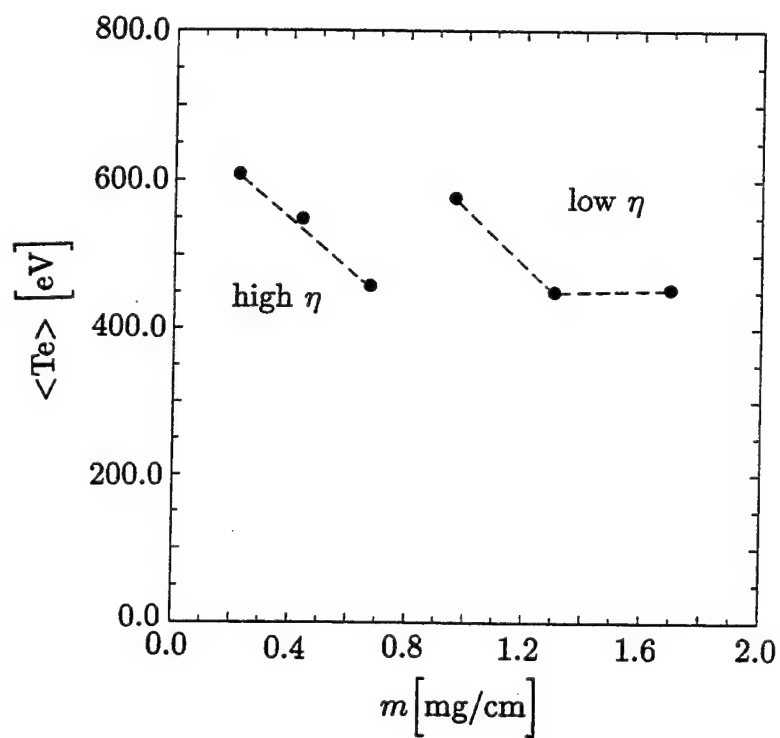


Figure 10

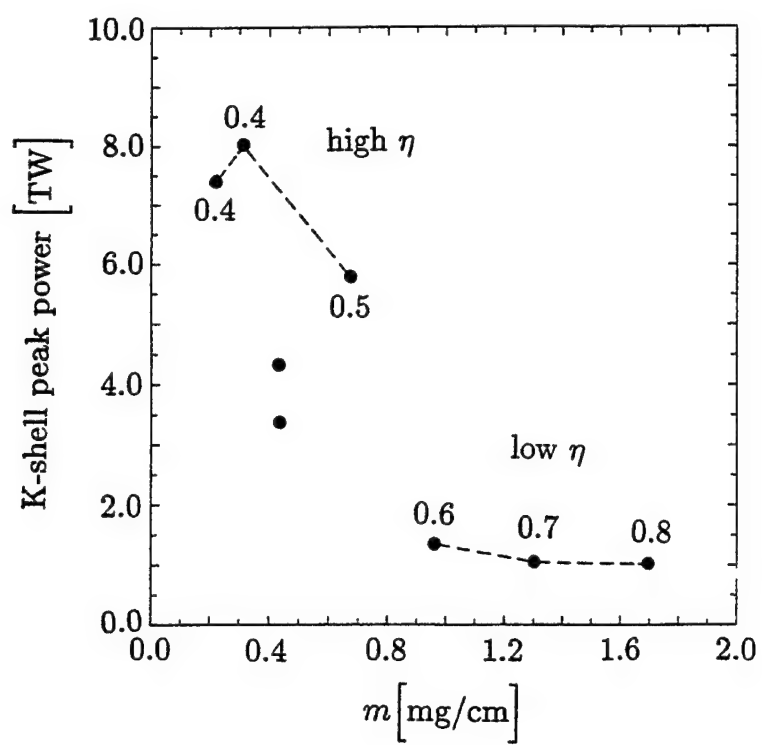


Figure 11

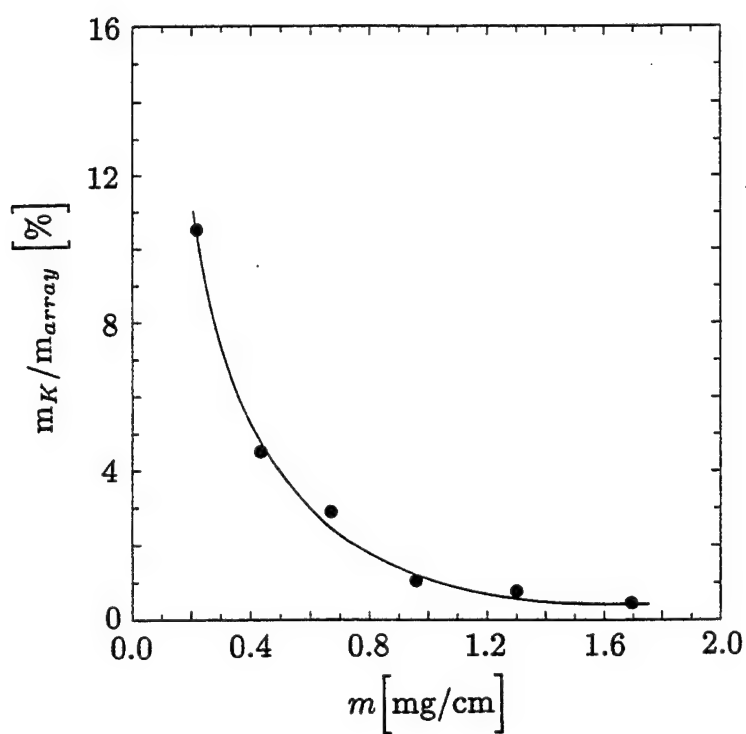


Figure 12

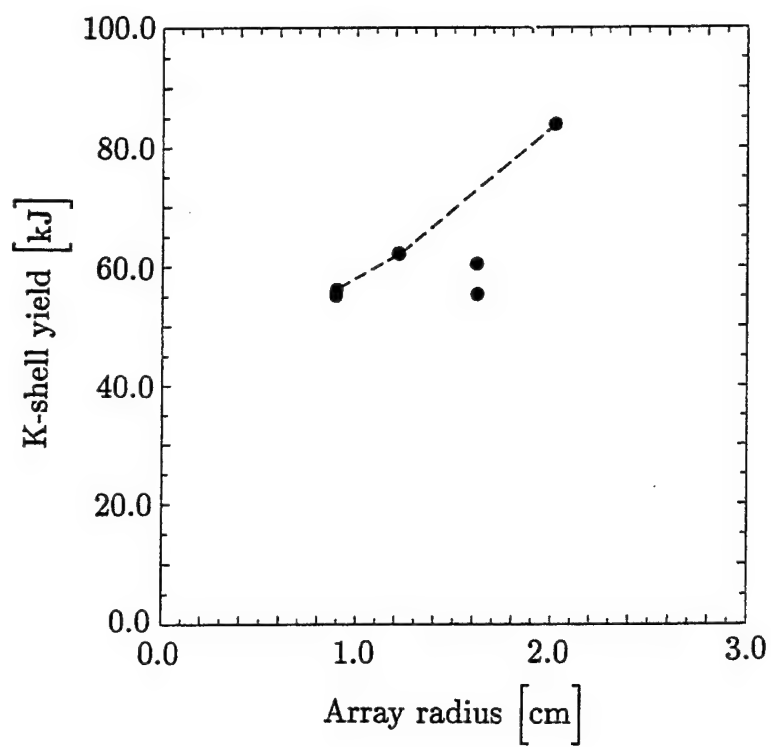


Figure 13

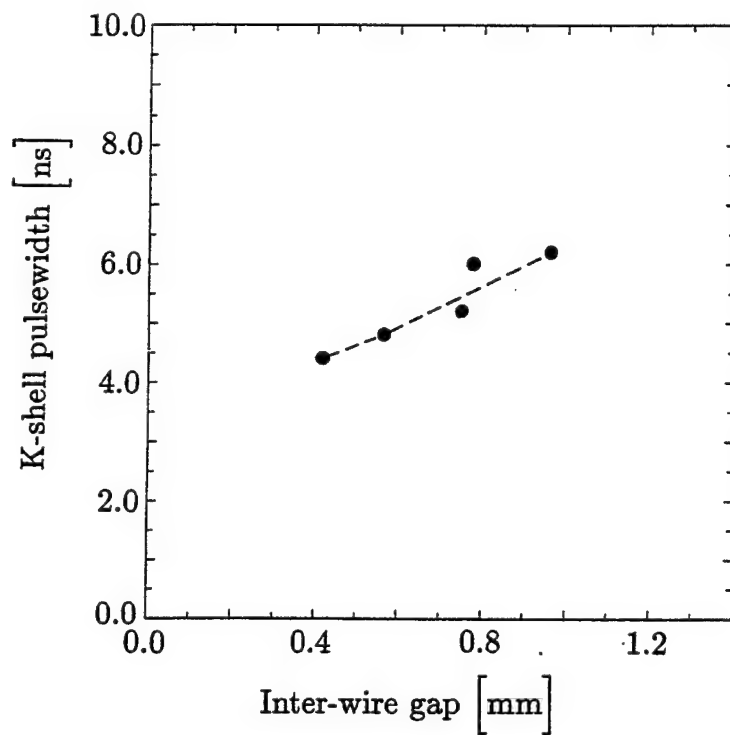


Figure 14

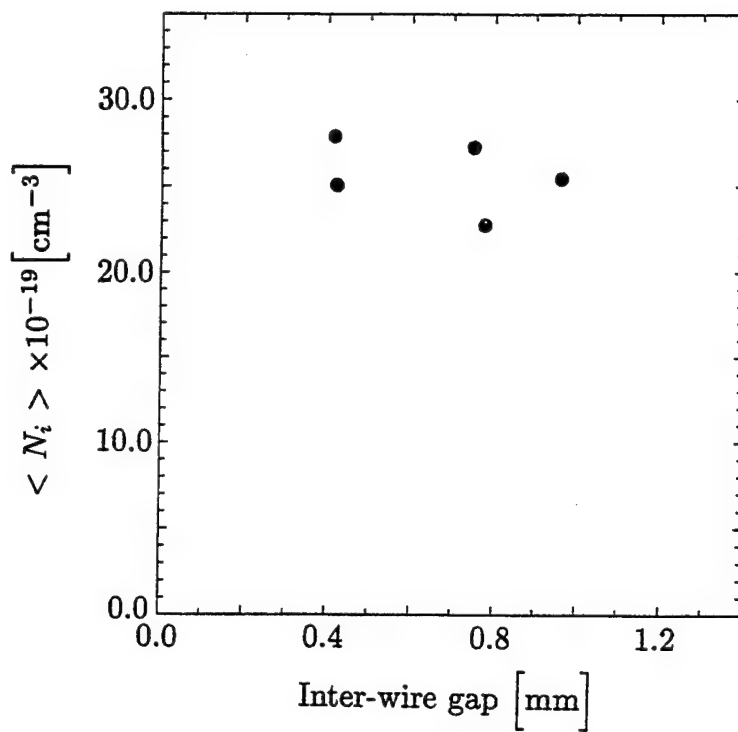


Figure 15

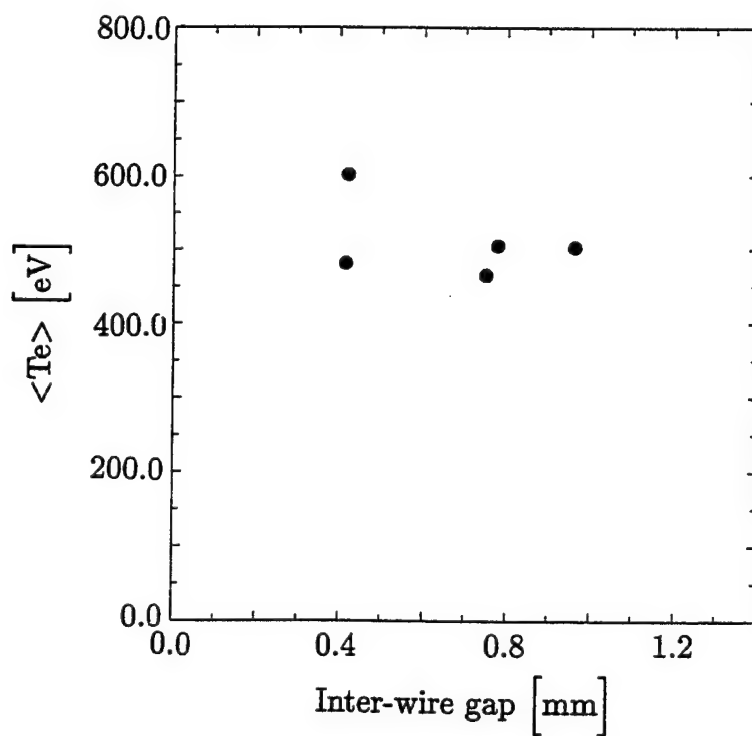


Figure 16

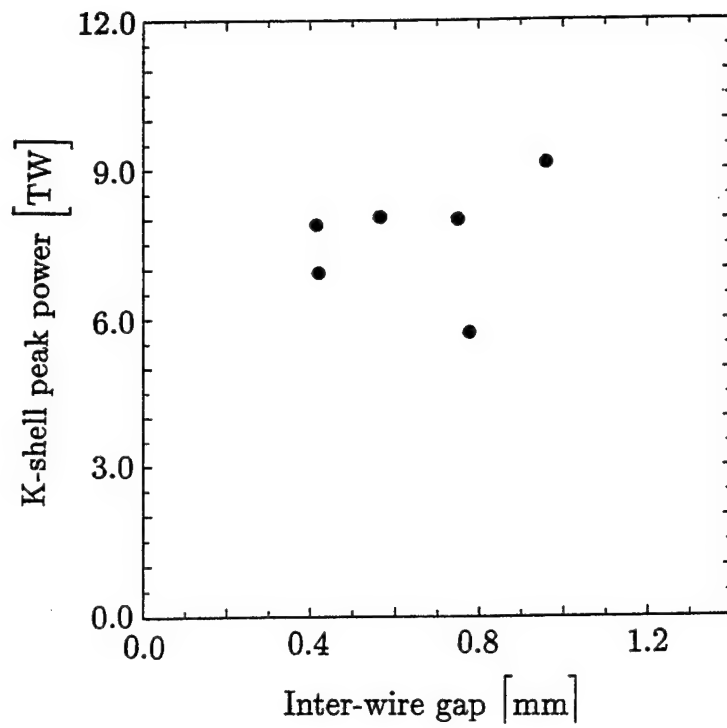


Figure 17

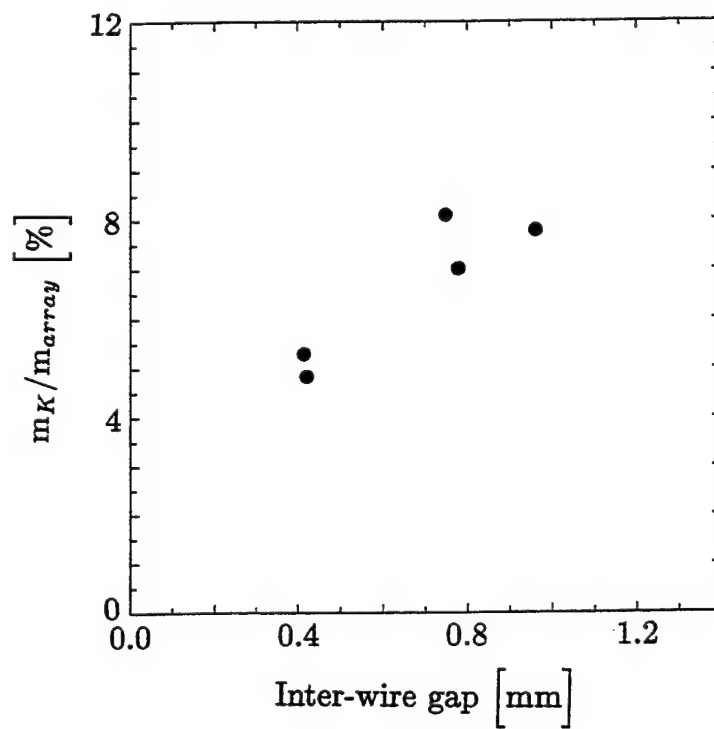


Figure 18

II. DETAILED ANALYSIS OF ALUMINUM PINCHES DRIVEN BY THE Z GENERATOR

A. INTRODUCTION

For more than a decade, pulsed-power generators have been used to implode Z-pinch loads with currents of several MA or more to produce copious yields of x-rays of energies exceeding 1 keV¹⁻¹⁵. These x-rays are usually produced by emission processes in the H- and He-like ionization stages of the load element(s), i.e., the K shell. Most of the work discussed in Refs. 1-15 employed wire arrays of Al or Al coated by or alloyed with Mg, although experiments have also been reported using Ar gas puffs^{5,13}. The new experiments on the Z generator reported and analyzed here used Al:Mg alloy wire loads. Prior to the advent of the 7-9 MA Saturn generator at Sandia National Laboratories^{9-12,14,15}, most of the experiments were conducted on three machines each of which had peak currents near 4 MA: Blackjack 5, at Maxwell Laboratories¹, Double EAGLE, at Physics International Corp.⁴, and Phoenix, at the Naval Surface Warfare Center⁶.

As the experimental and theoretical work progressed, considerable insight was gained into the coupled load and generator physics which affect x-ray production in such experiments. The initial experiments¹ on Blackjack 5 employed six, 3-cm long Al wires and imploded a mass load of 0.12 mg/cm from an initial radius of 7.5 mm in 70 ns to optimize the Al K-shell yield at 20 kJ. Succeeding experiments on Double EAGLE used 12 wires, at an initial radius of 6.25 mm, each 2-cm long, and a mass load of 0.28 mg/cm. These 95 ns implosions improved the Al K-shell yield to 35 kJ⁴. The remainder of the experiments discussed here all used 2-cm long wires. Evidence from Phoenix experiments also indicated that use of more wires and the attendant symmetrization of the implosion could enhance the x-ray yield⁶. More recent experiments⁸ on Double EAGLE produced Al K-shell x-ray yields of up to 55 kJ, by imploding an 18 wire Al mass load of 0.25 mg/cm

from an initial radius of 12.75 mm. Another series of Double EAGLE experiments⁷ used Al wires coated with Mg to take advantage of the fact that the total K-shell emissivity of two nearby atomic number elements can exceed that of either element alone due to opacity effects¹⁶. These experiments produced Al+Mg K-shell yields of up to 58 kJ, using 12 wires, 0.3 mg/cm, imploded in 87 ns from an initial radius of 7.5 mm. These conditions produced only 32 kJ from pure Al wires, demonstrating the predicted opacity effect¹⁶.

The trend of more wires leading to better symmetrization of the implosion, and improved K-shell yields continued in experiments performed on Saturn¹⁴. Comparison of shots taken with 24, 30, and 42 Al wires showed that tighter pinches, and increased radiated powers and yields were obtained with the 30 and 42 wire experiments. The best Al K-shell yield to date on Saturn, 88 kJ, was obtained with a 30 wire array of mass 0.41 mg/cm, imploded from a radius of 12 mm with a peak load current of 7 MA. Machine-to-load coupling, plasma and fluid instabilities, thermalization of kinetic energy, pulse widths, radiative cooling, temperatures, densities, their gradients, and the fraction of the load that participates in the K-shell radiation are all contributing elements that interact to significantly affect the yields. The reader is advised to consult the original references cited above for detailed discussions of these issues. Ref. 17 provides a more general early review.

A further series of Saturn experiments^{9-12,15} explored wire numbers as high as 192. While it was found that the K-shell yields were not further enhanced, dramatic reductions in the radiation pulsewidths, and corresponding increases in the radiated power were noted as the number of wires increased from 10 to 192. These effects occurred monotonically as a function of wire number and for initial load radii of both 8.65 and 12 mm, and were observed for all photon energies between ~ 0.2 and ~ 9 keV. As N , the number of wires, increases, the gap g between the wires decreases from ~ 6 mm to 0.4 mm. At gaps greater than ~ 2 mm, the data and calculations^{9,15,18} suggest that the wires fail to merge prior to on-axis assembly, a phenomenon known as the "wire plasma" regime. At gaps smaller than ~ 2 mm (wire numbers greater than ~ 40), calculations suggest that the individual wire

plasmas merge, forming a plasma shell of decreasing azimuthal variation and thickness as N increases. The wire number increase results in increased compression, higher on-axis density, and decreased radiation pulsewidths. The shortest pulsewidths are ~ 4 ns, for $N \geq 90$, compared to the typical 10-30 ns achieved on the 4 MA machines and by the earlier Saturn experiments¹⁴. Another interesting effect: for pure Al wire arrays, the K-shell yield *decreased* for the gap spacings below ~ 2 mm¹⁵. This decrease has been interpreted as an opacity effect resulting from the tighter, denser pinches that are achieved with more symmetric implosions^{11,12}. This trend toward lower K-shell yields with higher N was mitigated in the shots that used a 95% Al: 5% Mg alloy, as the much more optically thin Mg produced 18% of the K-shell line yield, despite constituting only 5% of the pinch ions¹⁵. The work presented below demonstrates an accentuation of this effect at much higher load masses, on the Z generator.

In this chapter, we present and analyze results from the first Al:Mg alloy wire experiments performed on the 60 TW, 19 MA Z generator at Sandia National Laboratories^{19,20}. Section B describes the experiments and the diagnostic data collected from them. Section C analyzes this data, using detailed collisional-radiative equilibrium (CRE) models of Al and Mg, with emphasis on the K-shell radiation processes of importance at the very high load masses used. The results are summarized and discussed in the concluding Sec. D.

B. EXPERIMENTS AND DATA

This section describes the experiments and presents the basic diagnostic data obtained from shots on the Z generator using arrays of Al:Mg alloy wires. Brief interpretive remarks are also given when appropriate; they are intended to preview the detailed analysis presented in Sec. C. Z, the world's most powerful and energy-rich Z pinch driver, is described in Refs. 19 and 20. Z stores 11.4 MJ in 36 Marx generators, and can deliver up to ~ 2 MJ total energy to a load. Peak load currents are typically 16-20 MA, reached in ~ 105 ns. The

values of these quantities achieved in practice depend upon the detailed load configuration.

The basic parameters of the 95% Al: 5% Mg alloy wire experiments are given in Table I. A total of 6 Al:Mg wire shots were taken on Z; the three listed in Table I are the best characterized, and they include all of the mass loads used (1.3, 2.1 and 3.6 mg/cm). The shots are listed in descending mass load order. In each case, a peak load current of 19 MA was achieved. An implosion time of 106 ns for each shot was assured by keeping mr^2 constant, where m is the mass of the load array and r is its initial radius. The experiments therefore tested the effect of varying the load mass on the pinch properties. The large number of wires employed, at least 180 in each case, was designed to insure that the implosion dynamics were characteristic of the plasma shell rather than the wire plasma regime. The gap between the wires was 0.53 mm for the medium- and high-mass shots, and 0.59 mm for the low-mass, 1.3 mg/cm shot. These gaps are fairly close to the smallest interwire gap of 0.4 mm used in the Saturn shot campaign⁹. Even so, the K-shell pulsewidths of 13-20 ns were well above the Saturn best of ~ 4 ns achieved at 0.4 mm gap, and also the ~ 5 ns at 0.6 mm (no Saturn shots were taken at 0.53 mm). This pulsewidth increase may be due to a number of factors, such as the larger initial array radii²¹, increased implosion time, and reduced current prepulse compared to the Saturn experiments. These differences tend to increase the growth of Rayleigh-Taylor instabilities and any initial asymmetries present in the load/return current structure, and potentially may increase the seed for the instability. The K-shell yields increased with decreasing load mass; another 1.3 mg/cm shot not shown in the table achieved 160 kJ.

Each Al atom requires a minimum energy of ~ 12 keV to strip its M and L shell electrons and heat them to a temperature conducive to efficient production of K-shell radiation. The η parameter² shown in Table I is the factor by which the calculated implosion kinetic energy of ~ 1 MJ exceeds this minimum for each load mass. Given its much larger current, the kinetic energy that Z imparts to its loads exceeds that of Saturn^{11,14} by a factor of 4 or more. Therefore, the masses used are several times those employed on Saturn. It is both

predicted and observed that heating much more Al:Mg to the K shell results in much more K-shell radiative yield. The Z data (Table I) shows a strong dependence on η , and the optimum η has yet to be explored.

Two instruments provided diagnosis of the sizes of the compressed pinch in both L- and K-shell emissions. Here, the pinch diameter is defined as the full-width-at-half-maximum in intensity, averaged along the pinch axis. A large format pinhole camera²² was filtered by 4- μ m Kimfol and 160-A Al to give an overall sensitivity to photons of energy 180-280 eV, and also above 800 eV. This camera supplies time resolved frames, which will be referred to as the L-shell images. For instance, near peak power, the 2.1 mg/cm Shot 70 has an L shell diameter of 5.7 mm. The K-shell diameters were obtained by a radially resolving, time-integrating crystal spectrometer, which recorded K-shell radiation from both Al and Mg between energies of 1.3 and 2.7 keV. From Table I, these K-shell diameters vary from 1.8 to 2.5 mm, and because they are time integrated, must be considered an upper limit to the K-shell pinch size at the time of peak K-shell power. The fact that the L-shell pinch size is at least 3 times that of the K shell is a common phenomenon, see, e.g., Refs. 4 and 23 for similar data on Double EAGLE, and Ref. 14 for Saturn.

Detailed time-resolved, spatially integrated Al K-shell spectra were provided by a second spectrometer, which, however, could not record the lower energy principal Mg K-shell lines. At yet higher photon energies, five absolutely calibrated broadband filtered diamond photoconductive detectors (PCDs)^{11,24}, obtained the time-resolved power at photon energies of 3.35, 3.65, 5.0, 6.0, and 7.7 keV. An example of a time-integrated spectrum is shown in Fig. 1, which focuses on the 1-2 principal resonance lines (the α lines) of both Mg and Al (Shot 70). In the present work, He α refers to the summed intensities of the $1s^2-1s2p^1P$ and $1s^2-1s2p^3P$ lines. Despite constituting just 5% of the plasma ions, the Mg lines are far stronger than 5% in relation to those of Al. The summed intensities of the two Mg α lines is 31% of that of the Al lines for Shot 70, 28% for Shot 71, and 21% for Shot 72. This is a strong indication that self-absorption is restraining the

yield of the Al lines much more than that of their Mg counterparts, whose optical depths are nearly 20 times smaller than those of Al.

The time-resolved K-shell Al spectrum at the peak of the K-shell power is shown for Shot 70 in Fig. 2. Table II presents some key line ratios, both time-resolved and time-integrated. There is virtually no difference, comparing peak power values to time-integrated ones, in the Ly α to He α ratios for Al. However, a striking difference is seen in the ratios of the 1-3 β lines to the α lines, for both ionization stages and for all 3 shots. These time-resolved ratios are 1.4-2.1 times greater than the time-integrated ones. As in the Saturn experiments analyzed in Ref. 15, peak power is evidently being produced by high pinch compression. The high pinch densities associated with peak power also maximize K-shell line opacity, allowing the β lines to more closely approach the α lines in intensity, thereby accounting for the difference in time-resolved and time-integrated β/α ratios.

Another interesting, and seemingly anomalous feature of the data is evident in both Fig. 1 and Table II. For all three shots, the time integrated Ly α /He α ratio for Al is well in excess of that of Mg. For alloy loads such as those employed in these experiments, there can be no spatial separation of the elements, therefore, the Mg pinch ions are exposed to the same plasma conditions as those of Al. Since Al's atomic number is higher than that of Mg, a higher temperature is required to ionize it from the He-like to the H-like stage. For the same temperature, in a purely collisional plasma, there should be a greater fraction of H-like Mg present than of H-like Al. Why then, do these ratios indicate the opposite, that there is more H-like Al? The physics behind this effect is explored in the next section, and is connected to the high masses and optical depths of the loads.

C. ANALYSIS

Model

The principal tool which we have used to analyze the extensive x-ray data collected from these experiments is a one-dimensional (1D), cylindrical plasma CRE model containing

detailed configuration atomic structure for the Li-, He-, and H-like ionic stages of Al and Mg. This model is described in more detail in Ref. 25. All optically thick lines are transported, as well as the two free-bound continua arising from radiative recombination to the K-shell ground states of Al and Mg. Although Z pinches, which show evidence of kink and sausage instabilities, and Rayleigh-Taylor bubbles and spikes, are not perfectly one-dimensional, our use of a 1D model employs the detailed radiation models necessary for a meaningful and fruitful analysis of the x-ray data. Such models are not available for 2 or 3 dimensional geometries. More importantly, the many years of experiment and analysis cited in the introductory section has revealed that definite trends exist in the average pinch properties as a function of radius, despite variations in the pinch properties along the axis. One clear evidence of this is the nearly universal finding that pinch diameters are larger when imaged at lower x-ray photon energies^{4,14,23,26}. One-dimensional analyses have been invaluable in deriving average pinch properties and thereby spotting trends in experimental campaigns in which load conditions have been systematically varied for a number of shots^{1,3-5,12,14,15}.

Average pinch conditions

The conceptually simplest analysis that we apply to the three shots listed in Table I has been described in Refs. 3 and 25. In such an analysis, the objective is to derive the average pinch properties and the method used is to match both the Ly α to He α line ratio and total K-shell power per unit length. Detailed CRE calculations of these quantities are displayed in the form of isocontours vs. density and electron temperature. The intersection point of the contours at the observed values gives the average pinch temperature and density. When this is done for the 3.6, 2.1, and 1.3 mg/cm Z shots, the electron temperatures obtained are, respectively, 1.0, 1.0, and 1.1 keV, and the ion densities $0.6, 1.2, \text{ and } 0.9 \times 10^{20} \text{ cm}^{-3}$. Note that the time-resolved and time-integrated α line ratios are nearly identical, so that using these ratios coupled with the peak K-shell power gives essentially no difference between

the time-resolved and time-integrated diagnoses. The most striking variation, however, occurs in the derived fractions of the original load mass that participate in the K-shell radiation, which are, in the same order, 2%, 7%, and 15% of the load mass. Such low mass fractions have also been inferred from the Saturn high-wire-number experiments^{11,12,15}. Note that all of the mass implodes to the vicinity of the axis as verified by the success of a slug model in predicting the implosion time. The K-shell radiating mass represents the approximate fraction of the imploded mass which is hot enough to radiate K-shell x-ray photons. A more detailed analysis using time-resolved data, as discussed below, shows that this is a reasonable interpretation. A similar analysis has been performed for Al wire shots on Saturn, and is summarized in Fig. 13 of Ref. 14. The Saturn analysis shows a monotonic decline with load mass of both K-shell radiating mass fraction and yield for total load masses above 0.4 mg/cm. This behavior is similar to the present Z result quoted above.

Temperature-density profile for Shot 70

Obtaining average pinch conditions by spectroscopic analysis has been valuable in discerning basic trends in shot campaigns in which load and/or machine conditions have been systematically varied. However, the basic goals of elucidating (1) the detailed processes by which radiation is produced, (2) whether efficiently or inefficiently, and (3) to what extent it is absorbed in the pinch, and also, e.g., (4) why soft radiation often dominates the spectral output, require diagnosis of the space and time dependent properties of the pinch (see, e.g., Refs. 11, 12 and 27). The most complete data set available from these experiments is that of the medium mass load (2.1 mg/cm) Shot 70. Our objective was to obtain a temperature-density profile, which the CRE model calculates to emit x-rays consistent with the radiation data from this shot at the time of peak K-shell power. In practice, this was accomplished by initially using analytic forms such as Gaussians and power laws to represent the radial variations of temperature and density. In this work, the power law exponents and Gaussian

widths were varied over $\sim 10^4$ separate CRE calculations to determine electron temperature and ion density profiles that produce a reasonable approximate spectral fit, which was then optimized using cell-by-cell adjustment of the temperature and density.

This fitting procedure was subjected to the following finite set of constraints. The profiles had to produce agreement within experimental/theoretical uncertainty for at least the α and β lines of both K-shell stages of Al. To provide one measure of the uncertainties inherent in the model spectral calculations, recent comparisons of experimentally measured electron collisional excitation cross-sections of the He α lines of highly charged He-like ions²⁸ may be consulted. The work reported in Ref. 28 showed departures from theory averaging 11% at the excitation thresholds, with a maximum departure of 25%. The calculations also were required to predict the observed peak K-shell power of 7.2 TW, with the full 2.1 mg/cm mass load. The temperature profile had to be consistent with a K-shell radiating core no larger than 1.8 mm in diameter, and an L-shell diameter of 5.7 mm. Because the Mg lines were only observed time-integrated, it was not possible to require precise agreement for Mg at any single time during the pinch lifetime. However, the profiles had to provide at least a qualitative explanation for the fact that the Ly-to-He α line ratio of Al exceeds that of Mg, and they had to also be consistent with the Mg α lines being about 30% as intense as those of Al, despite Mg constituting only 5% of the pinch ions. The temperature profile shown in Fig. 3a and the density profile of Fig. 3b meet these constraints. It is not possible to prove rigorously that these profiles constitute a unique fit. However, the temperatures and densities have been both increased and decreased from the best fit profile values in every radial region, invariably resulting in deterioration of the agreement with experiment. For further discussion of the uniqueness issue, coupled with an example from some Saturn experiments, see Ref. 27.

Modeling of K-shell emissions has been improved and refined by more than a decade of detailed comparisons between Z-pinch experiments and theoretical calculations. Additional confidence is gained due to the relative simplicity of the atomic physics of 1- and 2-electron

ions. Such is not the case for both experimental and theoretical endeavors involving the more complex L-shell stages, for which no detailed x-ray spectra were collected in these experiments. Given the relative lack of maturity of the state-of-the-art of L-shell modeling, no requirement for agreement with the L-shell power was imposed. A note on numerics: 10 radial cells were used for the many coarse scoping runs, 20 for optimization, and 40 to check convergence. The 20-cell results are plotted in Figs. 3a and b.

A salient feature of these profiles is that outside a diameter of 1.4 mm, the pinch electron temperature is less than 0.1 keV, indicating a pure Al:Mg L-shell radiator consistent with the K- and L-shell pinhole images. We will refer to this outer region of the pinch as the "halo" and the portion inside it as the "core"^{10,11}. The temperature profile of the halo is only coarsely determined due to the lack of L-shell spectra, but its upper temperature limit of 0.1 keV assures that no significant K-shell emission emanates from it. Key x-ray optical depths, measured along the radius, are, for Al He α , 664, for Ly α , 53, at the threshold of the He-like recombination continuum, 1.2, and at the threshold of the H-like recombination, 1.6. The continuum optical depths exceed unity due to the large load masses; this is qualitatively different from other K-shell Z pinch experiments to date that used load masses several times smaller than Z is able to implode. In previous experiments, K-shell continuum optical depths were less than unity and the resulting free-bound photon absorption was small. In deriving the Fig. 3 profiles, an ion temperature of 20 keV was assumed, consistent with the width of the Mg He α line, which is relatively unaffected by opacity or Stark broadening. This ion temperature is similar to that measured in the high-wire-number Saturn experiments^{11,12}. The core/halo property of the profiles show that two processes produce the collisionally unexpected Ly α /He α ratios. These are: (1) absorption of the He-like Al resonance line in the cool blanket, and, (2) photopumped ladder ionization due to photoexcitation followed by collisional ionization. These are now discussed in turn.

It must be kept in mind that the Mg comprises only 5% of the pinch ions, resulting

in much lower optical depths for the Mg K-shell resonance lines compared to their Al counterparts. Thus, absorption processes that greatly affect the Al lines are absent or minimal for Mg. The pinch blanket is too cool to contain any H-like Al or Mg. Therefore, the H-like lines formed in the core will pass through this region unaffected. Such is not the case for the He-like stage, which is much more easily populated by ionization of the low-threshold Li-like species. Although the blanket is too cool to produce excited states of He-like Al, considerable He-like Al is present in the non-radiating ground state. For example at a radius of 0.9 mm, where there is a corresponding electron temperature 85 eV, 10% of the Al ions are in the He-like ground state. A portion of the Al He α line formed in the core is thus absorbed and collisionally quenched in the blanket. This process has the effect of increasing the Ly α /He α ratio for Al, but not affecting the much less optically thick Mg. This mechanism accounts for some of the difference in the Ly-to-He resonance line ratios of Al and Mg. The effect is illustrated in Figs. 4a and b. Fig. 4a shows the calculated spectrum emitted from the core only, whereas 4b is the spectrum calculated to be produced from the full best-fit profiles of Figs. 2. A comparison of Figs. 4a and 4b reveals that the halo has no effect on the H-like lines because it contains no H-like ions, but that it reduces the intensity of the optically thick He-like lines by self-absorption. The Ly α /He α ratio emitted by the core only is calculated as 2.2, but the halo increases it to 2.7.

The emitted line intensities are accurately calculated within the CRE model using a multicell-coupling technique for radiative transfer²⁹. This method is based on line-profile-averaged escape probabilities differentiated across the cell boundaries, and thus it cannot calculate the emergent line profiles. To facilitate visual comparison, the calculated spectral lines have been plotted in Figs. 4 as Gaussians with the same widths (from all sources) measured by the time-resolving spectrometer. The calculated intensities of the Al K-shell lines fit the measured, time-resolved ratios of the α and β lines at the peak of shot 70's K shell power to better than 19%.

The other effect boosting the Al Ly-to-He resonance line ratio is photopumped ladder

ionization. If ionization of the two elements were controlled solely by electrons, then in the identical environment Mg would be stripped further than Al. However, the ambient photon field also plays an important role in Al. The best way to illustrate this photopumping is to consider in detail a specific numerical radial cell (the 5th cell from the center in the 20-cell best fit profile calculation). The electron temperature in this cell is 470 eV, the Al ion density, $7 \times 10^{20} \text{ cm}^{-3}$. The collisional ionization rate from the ground state is $2.3 \times 10^9 \text{ sec}^{-1}$, but from the excited states, summed over their fractional populations, the ionization rate is $2.0 \times 10^{11} \text{ sec}^{-1}$. Even though the excited states carry just 5.5% of the He-like population, their greater energetic proximity to the H-like ground state results in much higher ionization rate coefficients and therefore they dominate the ionization. The same best-fit profile calculation was rerun assuming that the plasma was optically thin at all x-ray energies, and this resulted in the He-like excited states carrying only 2% of the He-like population, due to the absence of line self-photopumping. The smaller excited state populations reduced the ionization rate proportionately, to $7.7 \times 10^{10} \text{ sec}^{-1}$. For the much thinner Mg component, enhancement of ionization due to line photoexcitation is much less important. As a result, the H-like population fractions of both the Al and Mg are calculated to be 0.35 in the optically thick case, whereas if both components are thin, the fraction of H-like Mg exceeds that of Al by $\sim 25\%$.

Another noteworthy feature of this analysis is revealed by the comparison of predicted and measured absolute powers at high photon energies. Recall from Sec. B that five absolutely calibrated diamond PCD's measured the time-resolved power at photon energies of 3.35-7.7 keV. Fig. 5 shows how these measurements compare with the model predictions from the best-fit profile calculation. Note that the excellent agreement, within a few percent, at photon energies of 3.35 and 3.65 keV, progressively deteriorates at higher energies. At 7.7 keV, the measured power exceeds the calculated power by a factor of 9. Clearly, the pinch contains some high energy electrons not accounted for in the best-fit profile. Such electrons may be in a localized spatial region so hot that the Al and Mg are stripped to the

bare nucleus, therefore having no effect on the emitted line spectrum, and diagnosable only through the continuum measurements. Alternatively, the fundamental electron distribution may be non-Maxwellian, with a secondary high-energy peak. Differentiating between these possibilities or combination thereof is beyond the scope of this work and is reserved for the future. Experimentally, 15% of the K-shell yield is at energies above 5 keV, 25% above 4 keV.

Another interesting facet of the Al:Mg wire experiments on Z is revealed by comparing them to a different series of experiments also conducted on Z³⁰, employing Ti (Z=22) wire arrays. Titanium's K shell lines lie at ~ 4.8 keV, and it requires 6 times the energy per atom as it does for Al to strip and heat Ti to radiate in the K-shell. Thus it may at first seem puzzling to learn that the best Ti K-shell yield on Z of 150 kJ is nearly equal to the Al:Mg maximum of 160 kJ. The likely explanation for this surprising result lies in the fundamental scaling of K-shell opacity with increasing atomic number. Assume that the line widths are dominated by Doppler broadening due to the high ion temperatures achieved on Z. For the same mass density profile, it is straightforward to show that the line optical depths of Ti are 4 times lower than those of Al. Similarly, the optical depths of the K-shell radiative recombination continuum are 5 times lower for Ti than Al. Even after being self-absorbed, many line photons can scatter out of the pinch by being repeatedly re-emitted, and the extent of this scattering is limited by collisional quenching of the excited states during the re-emission process. This process is significant for both Ti and Al, but the collisional quenching per absorption for Ti is a factor of 40 lower than that of Al. In summary, all of the fundamental atomic parameters tend to sharply reduce the effect of opacity in restraining the emission of both lines and continua, for the K-shell, as atomic number increases. The CRE best-fit profile calculation was redone assuming the Al was optically thin, resulting in a fivefold increase in emitted K shell power. Using the same mass density and temperature profiles, Ti was then substituted for Al in the same two calculations, resulting in essentially no difference between the thin and thick results. Therefore both experiment and theory

indicate that, on the Z accelerator, the Al K-shell yield is being strongly restrained by self-absorption, but that of Ti is not.

We have presented average conditions in the pinch for the three different mass load shots on Z. It was found for shot 70 that 7% of the ions in the initial mass load were responsible for radiating the K-shell photons. Does this make sense when compared with the detailed best-fit profile? Fig. 6 shows the fraction of the pinch mass which lies above a given electron temperature, indicating that 7% of the pinch lies above 300 eV. The K-shell emissivity of Al peaks at about 1 keV, and is $\sim 20\%$ of its peak value at 300 eV. Given the broad temperature distribution over which Al radiates K-shell photons at some level of efficiency, there can be no rigorous definition of "radiating mass fraction". However, by comparing the analysis of one-cell, average pinch conditions with the more in-depth detailed profile and defining an efficiency cut-off at 20% of peak emissivity one finds an exact correspondence between the radiating masses obtained with both methods.

D. SUMMARY AND DISCUSSION

The history of the development of Z pinches as x-ray sources has demonstrated that, when higher-current, more energetic drivers can be built, higher yields of K-shell photons as well as photons of all energies are invariably achieved. As the energies imparted to the loads have increased, so have the masses of the loads, and the ability to strip a greater number of atoms to the desired ionization stages has been a major factor in the increased yields. However, the greater mass inevitably results in greater opacity of the Z-pinch plasma, and at some point self-absorption can prevent the yields from scaling even linearly with the mass, as the pinch transitions from a volume to a surface radiator. The results from the Z generator presented here indicate that this transition is well underway for the K-shell lines and continua of Al for mass loads of 1.3-3.6 mg/cm. Such is not the case for Ti, because, as atomic number increases, the effects of opacity on K-shell emission are sharply reduced. To recover high efficiency emission in the 1-2 keV photon energy regime, at least two

strategies are possible but their usefulness needs to be demonstrated by future experiments. One involves the judicious use of mixed element loads^{7,16} which has shown some success in the past on lower-current machines. Another option is to use higher atomic number L-shell radiators.

The high optical depths achieved on Z have enhanced some radiation effects that noticeably affect the x-ray spectra. These processes, photopumped ladder ionization, and absorption of the He-like lines in the cool pinch blanket, distort the Al Ly-to-He α line ratio to the point that it exceeds the same ratio of the lower atomic number Mg component. The Mg is not affected significantly by these processes, because it comprises only 5% of the ions and is much less optically thick.

Another interesting facet of these experiments was not directly connected to opacity effects. The measured absolute power at 5 continuum energies from 3.35 to 7.7 keV showed excellent agreement with the best-fit model calculations at 3.35 and 3.65 keV. This agreement, however, deteriorated at higher energies to the point that, at 7.7 keV, the model underpredicts the power by nearly an order of magnitude. Solution of this discrepancy will probably involve a hot electron population, and is beyond the scope of the present work.

Recently, an aluminum-wire experiment similar to Shot 70 was carried out on the Z generator, and produced twice the K-shell yield and power as reported here for that shot. The reasons for these differences are not yet fully understood, and several factors might contribute. Typical discrepancies in PCD calibrations are 20%. Viewing a pinch along different lines of sight can result in detected power differences of up to 30%. Also, axial pinch nonuniformities can lead to errors in the extrapolation procedure used to infer the total power when the detectors are apertured and can view only a fraction of the pinch. This effect has caused discrepancies of up to 50% on tungsten pinches driven on Z, and at present appears to be responsible for about 20% of the K-shell power and yield differences between Shot 70 and the more recent experiment. Finally, there is an inherent degree of irreproducibility present in all Z-pinch experiments so that the possibility exists that the two

experiments, while similar in initial conditions, produced somewhat different implosion and assembly dynamics. These issues are always present in the acquisition and interpretation of Z-pinch data. Nonetheless, the high quality, consistent data reported here has allowed unambiguous inference of the pinch temperature and density profiles.

Finally, the derivation of best-fit temperature and density profiles at the peak of the K-shell power of Shot 70 raises an important challenge for magnetohydrodynamic (MHD) calculations. For example, one-dimensional (1D) MHD calculations have been successful in duplicating average electron temperatures, ion densities and K-shell emitting masses only when some of their fundamental transport coefficients have been adjusted^{12,31}. Moreover, recent calculations that leave the current on during the implosion phase¹² have tended to predict that both the K- and L-shell radiation are confined to narrow emitting zones resulting in much smaller differences between the K- and L-shell sizes than are seen experimentally. Pinhole camera images generally show that the L-shell emitting region is at least 2-3 times as wide as the K-shell region. Further adjustments of the transport parameters and initial conditions are needed to improve the MHD predictions of temperature and density profiles on axis.

With regard to 2D simulations: the observed, axially-integrated spectra are, in effect, spatial integrals of the K-shell emission weighted according to the K-shell emissivity of each distinct axial region. The same principle applies to the pinhole sizes, with the photon energy weighting factor given by the overall detector sensitivity folded with the filter transmissivities. When considering methods of comparing multidimensional calculations to the present experiments and inferred pinch profiles, a useful starting point might be to calculate the same weighted integral for the multidimensional simulations and compare the weighted, axially-integrated profiles to those of Figs. 3a and b. The most intensively investigated, and most frequently adjusted parameter in 2D MHD calculations has been the magnitude of the initial density perturbation¹⁵. How does this perturbation affect the density-temperature profile and is it possible to bring it into agreement with the one

presently inferred using a detailed configuration radiation model? By directly inferring the gradient structure of the K-shell emission region of ultrahigh optical depth pinches, one can better evaluate the usefulness and applicability of both 1- and 2D-MHD models.

REFERENCES

1. M. Gersten, W. Clark, J. E. Rauch *et al.*, Phys. Rev. A **33**, 477 (1986).
2. K. G. Whitney, J. W. Thornhill, J. P. Apruzese, and J. Davis, J. Appl. Phys. **67**, 1725 (1990).
3. M. C. Coulter, K. G. Whitney, and J. W. Thornhill, J. Quant. Spectrosc. Radiat. Transfer **44**, 443 (1990).
4. C. Deeney, T. Nash, R. R. Prasad, L. Warren, K. G. Whitney, J. W. Thornhill, and M. C. Coulter, Phys. Rev. A **44**, 6762 (1991).
5. C. Deeney, P. D. LePell, B. H. Failor, J. S. Meachum, S. Wong, J. W. Thornhill, K. G. Whitney, and M. C. Coulter, J. Appl. Phys. **75**, 2781 (1994).
6. K. G. Whitney, J. W. Thornhill, J. L. Giuliani, Jr. *et al.*, Phys. Rev. E **50**, 2166 (1994).
7. C. Deeney, P. D. LePell, B. H. Failor *et al.*, Phys. Rev. E **51**, 4823 (1995).
8. K. G. Whitney, J. W. Thornhill, J. P. Apruzese, J. Davis, C. Deeney, P. D. LePell, and B. H. Failor, Phys. Plasmas **2**, 2590 (1995).
9. T. W. L. Sanford, G. O. Allshouse, B. M. Marder *et al.*, Phys. Rev. Lett. **77**, 5063 (1996).
10. T. W. L. Sanford, T. J. Nash, R. C. Mock *et al.*, Rev. Sci. Instrum. **68**, 852 (1997).
11. T. W. L. Sanford, T. J. Nash, R. C. Mock *et al.*, Phys. Plasmas **4**, 2188 (1997).
12. K. G. Whitney, J. W. Thornhill, P. E. Pulsifer, J. P. Apruzese, T. W. L. Sanford, T. J. Nash, R. C. Mock, and R. B. Spielman, Phys. Rev. E **56**, 3540 (1997).
13. K. L. Wong, P. T. Springer, J. H. Hammer *et al.*, Phys. Rev. Lett. **80**, 2334 (1998).

14. C. Deeney, T. J. Nash, R. B. Spielman *et al.*, Phys. Plasmas **5**, 2431 (1998).
15. T. W. L. Sanford, R. C. Mock, T. J. Nash, K. G. Whitney, P. E. Pulsifer, J. P. Apruzese, and D. L. Peterson, "Systematic trends in x-ray emission characteristics of variable-wire-number, fixed-mass, aluminum-array, Z-pinch implosions", submitted to Phys. Plasmas.
16. J. P. Apruzese and J. Davis, J. Appl. Phys. **57**, 4349 (1985).
17. N. R. Pereira and J. Davis, J. Appl. Phys. **64**, R1 (1988).
18. B. M. Marder, T. W. L. Sanford, and G. O. Allshouse, Phys. Plasmas **5**, 2997 (1998).
19. M. K. Matzen, Phys. Plasmas **4**, 1519 (1997).
20. R. B. Spielman, C. Deeney, G. A. Chandler *et al.*, Phys. Plasmas **5**, 2105 (1998).
21. T. W. L. Sanford, R. C. Mock, R. B. Spielman, D. L. Peterson, D. Mosher, and N. F. Roderick, Phys. Plasmas **5**, 3755 (1998).
22. L. E. Ruggles, R. B. Spielman, J. L. Porter, and S. P. Breeze, Rev. Sci. Instrum. **66**, 712 (1995).
23. T. Nash, C. Deeney, M. Krishnan, R. R. Prasad, P. D. LePell, and L. Warren, J. Quant. Spectrosc. Radiat. Transfer **44**, 485 (1990).
24. R. B. Spielman, Rev. Sci. Instrum. **66**, 867 (1995).
25. J. P. Apruzese, K. G. Whitney, J. Davis, and P. C. Kepple, J. Quant. Spectrosc. Radiat. Transfer **57**, 41 (1997).
26. T. W. L. Sanford, R. C. Mock, R. B. Spielman, D. L. Peterson, D. Mosher, and N. F. Roderick, Phys. Plasmas **5**, 3737 (1998).
27. J. P. Apruzese, J. W. Thornhill, K. G. Whitney *et al.*, IEEE Trans. Plasma Sci. **26**, 1185 (1998).

28. K. L. Wong, P. Beiersdorfer, K. J. Reed, and D. A. Vogel, *Phys. Rev. A* **51**, 1214 (1995).
29. J. P. Apruzese, *J. Quant. Spectrosc. Radiat. Transfer* **25**, 419 (1981); *ibid.*, **34**, 447 (1985).
30. C. Deeney, T. J. Nash, M. R. Douglas *et al.*, *Bull. Am. Phys. Soc.* **42**, 1878 (1997).
31. J. W. Thornhill, K. G. Whitney, C. Deeney, and P. D. LePell, *Phys. Plasmas* **1**, 321 (1994).

TABLE I. Basic data from Al:Mg alloy wire shots on Z.

Shot	Wires	R(cm)	mg/cm	η	K yield (kJ)	K pulse (ns)	K power (TW)	Diam (mm)
71	180	1.5	3.6	2.8	68	20	2.6	1.8
70	236	2.0	2.1	5.5	122	13	7.2	1.8
72	264	2.5	1.3	8.2	152	13	8.4	2.5

**TABLE II. Line ratios: (), time resolved at peak power,
otherwise time integrated.**

Shot	Al: Ly α /He α	Al: Ly β /Ly α	Al: He β /He α	Mg: Ly α /He α	Mg α sum/Al α sum
71	2.24 (2.24)	0.13 (0.24)	0.22 (0.41)	1.24	0.28
70	2.33 (2.39)	0.17 (0.36)	0.26 (0.48)	1.34	0.31
72	2.42 (2.56)	0.21 (0.29)	0.29 (0.42)	2.08	0.21

FIGURE CAPTIONS

FIG. 1. Time and space integrated spectrum of shot 70, showing the α lines of both H- and He-like Mg and Al, plotted in arbitrary linear units.

FIG. 2. Spatially integrated Al K-shell spectrum of shot 70, time-resolved at peak K shell power, plotted in arbitrary linear units.

FIG. 3. Plots of (a) the temperature profile of shot 70's Z pinch at the peak of its K-shell power which replicates the radiation data as described in Sec. C, and (b) the corresponding Al ion density profile.

FIG. 4. Plots of (a) the Al K-shell spectrum calculated to be emitted from the core only of the best-fit profile for shot 70, and (b) the theoretical spectrum emitted from the full profile, core plus blanket.

FIG. 5. Comparison of measured absolute power at the peak of shot 70's K-shell power with that of the best-fit profile calculation which fits the rest of the radiation data. The absolute power was measured using photoconductive detectors (PCD's) for which 50% of the response occurs within the photon energy band indicated by the respective horizontal bars.

FIG. 6. The fraction of the load mass for the best-fit profile of shot 70 which lies above a given electron temperature.

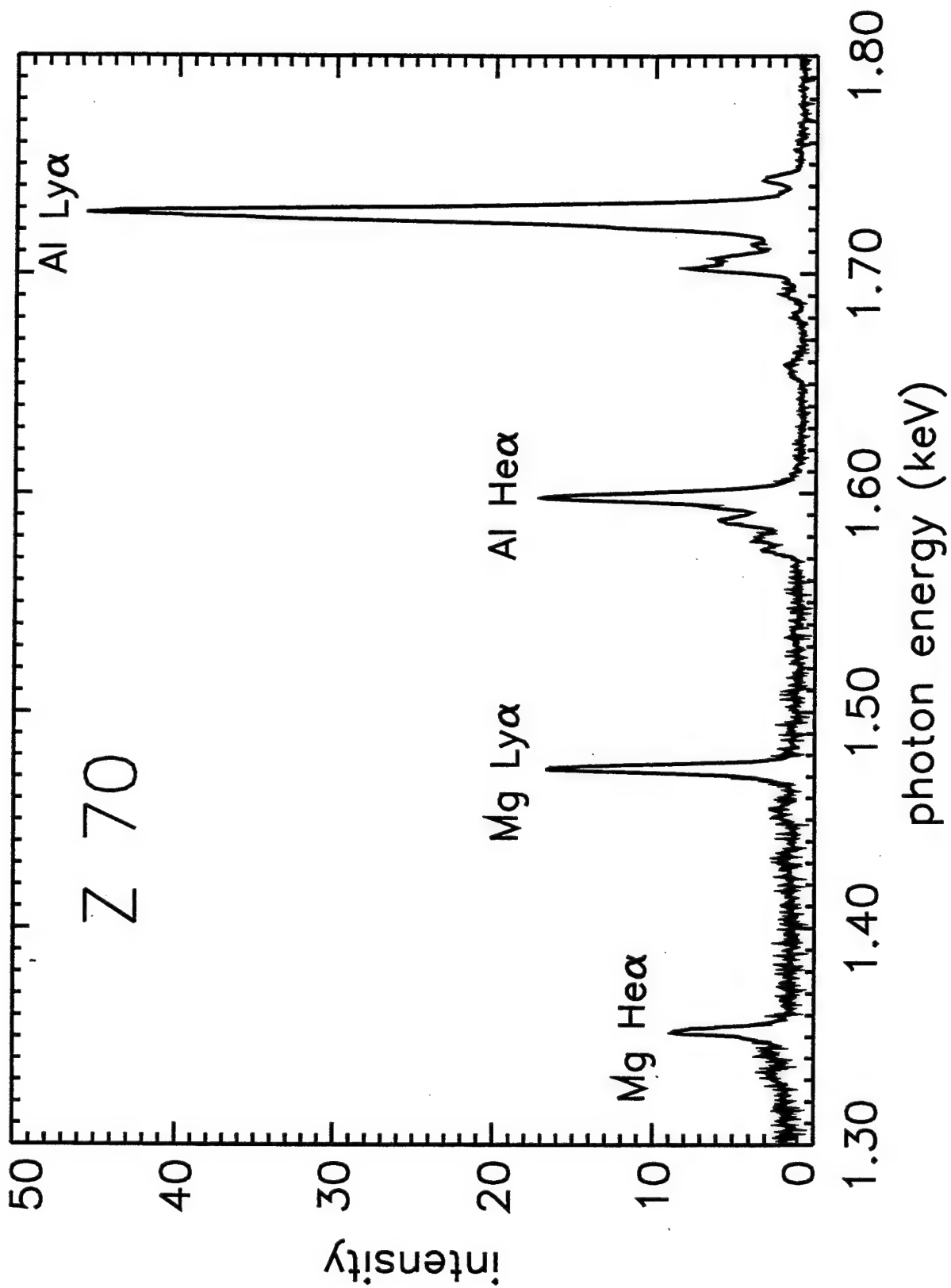


FIG. 1

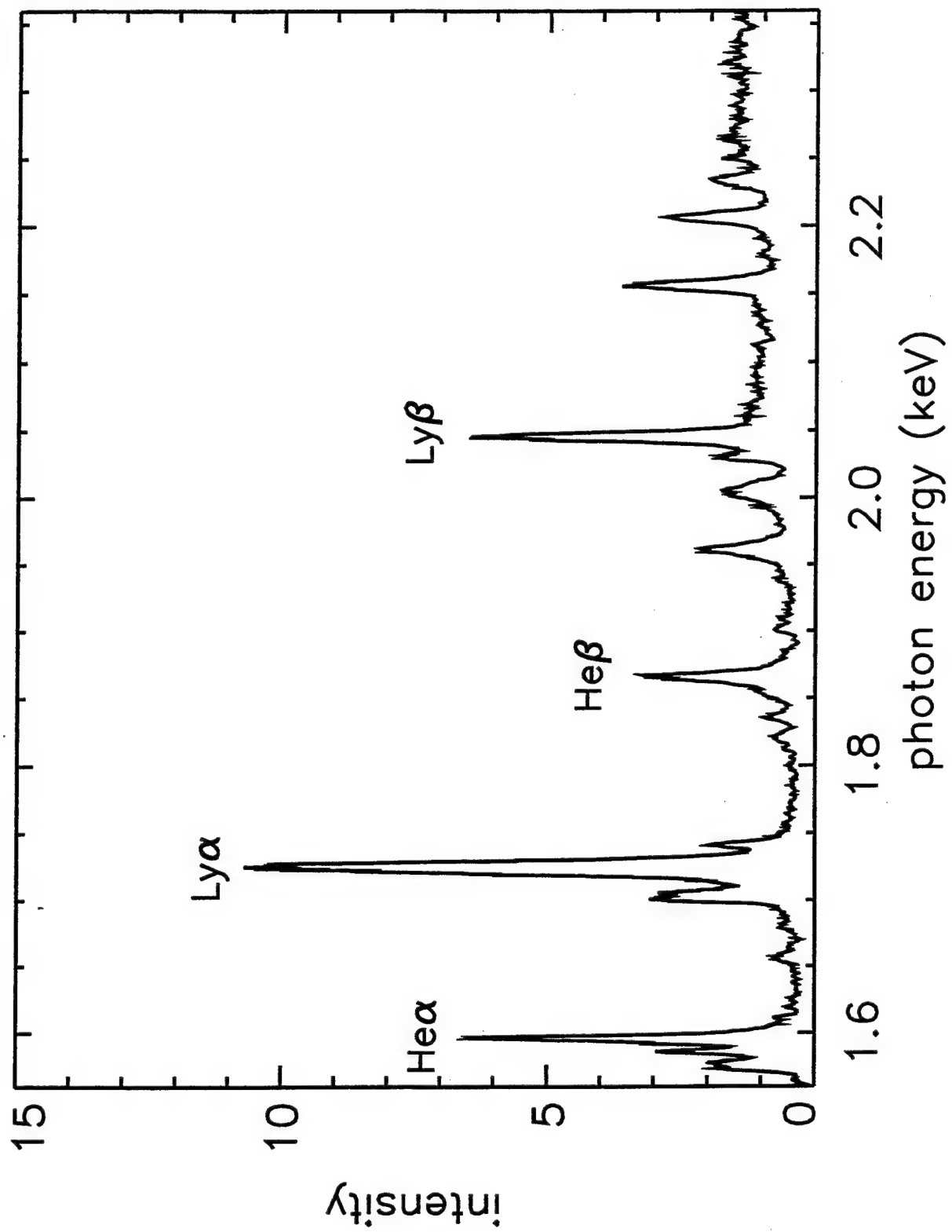


FIG. 2

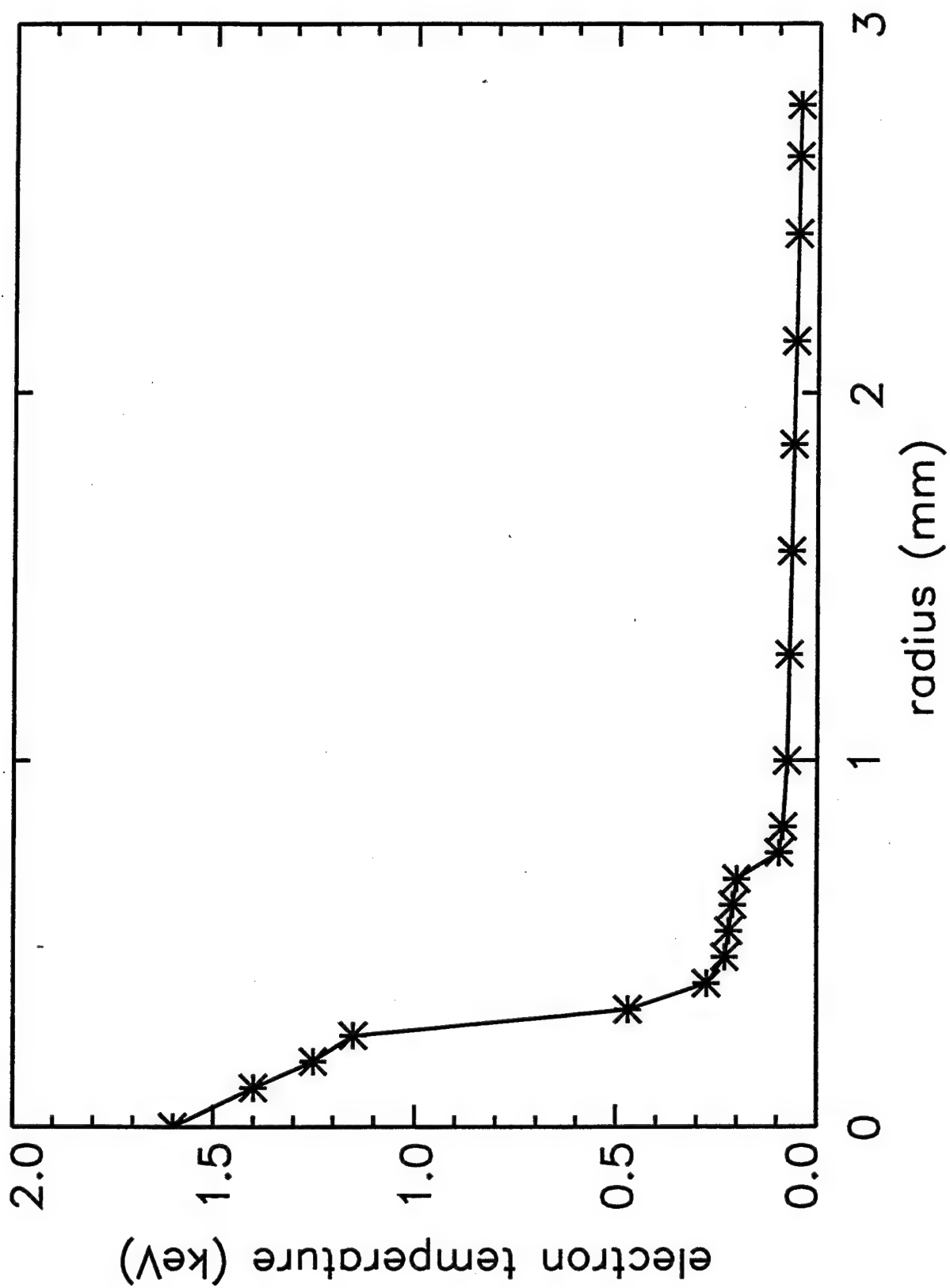


FIG. 3a

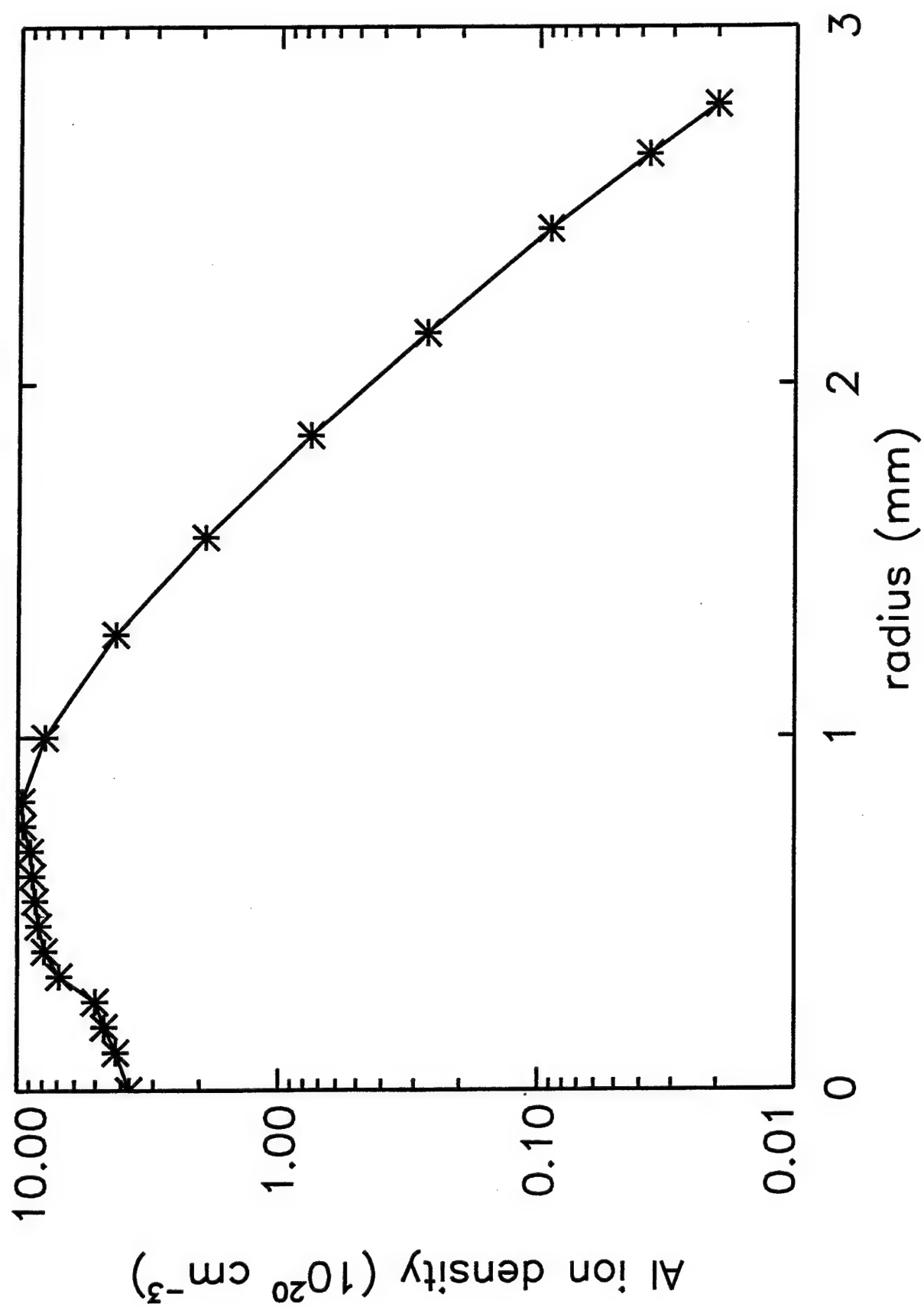


FIG-3b

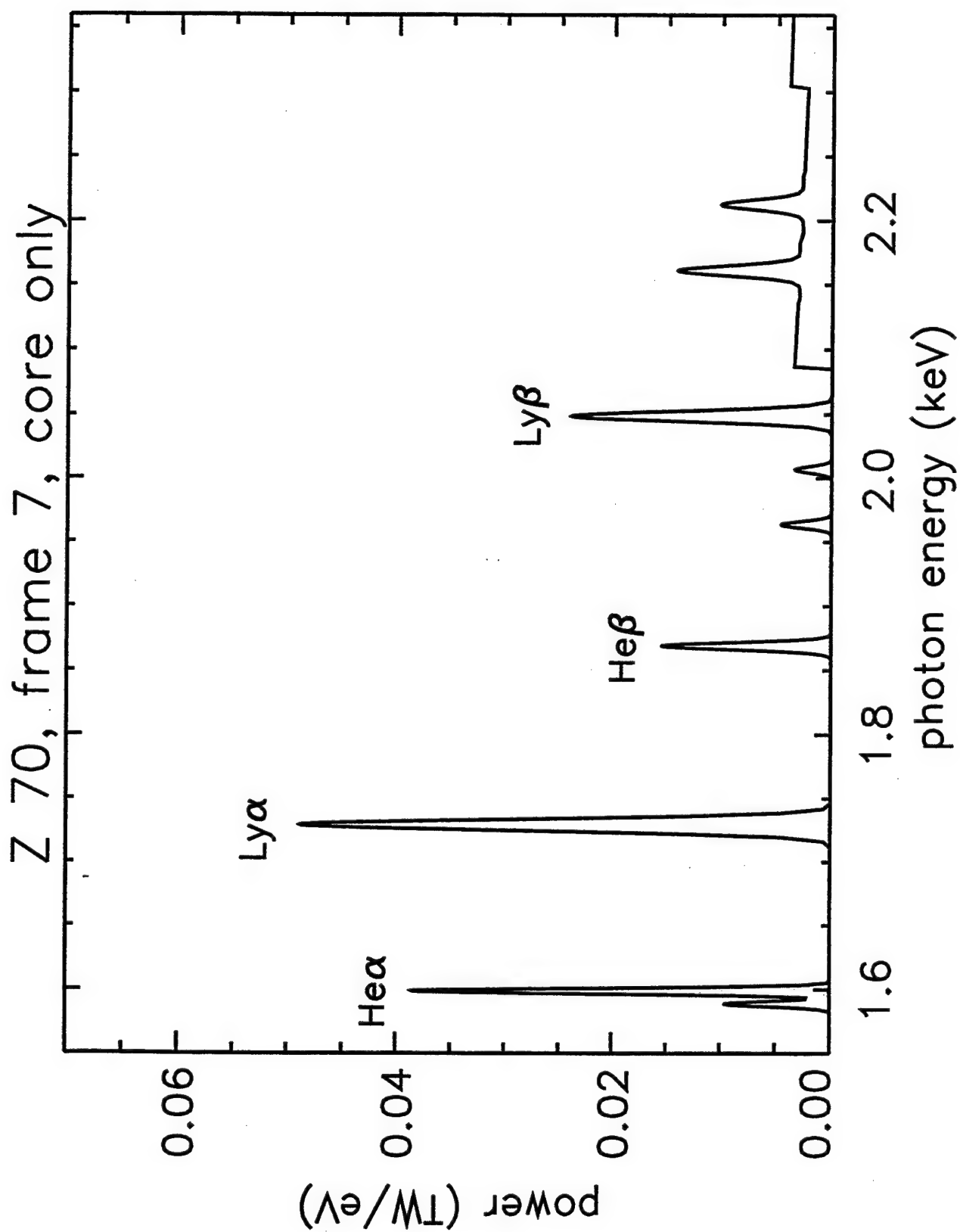


FIG. 4a

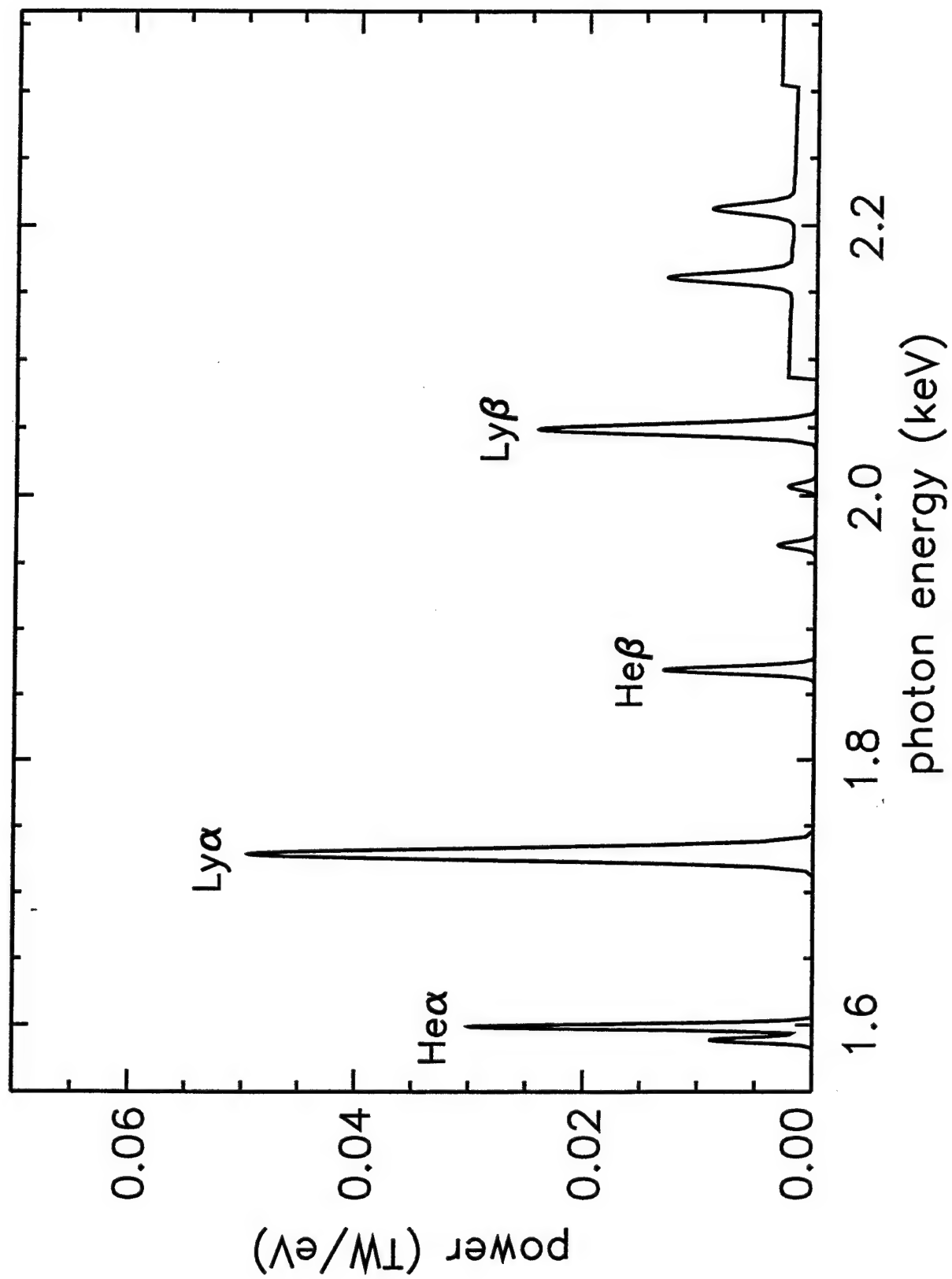


FIG. 4b

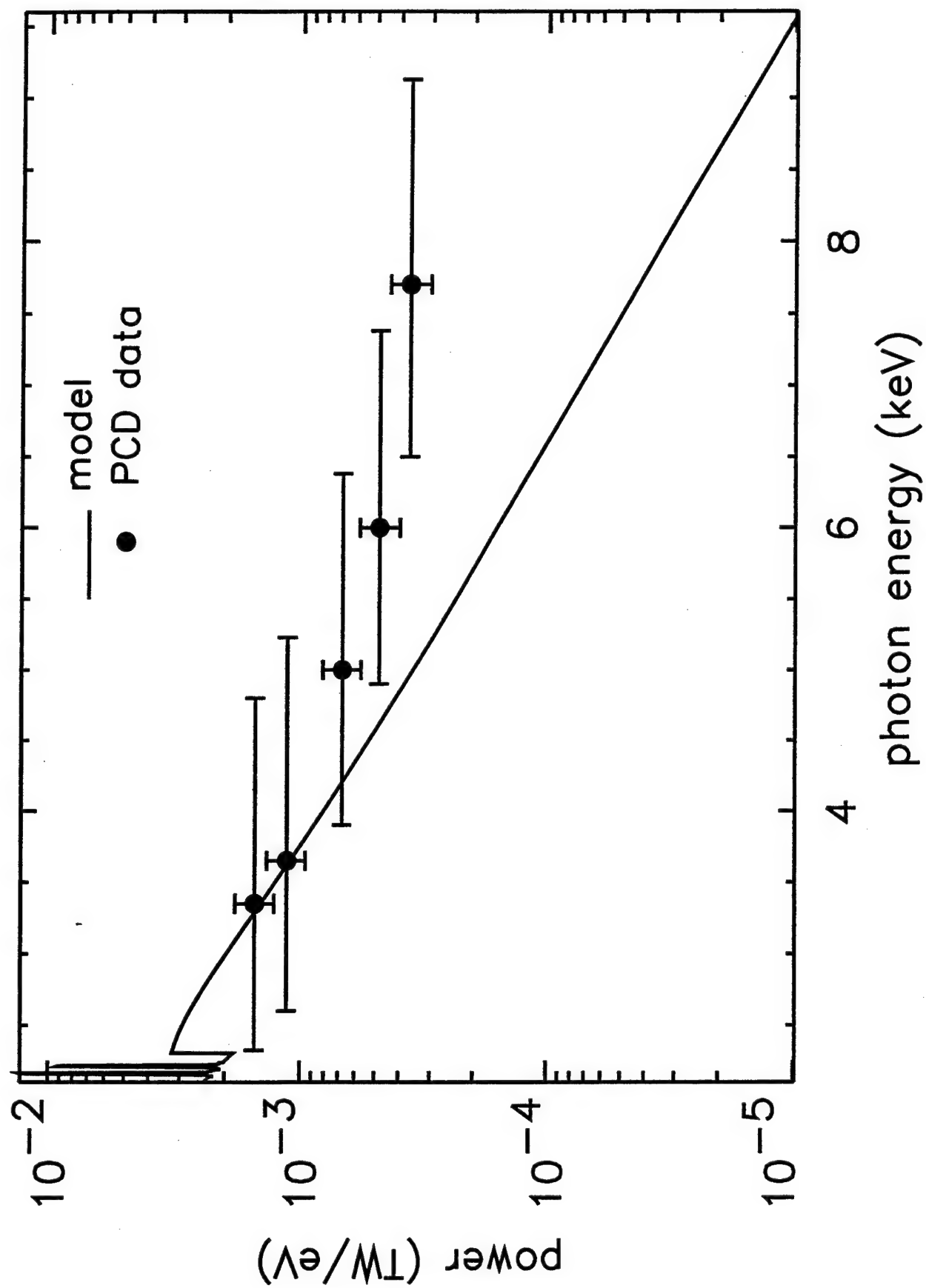


FIG. 5

Z 70, frame 7

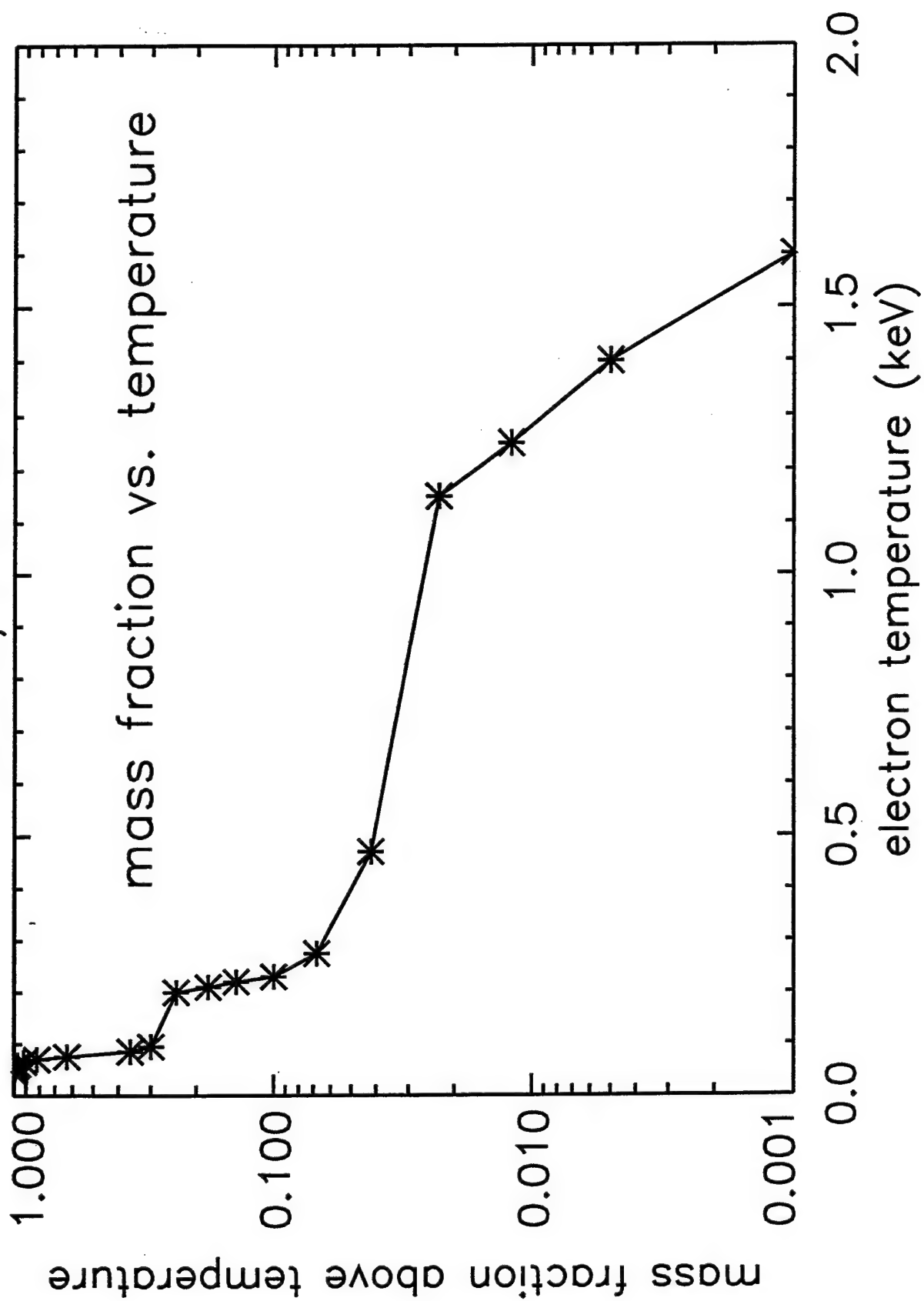


FIG. 6

III. Plasma Spectroscopy of Pulsed Power Driven Z-pinch Titanium Plasmas

ABSTRACT

We have investigated the radiative behavior of a titanium wire load driven on the Sandia National Laboratory Z facility. A radiation hydrodynamic model self-consistently driven by a circuit describes the evolution of the plasma and its self-generated environment. Numerical simulations were carried out to compare the K- and L-shell soft x-ray emission as a function of the ionization dynamic model. The ionization models compared include (1) a time-dependent non-equilibrium (NEQ) model, (2) a Collisional Radiative Equilibrium (CRE) model, and (3) a Local Thermodynamic Equilibrium (LTE) model. For all three cases, the radiation transport is treated (a) in the free-streaming optically thin approximation, where the plasma is treated as a volume emitter, and (b) in the optically thick regime, where the opacity for the lines and continuum is self-consistently calculated on-line and transported through the plasma. Each of the resulting six simulations is carried out independently to determine the sensitivity of the implosion dynamics to the ionization and radiation transport model (i.e. how the ionization dynamic model affects the radiative yield and emission spectra). Results are presented for the total and K-shell radiation yields, and emission spectra as a function of photon energy.

1. INTRODUCTION

Z-pinch physics is enjoying a modern-day renaissance due, in part, to the successful demonstration of the Z-facility's radiative performance. The experimental results have thus far been spectacular, culminating in the production of about 290 TW of radiated power from a double-nested wire array initially investigated and theoretically studied by NRL¹. Total radiation yields of the order of a megajoule have been reported from tungsten, titanium and stainless steel wire array implosions²⁻⁴. Z-pinch loads that are imploded to generate large amounts of soft x-rays are referred to as Plasma Radiation Sources (PRS). The dynamic evolution of PRS often exhibits structure during the implosion indicative of growing plasma instabilities. One of the goals of the program is to minimize the formation of plasma structure and produce more nearly 1-D cylindrically symmetric implosions. Better stability means a tighter Z-pinch at the stagnation phase and a more uniform radiating plasma, resulting in higher radiative output, and, in particular, greater K-shell yield. This suggests the importance of designing experiments that are more 1-D like. Modeling two- and three-dimensional effects in Z-pinch plasmas should be viewed as a tool for designing loads that minimize instabilities and produce a uniformly radiating plasma.

The theoretical description and numerical simulation of pulsed power driven Z-pinch plasma loads is based on a variety of models that vary from the very simple (as in the case of the slug model), to very complex one-, two- and three-dimensional scenarios. The accuracy and reliability of a model is assessed by how well it provides a basis for an improved understanding of the observations as well as the capability to accurately predict the behavior of planned DTRA experiments. In some instances, the simple slug models, coupled to two level atom ionization dynamic models, have been employed to crudely estimate the implosion time and the magnitude of the emitted K-shell x-ray pulse. At the other extreme there are one-, two- and three-dimensional Radiation Magnetohydrodynamic (RMHD) scenarios that incorporate a portfolio of subroutines for the equation of state, non-LTE ionization physics, transport properties, etc. These models attempt to describe the dynamic evolution of the plasma, including growth of plasma instabilities and how they affect the integrity of the implosion and the emitted x-ray pulse.

Model validation should be determined by comparing theoretically generated databases with experimentally observed results for as many plasma parameters as possible. The parameters most commonly selected include the magnitude of the radiative yield, the x-ray pulse length and shape, x-ray pinhole photographs of the assembling plasma, and emission spectra. The

temperature and density are inferred from unfolding the experimental results in conjunction with an ionization dynamic model. In order to explore the sensitivity of the emission spectrum to variations in the model, we have performed a series of numerical simulations of a titanium wire array driven by the Z accelerator. The simulations were performed using a 1-D RMHD model to quantify how the emission features and radiation signatures are influenced as the atomic and opacity models are modified. The use of a full 1-D model is sufficient to illustrate the sensitivity of the emission history to the choice of atomic and opacity models. For example, in the case of multiple wire Ti array loads (having 40 or more individual wires) investigated on the SNL Saturn accelerator, the implosion appeared to be less influenced by azimuthal asymmetries and, to first order, adequately represented by a 1-D implosion model⁵⁻⁷. Also, comparing and contrasting the synthetically generated spectra with the experimentally observed spectrum has the potential to validate the reliability of the simulation and identify the model strengths and weaknesses.

2. MODEL

The morphology of Z-pinch plasmas generally exhibits three (and in some cases four) distinct and sometimes overlapping stages. The first stage is the initial heating and expansion phase. In the second phase, $J \times B$ forces drive the implosion. The third stage is characterized by the reassembling of the plasma on axis, and the conversion of the kinetic energy of implosion to thermal energy. During this stage, the newly formed hot dense plasma emits an intense kilovolt x-ray pulse. Occasionally, a fourth and final stage may develop when the current is large enough to maintain plasma confinement, and additional heating and compression occurs, accompanied by additional x-ray production. The numerical simulations presented here to characterize the dynamics of a radially imploding Z-pinch plasma are based on a one-dimensional two-temperature multi-zone non-LTE radiation-magnetohydrodynamic model, DZAPP, with a transmission line circuit model representing the driving generator. A thorough discussion of the model is presented in reference 8.

The titanium model contains all the ground states and a manifold of excited states distributed throughout the various ionization stages. Only the strongest lines, i.e., lines with the largest oscillator strengths, were included in the simulations. Thus, the simulations were carried out with an atomic model for titanium that contained over 300 spectral lines distributed throughout the K, L, and M shells. This assumption represents a reasonable compromise between the

atomic model and computational constraints, particularly when the medium is opaque and radiation must be transported through the plasma.

Radiation emission from the plasma and its opacity are dependent on the local atomic-level population densities. Except for optically thin plasmas, however, the level populations depend on the radiation field, since optical pumping via photoionization and photoexcitation can produce significant population redistribution. Thus, the ionization and radiation transport processes are strongly coupled and must be solved self-consistently. In this model, an iterative procedure³ is used, where level populations are calculated using the radiation field from the previous iteration, then using these populations to calculate a new radiation field until convergence is reached.

Radiation emission, including opacity effects, from the plasma is dependent upon the local atomic level populations, because photons are created by radiative recombination and spontaneous decay, and the absorption of these photons can lead to population redistribution. Thus, the ionization dynamics and radiation transport are a strongly coupled interactive system, and must be solved together as demonstrated in reference 9. The radiation transport of the bound-bound and free-bound transitions was carried out using the probability of escape formalism described by Apruzese¹⁰. Multifrequency transport is performed for the free-free radiation.

3. RESULTS

The current profile that results from driving the circuit with a changing load inductance is shown in Fig. 1. The peak short-circuit current is about 20 megamperes. The load in this case is represented by a multiwire array of titanium with a total mass of 324 μg , a length of 2 cm and an initial array radius of 2 cm.

A compact summary of the evolution of selected hydrodynamic parameters from the DZAPP model is given in Fig. 2 as a function of radius $[(x) \text{ in cm}]$ and time $[\text{in } \mu\text{sec}]$ with a time-dependent collisional-radiative ionization dynamic model (referred to as NEQ). The electron and ion temperatures are represented as E-Temp and I-Temp, respectively, and are in eV. The plasma density is given in g/cm^3 and the radiative cooling rate in kW/cm^3 . The scale at the right of each insert on the Fig. associates a numerical (logarithmic) value with each contour (color). The "first" bounce occurs around 140 ns. At peak compression, the ion temperature is about 100 keV and the electron temperature reaches about 20 keV in a highly localized region.

The ionization dynamic models used here to produce emission spectra are designated NEQ, CRE and LTE for both optically thick and thin radiation transport. Each of the resulting

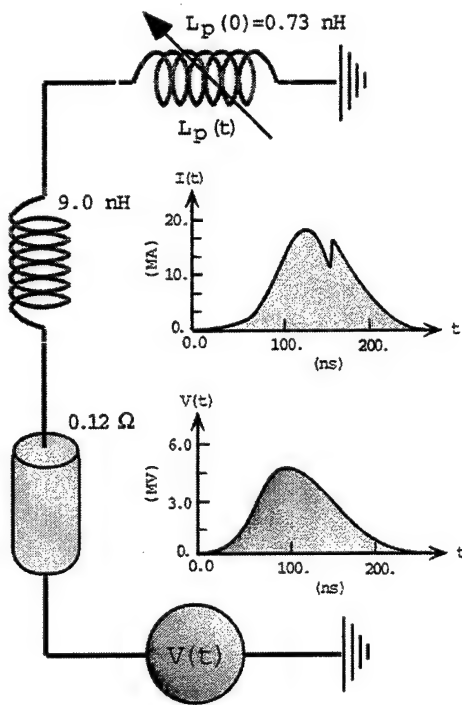


Figure 1. Equivalent electrical circuit.

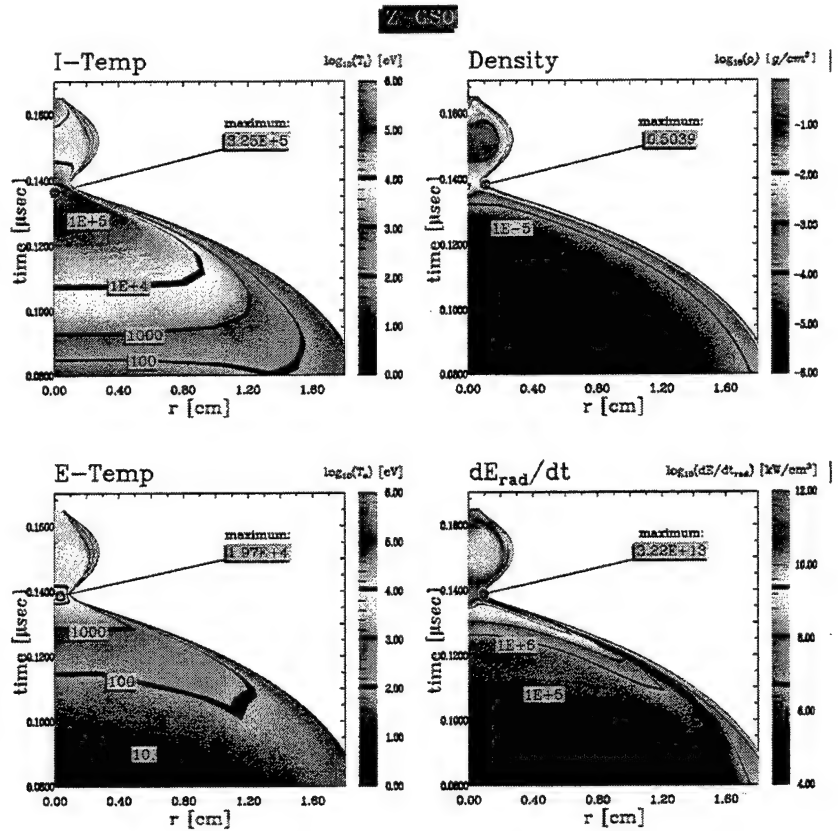


Figure 2. Time dependent Collisional Radiative (NEQ) model results for the ion and electron temperatures, mass density, and radiative cooling as functions of radius (cm) and time (μsec).

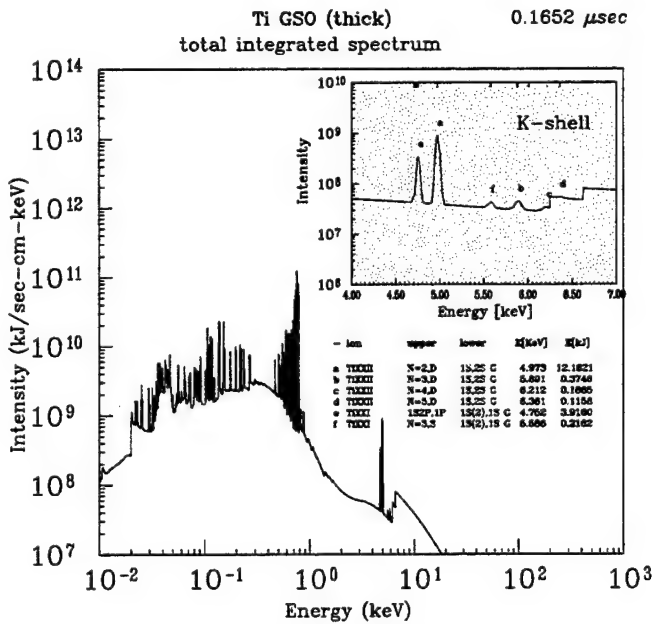


Figure 3. Emission spectra for the time dependent NEQ model.

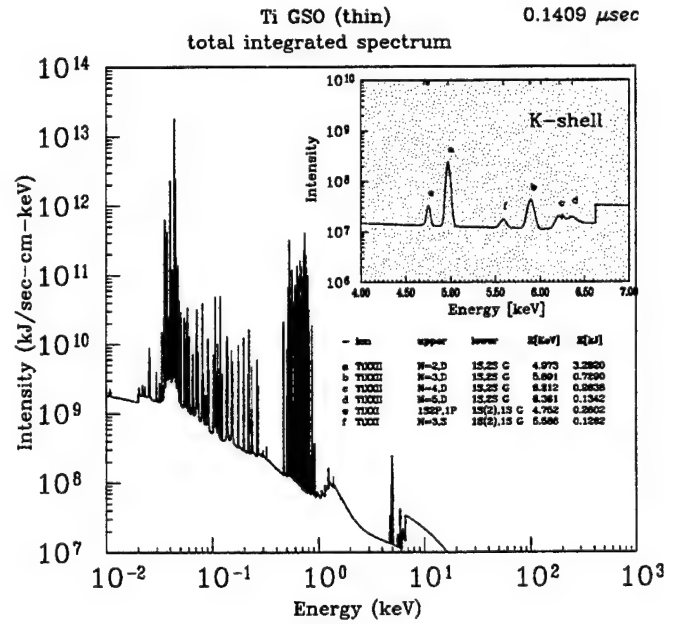


Figure 4. Emission spectra for the optically thin NEQ model.

six simulations is self-contained in the sense that for each ionization/transport model, a full RMHD simulation was performed (rather than the post-processing of a single hydrodynamic simulation). This produced small differences in the implosion times and minimum radii. All of the simulations were carried out until the plasma, on reexpansion, reached a radius corresponding to 2.5 times the minimum implosion radius. The total time-integrated spectra produced from the NEQ model will serve as our benchmark, and is shown in Fig. 3. Some selected spectral lines are identified along with their transition energies (keV), radiated powers (MW/cm) and radiated energies (kJ). The hydrogen- and helium-like resonance lines account for about 15% of the radiated K-shell energy. The calculated total and K-shell radiated energies are presented in Table 1.

TABLE 1: Radiative Yields

Ionization Model	Rad Transport	Total Yield (kJ)	K-shell Yield (kJ)
NEQ	thick	980	131.5
CRE	thick	989	128.2
LTE	thick	599	163.7
NEQ	thin	701	47.8
CRE	thin	678	50.2
LTE	thin	456	239.9

The optically thin simulations are given for comparison, since the thin approximation is often employed erroneously as a means of radiatively cooling the plasma. As the plasma evolves, the opacity (which is a function of plasma density and temperature, pathlength, and oscillator strength) can potentially influence the population of excited states, and consequently the emitted radiation. A comparison of the Total and K-shell thick radiative yields shows that the CRE simulation is in close agreement with the NEQ calculation. Table 1 also illustrates that the LTE assumption, even with opacity, predicts a Total yield reduced by more than 50% and a K-shell yield higher by about a factor of two than the NEQ model. As the density increases during peak compression, the NEQ and CRE L-shell excited state populations should exhibit trends towards LTE. However, the temperature remains too high and the density too low for the entire plasma to go into LTE. The experimental observations for the 110 multiple wire load (shot Z88) produced a total yield of about 1 MJ and a K-shell yield of about 125 kJ. The NEQ and CRE predictions of total and K-shell yield are in reasonably good agreement with the

observations. Just prior to the bounce, the plasma showed signs of developing perturbations reminiscent of the spike and bubble structure which is the trademark of the Rayleigh-Taylor instability. We can speculate that, as the structure evolves, it seeds "bright spots", and it is these spots that are the origin of energetic photons lying above the K-shell.

The total emission spectra are shown on Figs. 3-8 for the cases represented in Table 1. Figure 3 is the NEQ result, and is considered the benchmark spectrum for these comparisons. The corresponding CRE spectrum, in Fig. 5, is nearly identical. This result is consistent with Table 1. The energies in the individual K-shell lines, given in the tables within the figures, also agree to within a few percent. The Ly- α lines, for example, are calculated to radiate 12.16 kJ for the NEQ case and 11.74 kJ for the CRE case, a difference of about 3.6%. The other K- and L-shell lines exhibit similar agreement. We must conclude that, at least in the regions emitting the most radiation, the plasma ionization (and excitation) state remains close to collisional radiative equilibrium. This is not a universal result; in many simulations with other masses and load constituents, substantial departures from CRE are obtained. For the optically thin NEQ and CRE emission spectra (Figs. 4 and 6, respectively), a similar conclusion can be drawn: they are nearly the same, with the energies in individual lines differing by about 10%. For example, the Ly- α lines differ by 11.2%.

Turning our attention to Figs. 7 and 8, it is obvious that the NEQ and CRE results are substantially different from the corresponding LTE emission spectra. Differences of a factor of five between individual lines are common. For example, the optically thick LTE to NEQ Ly- α line ratio is $(51.20\text{ kJ}/12.16\text{ kJ}) = 4.21$! For the optically thin cases, the differences are even more pronounced. The implication is that the plasma is far from LTE in the regions where the bulk of the K- and L-shell radiation is produced. It is, nevertheless, to be expected that in cooler, denser regions (for example, at early times near the individual wires), the plasma will be close to LTE. However, little plasma radiation is produced in these locations.

One way to quantify the departure of the plasma from LTE during the various phases of the implosion is to follow the departure coefficients for selected atomic states. The departure coefficient is defined as the ratio of the population of a given state to the population it would have if the plasma were in LTE at that time and place. As we have surmised from the emission spectra, for much of its history, the plasma is far from LTE. In the region of peak radiated power, which occurs at $r \simeq 0.10$ cm and $t \simeq 140$ ns, only the $n \geq 2$ levels of hydrogenlike titanium are in LTE. All the other levels are generally far removed from LTE. This has major consequences for models assuming radiation diffusion with a blackbody source function or Rosseland weighted opacities in conjunction with Eddington transport equations both for the

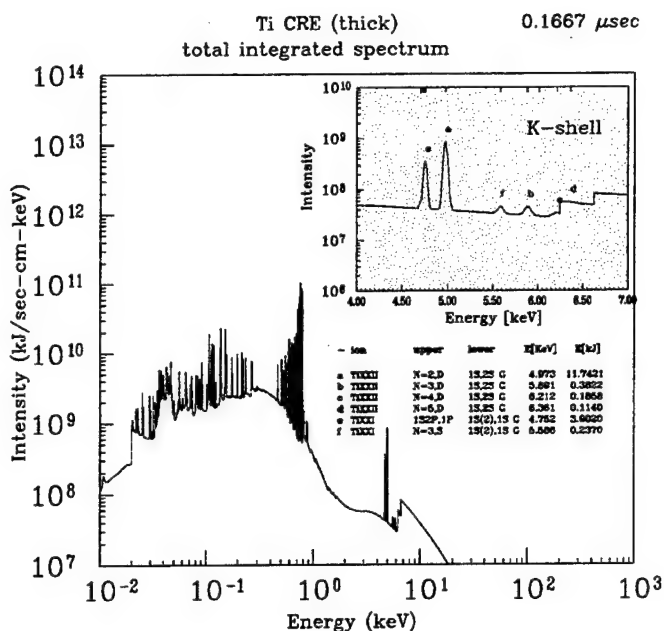


Figure 5. Emission spectra for the CRE model.

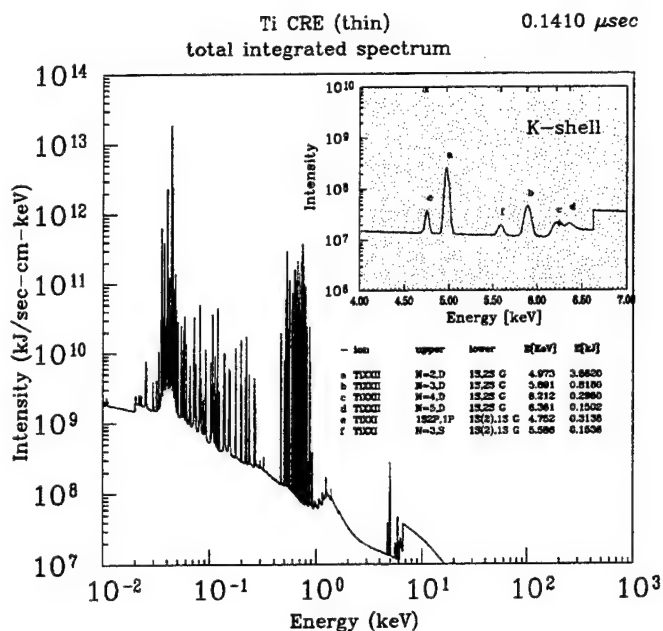


Figure 6. Emission spectra for the optically thin CRE model.

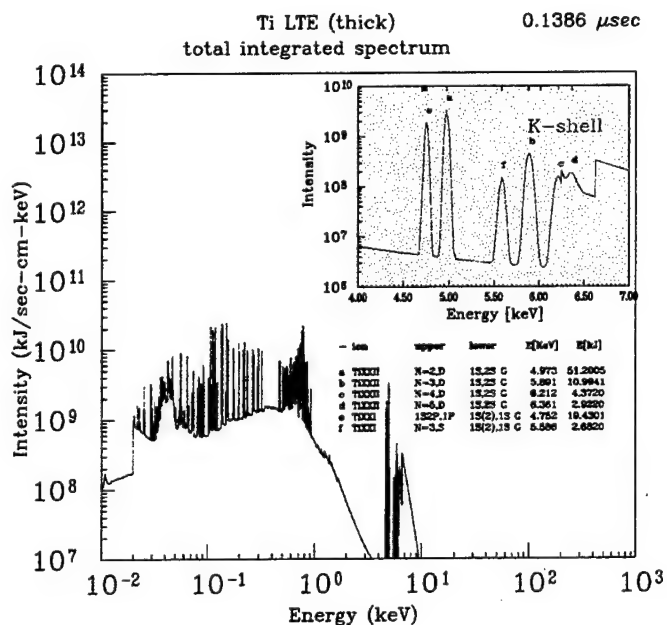


Figure 7. Emission spectra for the LTE model.

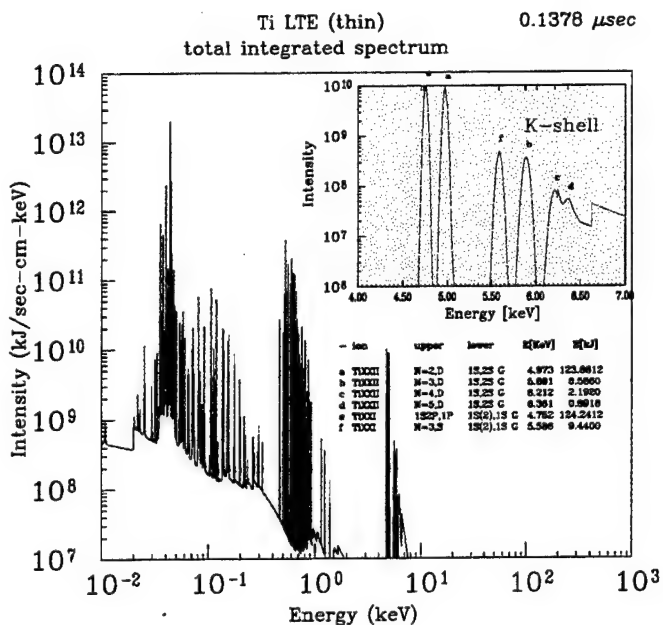


Figure 8. Emission spectra for the optically thin LTE model.

evolving dynamics as well as the emission spectra. Usually, any agreement between numerical simulations based on these models and experiment is purely fortuitous unless, of course, the plasma is a blackbody radiator in LTE.

A detailed summary of the departure coefficient history for selected atomic levels in H-, He-, Li-, and Be-like titanium is given in Figure 9. The coefficient history near peak implosion ($t = 141 - 145 ns$) and ($r = 0 - 0.22 cm$) is shown. In each case, the value of the departure coefficient at the *time and location of peak radiative emission* is indicated. The atomic levels shown are: (1) the $1s, 2S$ H-like, (2) the $1s^2, 1S$ He-like, (3) the $1s^2 2s^1, 2S$ Li-like, and (4) the $1s^2 2s^2, 1S$ Be-like states. Even at the point of peak emission, the coefficients are substantially different from unity, indicating a correspondingly large departure from LTE. The coefficients for the indicated H-, He-, Li-, and Be-like levels are, respectively: 18.0, 0.053, 0.21, and 2.62 at peak emission. The contour corresponding to $f/f_{LTE} = 1$ is highlighted in black for reference. Note that the gradients of the coefficients are very large near the point of peak emission. The departure coefficients deviate drastically from unity away from this region. The conclusion which must be drawn is that the plasma atomic populations and radiative emission are, in general, strongly non-LTE.

Z88-Ti

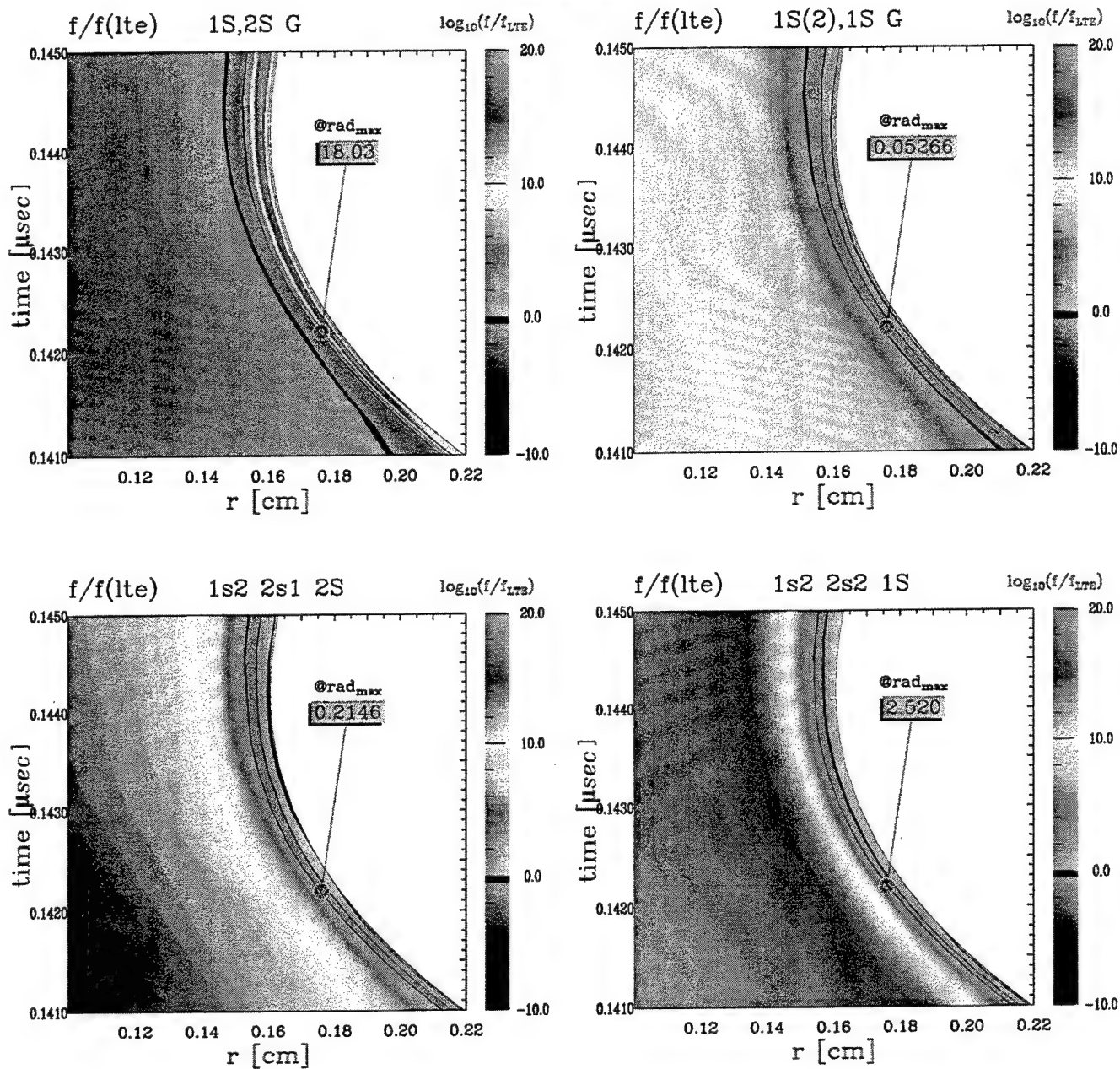


Figure 9. Departure coefficients, (f/f_{LTE}) for selected atomic levels in H-like through Be-like titanium.

4. CONCLUSIONS

The intent of this investigation was (1) to generate and characterize the emission spectra from an imploding multiwire Ti array plasma driven by the 20 MA Z accelerator, (2) compare and contrast synthetically generated spectra for three different (but standard) models for the ionization dynamics, and (3) use the synthetic spectra as a tool for validating the accuracy and reliability of the numerical simulation model. These issues have been addressed, and we have concluded that the synthetically generated spectra can be used to benchmark and validate numerical simulations. The key to benchmarking and validating models depends upon obtaining reliable and reproducible experimental measurements.

ACKNOWLEDGMENTS

The authors would like to thank Dr. John Rogerson for assisting in generating the numerical results and Drs. Apruzese, Terry and Whitney for many helpful discussions and for making available the results of their analysis of multiple wire experiments.

REFERENCES

1. J. Davis, et al., *Appl. Phys. Lett.* **70**, 170 (1997).
2. C. Deeney, T. Nash, et al., *Phys. Rev. E* **56**, 5945 (1998).
3. C. Deeney, T. Nash, et al., *Phys. Plasmas* **5**, 1 (1998).
4. R. Spielman, C. Deeney, et al., *Phys. Plasmas* **4**, 1519 (1997).
5. T. Sanford, G. O. Allshouse, et al., *Phys. Rev. Lett.* **77**, 5063 (1996).
6. K. Whitney, W. J Thornhill, et al., *Phys. Rev. E* **56**, 1 (1997).
7. T. Sanford, T. Nash, et al., *Rev. Sci. Instrum.* **68**, 852 (1997).
8. J. Davis, J. Giuliani, Jr., M. Mulbrandon, *Phys. Plasmas* **2**, 1766 (1995).
9. D. Duston, R. Clark, J. Davis, J. Apruzese, *Phys. Rev. A* **27**, 1441 (1983).
10. J. Apruzese, *J. Quant. Spect. and Rad. Transfer* **25**, 419 (1981).

IV. DECADE QUAD LOAD PERFORMANCE ASSESSMENT

A. Introduction

A long current rise time makes it essential that DECADE QUAD have the ability to efficiently extract K-shell emission from large radius loads. In this section we evaluate the future performance on DECADE QUAD of the large radius loads that have been developed for Double Eagle and Saturn. These are evolutionary loads in that the knowledge attained from their usage on Double Eagle and Saturn will allow us to mitigate the risks associated with large radius implosions and ultimately design loads that make DECADE QUAD a successful argon Plasma Radiation Source (PRS) machine. In particular, the 7 cm diameter uniform fill loads used in the Double Eagle and Saturn long pulse argon experiments will be assessed in terms of their future performance on DECADE QUAD.

B. I^2 scaling of Double Eagle yields to DECADE QUAD

Figure 1 displays argon K-shell yield as a function of increasing mass-per-unit length for three theoretical curves at a fixed coupled energy-per-ion ($\eta^* = 4$). The first curve was obtained using a 1D radiation transport model that used classical transport coefficients in accord with some of our earliest work on K-shell yield scaling.^{1,2} The second curve was obtained using the same 1D model with the exception that the transport coefficients were enhanced in order to match the stagnation conditions attained in a series of Double Eagle short pulse small radius aluminum experiments.^{3,4} The third curve is very hypothetical in the sense that it is what one might obtain if one tried to match the 1D transport coefficients to the stagnation conditions attained from a series of poorly designed experiments. All three of these curves as well as many K-shell scaling experiments exhibit the characteristic I^4 to I^2 K-shell yield transition as a function of increasing mass load. The I^4 scaling regime is characterized by radiative cooling rates that are too small to effectively influence the dynamics of the pinch. Under these low mass conditions the K-shell radiation increases at the optically thin rate, which scales as the square of the ion density (N_i^2) or as $mass^2$. However at sufficiently large mass the rates will begin to affect the pinch dynamics and the radiative yields will

be limited by energy conservation to less than or equal to an I^2 increase with mass.

Depending on the curve and mass load there can be a large range of K-shell yields spanned by the curves in Fig. 1. This is the major difficulty with using curves like these, or 0-D models based on them, to predict K-shell yield because it is not known *a priori* which curve is applicable to a given experiment. This difficulty is especially true for the larger radius experiments because they are at the frontier of new load design, where the roles that asymmetry, instability, compression, and adequate current play in influencing K-shell yield are largely unresolved. Therefore in the interest of eliminating as many model dependences as possible it was decided that it would be best to scale the experimental Double Eagle long pulse argon K-shell yields directly to DECADE QUAD using only an I^2 (energy) scaling. This eliminates the need for detailed knowledge of where the I^4 transition begins and ends at the sacrifice of making a conservative projection of the DECADE QUAD K-shell yield. Fig. 2 illustrates the procedure of I^2 scaling by projecting a fictitious Double Eagle K-shell yield to DECADE QUAD.

The major caveat in performing an I^2 projection of Double Eagle yields to DECADE QUAD is the assumption that loads using the same nozzle and that couple the same energy-per-ion to the load behave similarly on Double Eagle as DECADE QUAD. Because there are large uncertainties in knowledge of gas puff initial mass distributions as well as their total mass, it is difficult to know with certainty the coupled energy-per-ion. However, if accurate circuit models of Double Eagle and DECADE QUAD are available then the relative energy differences between the two machines can be assessed. Knowledge of this relative difference is all that is necessary for a valid I^2 projection. In this regard, the model conditions that are used to calculate the coupled energy as a function of mass load must be applied uniformly to both Double Eagle and Decade Quad snowplow models. For example, if a 1/10 compression and uniform fill distribution are assumed for Double Eagle they must also be assumed for DECADE QUAD. On the other hand the Double Eagle and DECADE QUAD models could both assume a 1/20 compression and a non-uniform initial mass distribution and it would not affect the results of the I^2 scaling projection. In this work a 1/10 compression and uniform fill distribution are modeled.

The Water Convolute design is the circuit model used to model DECADE QUAD.⁵ This

design is shown in equivalent circuit form in Fig. 3 along with a current profile that is calculated from imploding a 7 cm diameter, uniform fill, 400 $\mu g/cm$ load. Fig. 4 displays the Double Eagle equivalent circuit model that gave the best overall representation of all the recent argon gas puff experiments that were performed on Double Eagle in the fall of 1998. The biggest difference between this model and those used in the past is the equivalent circuit inductance is increased to 28 nh from a previous value of 20 nh. Insufficient inductance is likely the reason there were difficulties matching calculated and measured implosion times and peak currents from past gas puff experiments. The Double Eagle open circuit voltage profiles for the long pulse and short pulse modes were provided by John Riordan and Jerrold Levine of Maxwell/PI. The open circuit voltage profile that was used to model long pulse experiments for which the Marx bank was charged to 65 kV is nearly the same as that for the 60 kV charge except it is enhanced by the factor 65/60. The load length was 4 cm for all the Double Eagle gas puff experiments and the current return diameter was 4 cm for the short pulse shots and it was 12 cm for the long pulse shots.

Figures 5-8 illustrate that the Double Eagle circuit model does an excellent job of reproducing the experimental current trace from representative shots for all four argon gas puff experimental configurations that were utilized during the fall 1998 campaign: short pulse - 2.5 cm diameter shell (Fig. 5; shot 4041), long pulse - 7 cm diameter uniform fill (Fig. 7; shot 4059), long pulse (enhanced voltage) - 7 cm diameter uniform fill (Fig. 6; shot 4083) and long pulse - 5 cm diameter shell (Fig. 8; shot 4071). In all four cases the circuit models reproduced the shape, the peak current, and the implosion time as determined from the experimental current trace (obtained from Maxwell/PI).

In order to calculate the current profiles in Figures 5-8 assumptions about the initial mass and mass distribution were made. For example, Fig. 7 shows the current profile and implosion time calculated for a 7 cm diameter uniform fill load of 190 $\mu g/cm$ that is representative of the long pulse enhanced voltage shot 4083. If instead, shot 4083 is modeled as a 6 cm diameter uniform fill load of 260 $\mu g/cm$ then the same current profile, the same peak current, the same implosion time as shown in Fig. 7 for the 7 cm diameter load are still obtained. In addition the calculated energy coupling to the load, which is indicated by the effective current I_{eff} shown in Fig. 9, is also the same. I_{eff} is defined as the peak current achieved from a linearly ramped current profile that

couples the same energy into a slug model load (10:1 compression) as does the snowplow model driven by the equivalent circuit model. This term represents a current normalization on the coupled energy, it is given by $I_{eff} = (\text{coupled energy} / 1.81 \times 10^3)^{1/2}$. Where I_{eff} is in MA and coupled energy is in Joules/cm. For most of the loads examined in this work I_{eff} is nearly identical to the peak value of the current I_{peak} .

Fig. 10 further illustrates the insensitivity of the Double Eagle current profile to the radius of the initial uniform fill mass distribution. In this figure I_{eff} is plotted as a function of Double Eagle implosion time for three different uniform fill gas distributions (3.5 cm, 3.0 cm, and 2.0 cm initial radius). The mass load that is required to give a specific implosion time for each of the gas distributions is also displayed. It is apparent from Fig. 10 that there exists a near one-to-one correspondence between implosion time and I_{eff} . Thus, in general, as long as the radii of the initial gas distributions are not grossly different, loads that have the same implosion time will produce approximately the same current trace ($I_{eff} \approx I_{peak}$) and energy coupling. Although our knowledge of the initial mass and its distribution in the experimental load is uncertain, this correspondence between energy coupling and implosion time give us confidence that we have a good model of the Double Eagle circuit. An example of the axial non-uniformity and uncertainty in the initial mass and distribution of an ostensibly 7 cm diameter uniform fill argon load is shown in Fig. 11 (as measured by and obtained from B. Weber, NRL code 6770). It is apparent from this figure that it is probably more appropriate to model the experimental load as a 6 cm diameter rather than a 7 cm diameter uniform fill.

The Double Eagle energy coupled to the load as well as the ratio of the DECADE QUAD to the Double Eagle coupled load energy are displayed in Fig. 12 as a function of the implosion time for a modeled 7 cm diameter uniform fill load. This figure shows that DECADE QUAD couples only 1.4 times the energy of Double Eagle into an $\eta^* = 4$ load, whereas it couples 3.7 times the energy of Double Eagle into an $\eta^* = 1$ load. Because the low η^* loads have longer implosion times it is not surprising that DECADE QUAD couples substantially more energy to them than to the higher η^* loads.

The Double Eagle K-shell yields are projected to DECADE QUAD in a straightforward

manner by the use of the DQ/DE energy coupling curve of Fig. 12. The DECADE QUAD yield is projected from Double Eagle shot 4083 by multiplying the Double Eagle yield of 15.3 kJ by two factors. The first is an occlusion factor of 1.13 and the second is the ratio DQ/DE, which is 2.5 for the 188 ns implosion time of shot 4083. The result is that the 15.3 kJ Double Eagle K-shell yield energy scales ($I_{effective}^2$ scales) to 43 kJ on DECADE QUAD. This procedure is performed for the rest of the 7 cm diameter enhanced voltage shots and the results are displayed in Fig. 13. In this figure the experimental Double Eagle K-shell yields are plotted as a function of their implosion time. It is apparent from the equivalent DECADE QUAD yield curves how each Double Eagle shot scales to DECADE QUAD. Notice, there are several K-shell yields that scale to 40 kJ. The drop off in Double Eagle K-shell yield for the longest implosion times is due to increasingly small η^* values (too little energy-per-ion to ignite the K-shell), while the fall in yield for the shorter implosion times is due to a decrease in load energy coupling, see Fig. 12. The decrease in Double Eagle K-shell yield relative to DECADE QUAD for the shorter implosion times is because the ratio of DQ/DE coupled energy falls significantly, again see Fig. 12.

If the Double Eagle experiments are modeled as 6 cm diameter uniform fill loads, which as mentioned above are more in accord with B. Weber's measurements than are the 7 cm diameter modeled loads, the same equivalent DECADE QUAD yield curves as shown in Fig. 13 are obtained. However there is one important distinction, and that is the $\eta^* = 1.5$ line is now moved to a shorter implosion time of 177 ns. This implies that the Double Eagle experiments that scale to 40 kJ on DECADE QUAD are in an even lower η^* scaling regime than indicated by Fig. 13. There is experimental evidence (aluminum wire array experiments on Saturn short pulse and Z)^{6,7} of decreasing or saturated K-shell yield production in this regime at large mass load, which is a concern because DECADE QUAD will be imploding substantially larger mass loads than Double Eagle. In addition, our theoretical work also showed this same saturation trend as is illustrated in Fig. 14 for titanium plasmas.⁸ It was determined theoretically that increased opacity and decreased radiating K-shell mass fraction are responsible for this saturation behavior.^{7,8}

The same scaling procedure is also applied to the other non-enhanced voltage 7 cm diameter experimental shots and the results are displayed in Fig. 15. These experimental results do not project to as large of K-shell yields on DECADE QUAD as did the enhanced voltage shots. Since

it is clear from Fig. 16 (obtained from J. Riordan) that the experiments are in an I^4 scaling regime, this is an expected result.

C. I^2 scaling of Saturn K-shell yields to DECADE QUAD

Saturn long pulse was tested in April-May 1998. In this test 3 cm long, 7 cm diameter, 11.4 cm diameter current return, uniform fill gas puff loads and a 2 cm long, 180 wire, 5 cm diameter current return, aluminum wire array load were investigated. Because these were preliminary experiments, the purpose of writing this section is mainly to establish a baseline for evaluating future Saturn long pulse experiments and not to draw any firm conclusions from a limited initial data set. The experiments were preliminary for the following reasons: they are the first long pulse experiments ever performed on Saturn, only five gas puff shots with adequate diagnostics were taken, there is some evidence of current shorting and power loss in the convolute, too few shots were taken to optimize gas valve operation for zipper elimination. In addition, because Saturn has a substantially lower front end inductance than Double Eagle, power flow problems may be reduced by using a smaller initial load inductance, i.e. use a 2 cm rather than a 3 cm length load.⁹

The Saturn long pulse equivalent circuit model and a sample calculated current trace for a 400 $\mu\text{g}/\text{cm}$ load modeled as a 7 cm diameter uniform fill configuration are displayed in Fig. 17. The model was developed by Ken Struve (Mission Research Corp.), Chris Deeney and our Branch. The open circuit voltage profile was obtained by solving the equivalent short circuit equation ($V_L = 0$) using the value of the measured short circuit current profile. This equivalent circuit approximately matched the peak current and implosion time measured experimentally for a 2 cm length, 615 $\mu\text{g}/\text{cm}$ aluminum wire array long pulse experiment. Full validation of this circuit model will require a comparison of calculated and measured current traces from future wire array and gas puff experiments.

Figure 18 illustrates theoretically that Saturn in the long pulse mode is an excellent test bed for DECADE QUAD. This figure shows a comparison between DECADE QUAD and Saturn for implosion time, energy coupling, peak current, and η^* as a function of mass for a 6 cm diameter, 3 cm long, uniform fill argon load. To establish a baseline for evaluating future Saturn long

pulse experiments, Figure 19 displays the I^2 projection to DECADE QUAD of the K-shell yields obtained from the five argon gas puff experiments. These projected DECADE QUAD yields are about a factor of two lower than were obtained from the Double Eagle experiments. In the absence of power flow problems and assuming that the 7 cm diameter uniform fill nozzle performs more like a 6 cm nozzle (B. Weber), the experimental implosion times (Fig. 19) indicate that the Saturn experiments also took place in a low η^* ($\eta^* \leq 1.5$) regime, see Fig. 18. However the load mass, which is estimated to be $400 \mu\text{g}/\text{cm}$ for the best Saturn yield shot, is larger than the mass of the highest yielding Double Eagle long pulse experiment, which is estimated to be $260 \mu\text{g}/\text{cm}$.

D. Conclusions

The PRS community should be very encouraged by the argon K-shell yields obtained on Double Eagle long pulse with the 7 cm diameter uniform fill load configuration. This load design I^2 scales to over 40 kJ of K-shell emission on DECADE QUAD.

However, here is reason for concern about some of the long pulse experimental results because the maximum Double Eagle and Saturn K-shell yields were attained in a low η^* regime. There is theory support (Fig. 14) and experimental evidence (aluminum experiments on Saturn and Z) that yield saturation can occur in this regime for large mass loads, which makes yield saturation a relevant concern for DECADE QUAD. The Saturn K-shell yields support this concern because the Saturn loads were more massive than the Double Eagle loads but yet they scaled well short of 40 kJ to DECADE QUAD. However, given that the Saturn experiments were so preliminary, non-optimized, and showed possible power flow difficulties it would be prudent to not base any strong conclusions on the initial performance of the Saturn argon loads. In light of the excellent Double Eagle yields, it requires a more solid benchmark set of experiments on Saturn before being overly concerned about yield saturation in the low η^* regime at large load mass.

It is encouraging that a comparison of the enhanced to non-enhanced voltage experimental Double Eagle K-shell yields reveals that the 7 cm diameter uniform fill load is in an I^4 scaling regime, which implies that the 40 kJ projected DECADE QUAD yield is a conservative projection. The I^4 yield scaling also implies that the peak efficiency for K-shell yield production using the 7 cm diameter nozzle has not, to date, been achieved. Experiments at higher current levels are

needed in order to determine this nozzle's peak efficiency. If efficiency is defined as the K-shell yield divided by the coupled energy as calculated from snowplow model with a 10:1 compression ratio, then the maximum efficiency obtained so far from the Double Eagle long pulse experiments is 15 % (17.3 kJ/112 kJ). For comparison purposes the efficiency for the optimal short pulse argon load is 23 % (22 kJ/ 96 kJ).

Given the success of the Double Eagle long pulse experiments it is time to consider doing experiments on Double Eagle at larger diameter than 7 cm in order to take better advantage of the additional energy available on DECADE QUAD at large diameter. Figure 20 illustrates that DECADE QUAD can theoretically couple substantially more energy to a 10 cm diameter than a 7 cm diameter uniform fill load. It is apparent from the ratio of DECADE QUAD to Double Eagle coupled energy that the I^2 scaling of Double Eagle yields to DECADE QUAD also improves with increased initial diameter. Another advantage to performing experiments with a larger radius load is K-shell yield production at higher η^* values can be investigated, which will help mitigate any concerns about K-shell yield scaling in the low η^* regime. Figure 21 clearly demonstrates that on Double Eagle a 10 cm diameter load couples more energy to higher η^* loads than does the 7 cm diameter uniform fill load. The K-shell yield production efficiency dropped from 23 % for the short pulse 2.5 cm diameter shell load to 15 % for the 7 cm diameter long pulse load. A further reduction in efficiency is expected from even larger diameter Double Eagle loads because, unlike DECADE QUAD, there is no additional energy to be tapped at larger diameter. It would still be interesting to investigate yield fall off with increasing load diameter.

References

1. K. G. Whitney, J. W. Thornhill, J. P. Apruzese, and J. Davis, *J. Appl. Phys.* 67, 1725 (1990).
2. J. W. Thornhill, K. G. Whitney, and J. Davis, *J. Quant. Spectrosc. Radiat. Transfer* 44, 251 (1990).
3. C. Deeney, T. Nash, R. R. Prasad, L. Warren, K. G. Whitney, J. W. Thornhill, and M. C. Coulter, *Phys. Rev. A* 44, 6762 (1991).
4. J. W. Thornhill, K. G. Whitney, C. Deeney, and P. D. LePell, *Phys. Plasmas* 1, 321 (1994).
5. This circuit model was obtained from Phil Spence and Pat Corcoran of Pulse Science Inc.
6. C. Deeney, T. J. Nash, R. B. Spielman, J. F. Seaman, J. S. McGurn, D. O. Jobe, M. F. Vargas, T. L. Gilliland, R. C. Mock, K. W. Struve, K. G. Whitney, P. E. Pulsifer, J. P. Apruzese, J. W. Thornhill, and J. Davis, *Phys. Plasmas* 5, 2431 (1998).
7. J. P. Apruzese, P. E. Pulsifer, J. Davis, R. W. Clark, K. G. Whitney, J. W. Thornhill, T. W. L. Sanford, G. A. Chandler, C. Deeney, D. L. Fehl, T. J. Nash, R. B. Spielman, W. A. Stygar, K. W. Struve, R. C. Mock, T. L. Gilliland, D. O. Jobe, J. S. McGurn, J. F. Seamen, J. A. Torres, and M. Vargas, *Phys. Plasmas*, 5, 4476 (1998).
8. J. W. Thornhill, K. G. Whitney, J. Davis, and J. P. Apruzese, *J. Appl. Phys.* 80, July 15, (1996).
9. Private communication from Chris Deeney of Sandia National Laboratory.

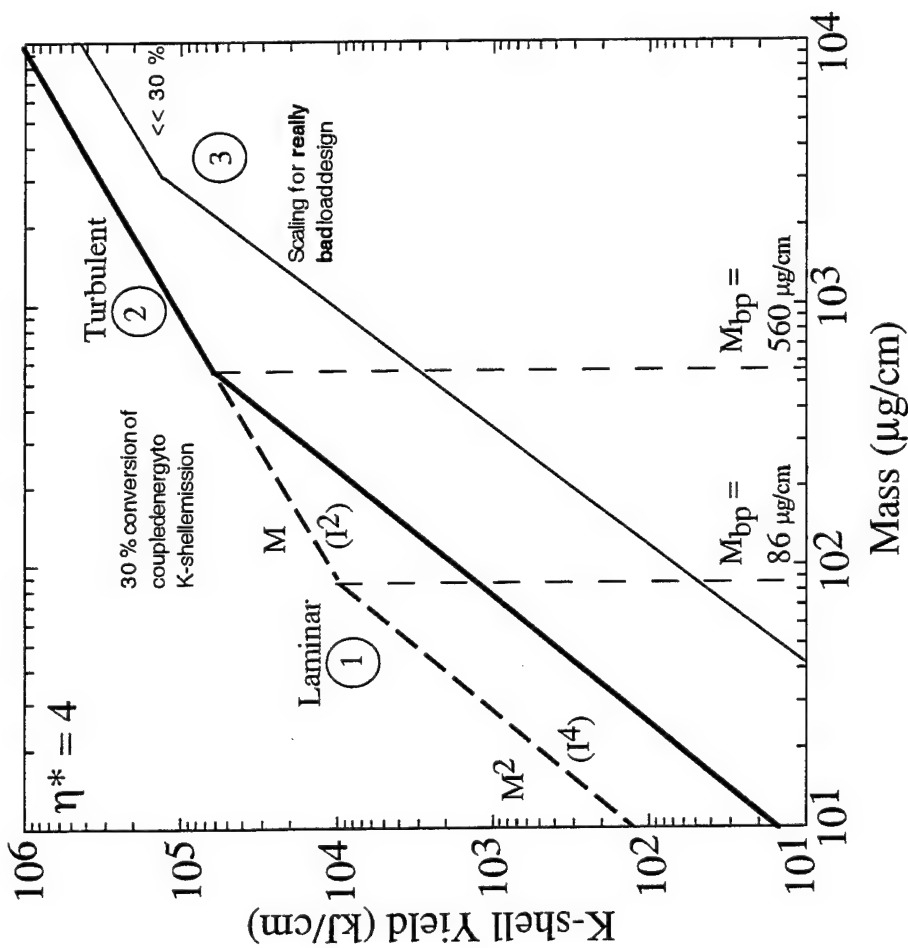


Fig. 1 K-shell yield as a function of load mass for three 1D model conditions.

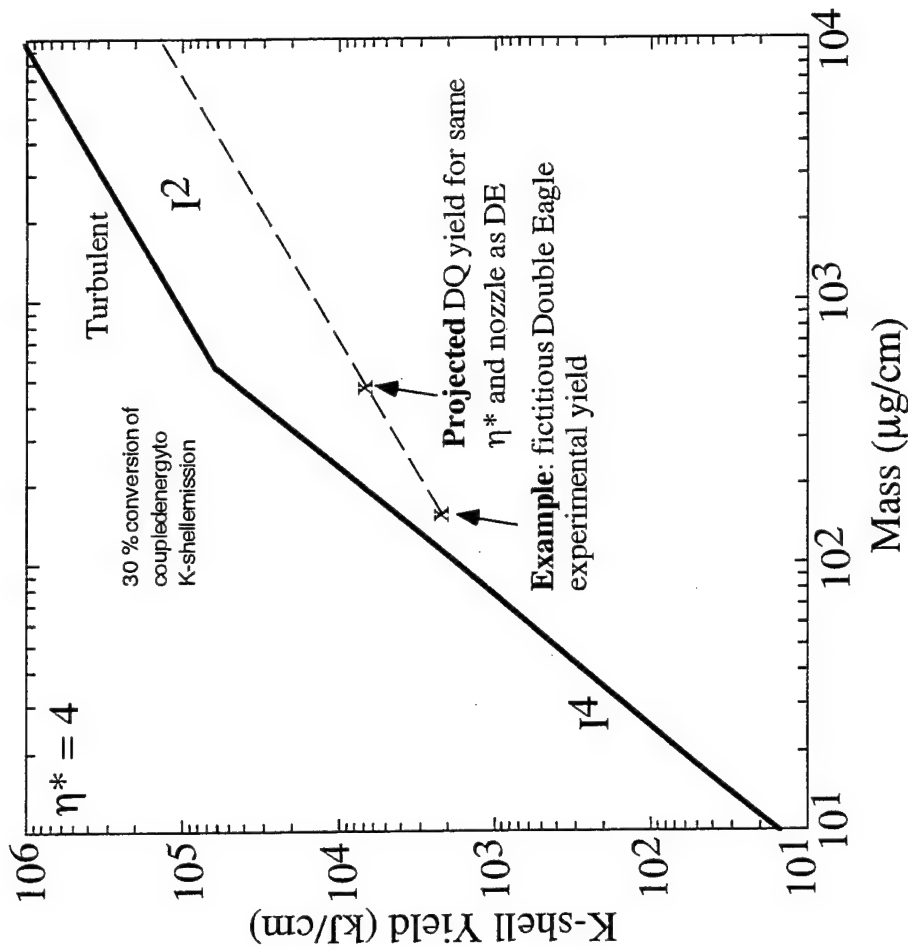


Fig. 2 Example of energy (I^2) scaling of Double Eagle K-shell yields to DECADE QUAD.

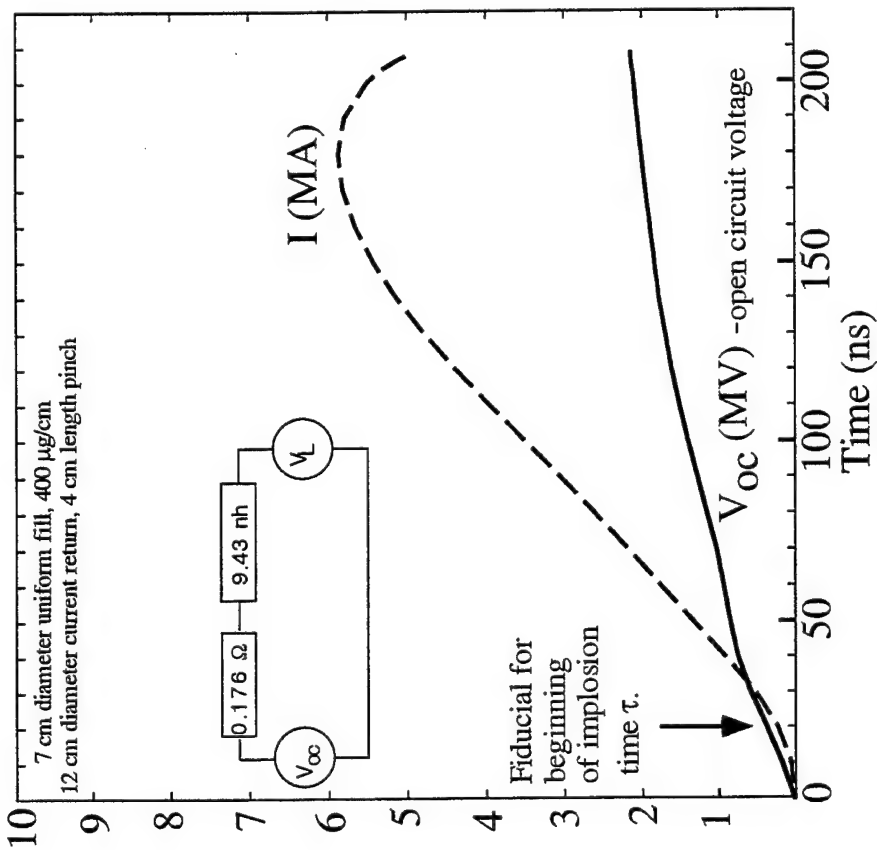


Fig. 3 Equivalent circuit model and sample load current for DECADE QUAD - Water Convolute design.

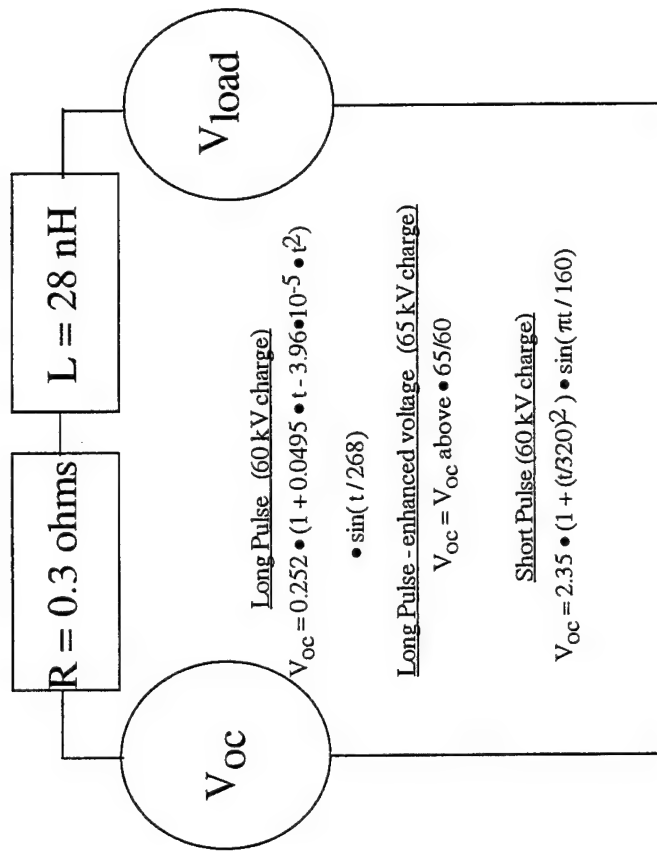


Fig. 4 Equivalent circuit model for Double Eagle gas puff experiments. V_{OC} in MV and time t in ns.

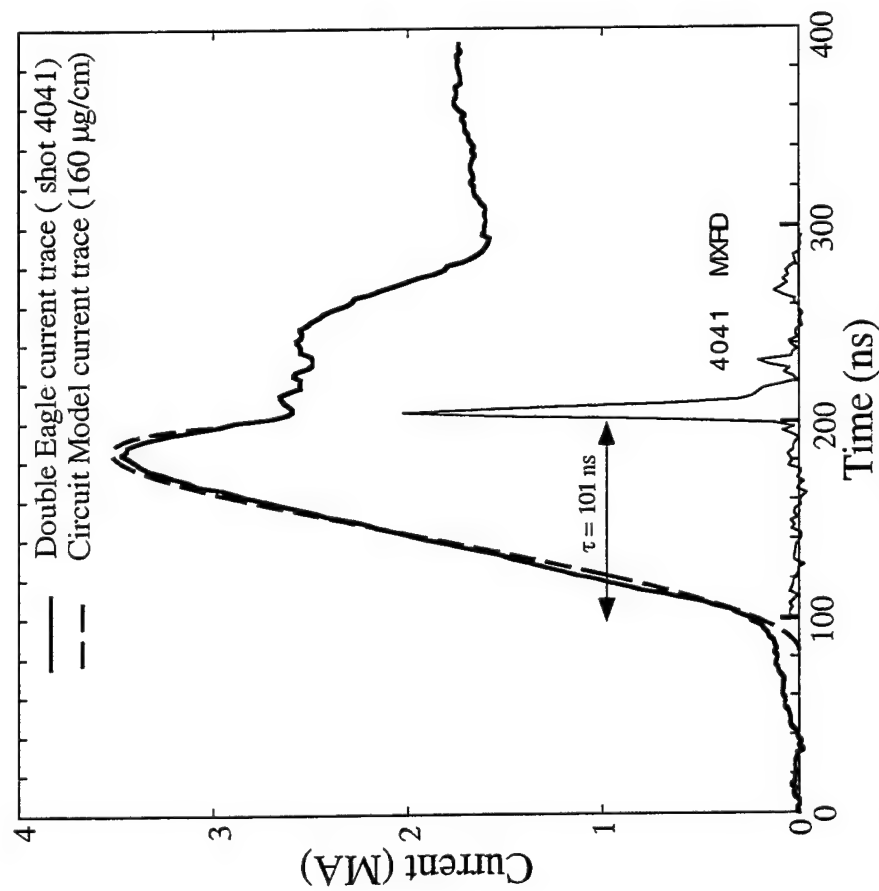


Fig. 5 Measured and calculated current trace for Double Eagle shot 4041, which was a short pulse, 2.5 cm diameter, 4 cm long shell implosion. A 160 mg/cm load was used in the calculation. The uncalibrated XRD trace is also displayed for shot 4041.

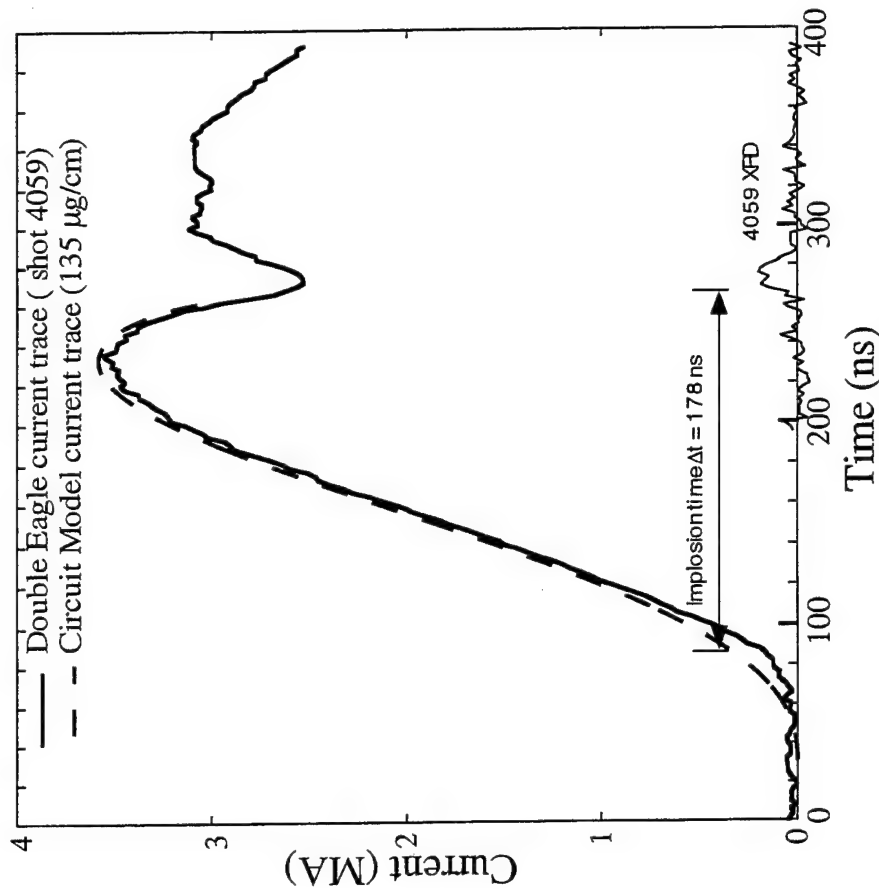


Fig. 6 Measured and calculated current trace for Double Eagle shot 4059, which was a long pulse, non-enhanced voltage, 7 cm diameter, 4 cm long, uniform fill implosion. A 135 $\mu\text{g}/\text{cm}$ load was used in the calculation. The uncalibrated XRD trace is also displayed for shot 4059.

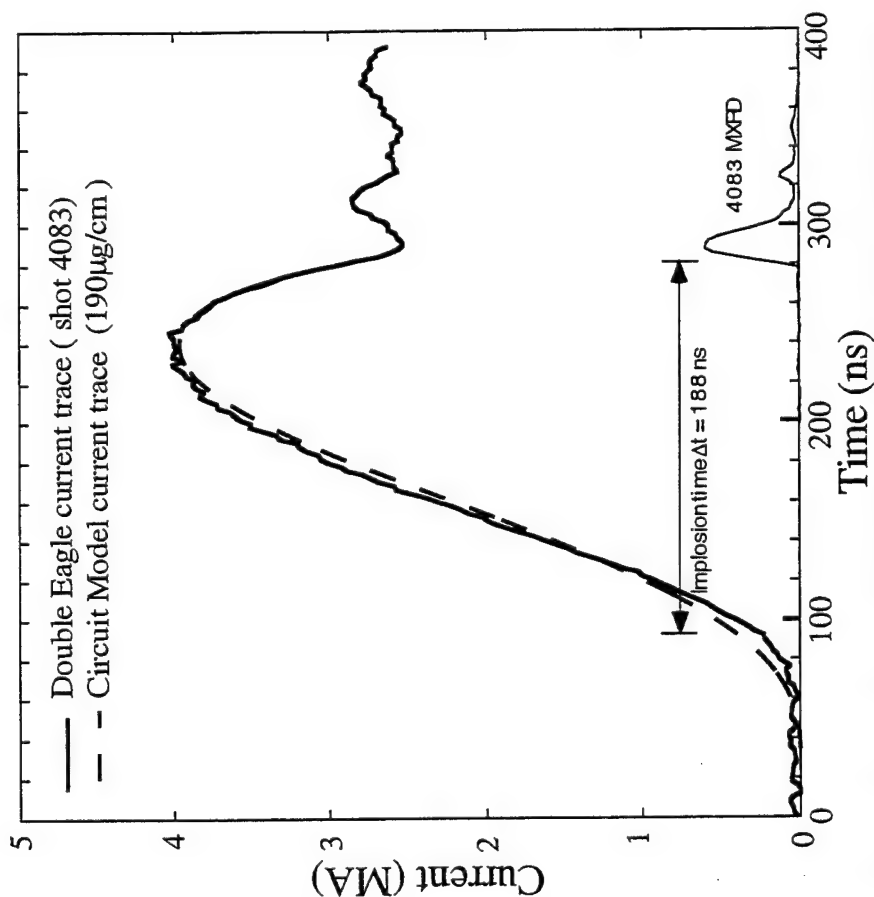


Fig. 7 Measured and calculated current trace for Double Eagle shot 4083, which was a long pulse, 7 cm diameter, enhanced voltage, 4 cm long, uniform fill implosion. A 190 $\mu\text{g}/\text{cm}$ load was used in the calculation. The uncalibrated XRD trace is also displayed for shot 4083.

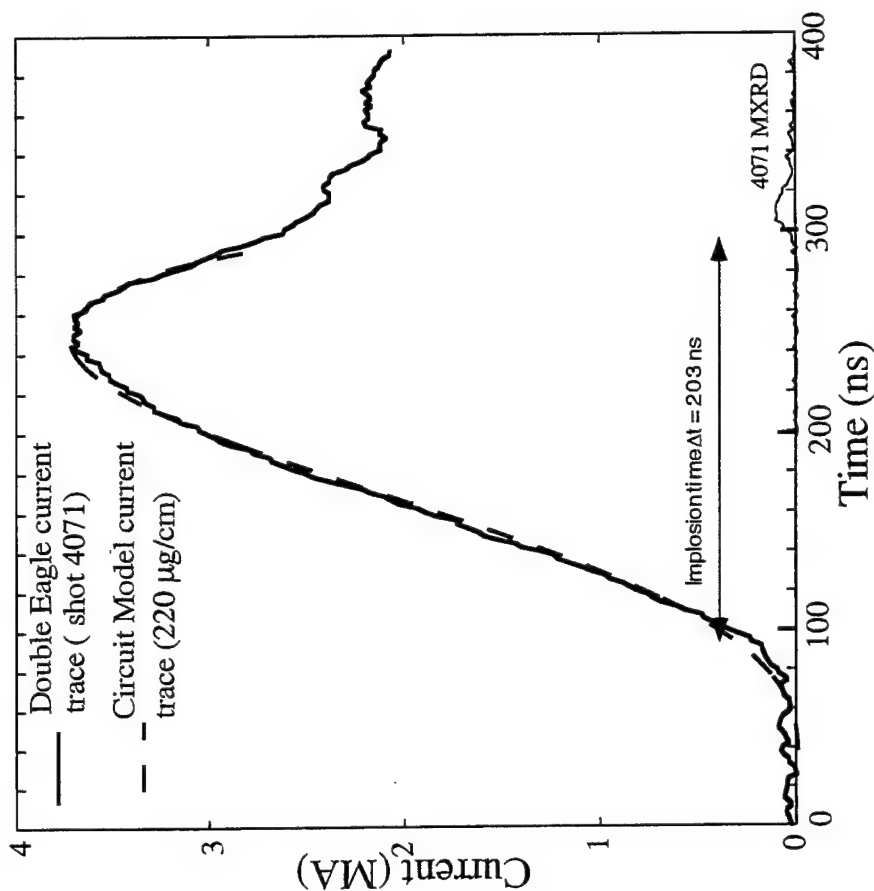


Fig. 8 Measured and calculated current trace for Double Eagle shot 4071, which was a long pulse, 5.0 cm diameter, 4 cm long, shell implosion. A 220 $\mu\text{g}/\text{cm}$ load was used in the calculation. The uncalibrated XRD trace is also displayed for shot 4071.

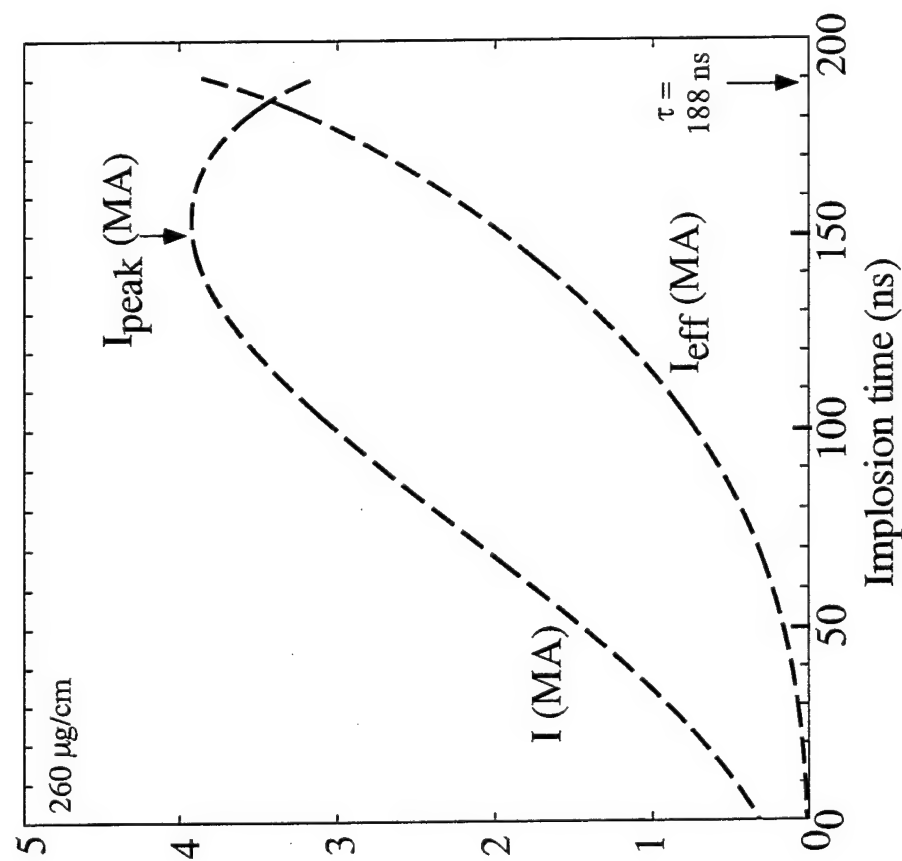


Fig. 9 Calculated peak current I_{peak} and effective current I_{eff} for shot 4083, which is modeled as a long pulse, enhanced voltage, 260 $\mu\text{g}/\text{cm}$, 6 cm diameter, uniform fill load. I_{eff} represents a current normalization on the coupled energy.
 $I_{\text{eff}} = ((\text{coupled energy in Joules/cm}) / (1.8 \times 10^3))^{1/2}$.

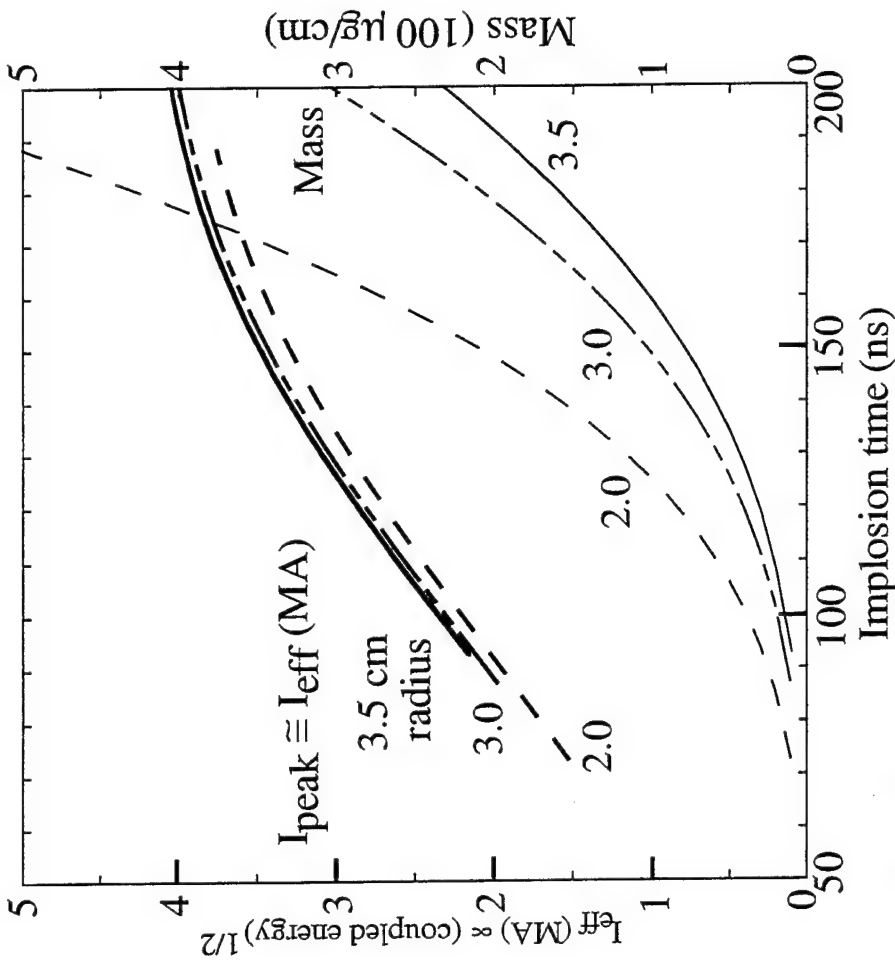


Fig. 10 Calculated effective current I_{eff} and mass load as a function of implosion time for uniform fill loads with initial radii of 3.5, 3.0 and 2.0 cm.

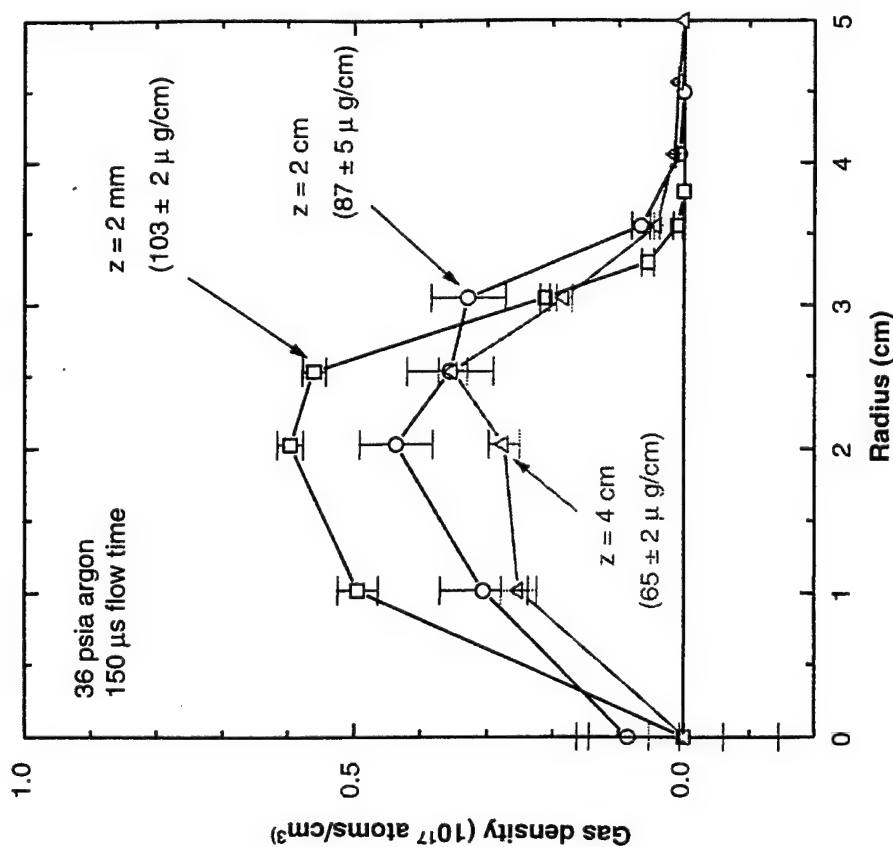


Fig. 11 Axial and radial density profiles for the 7 cm diameter uniform fill nozzle. Obtained from B. Weber (NRL Code 6770).

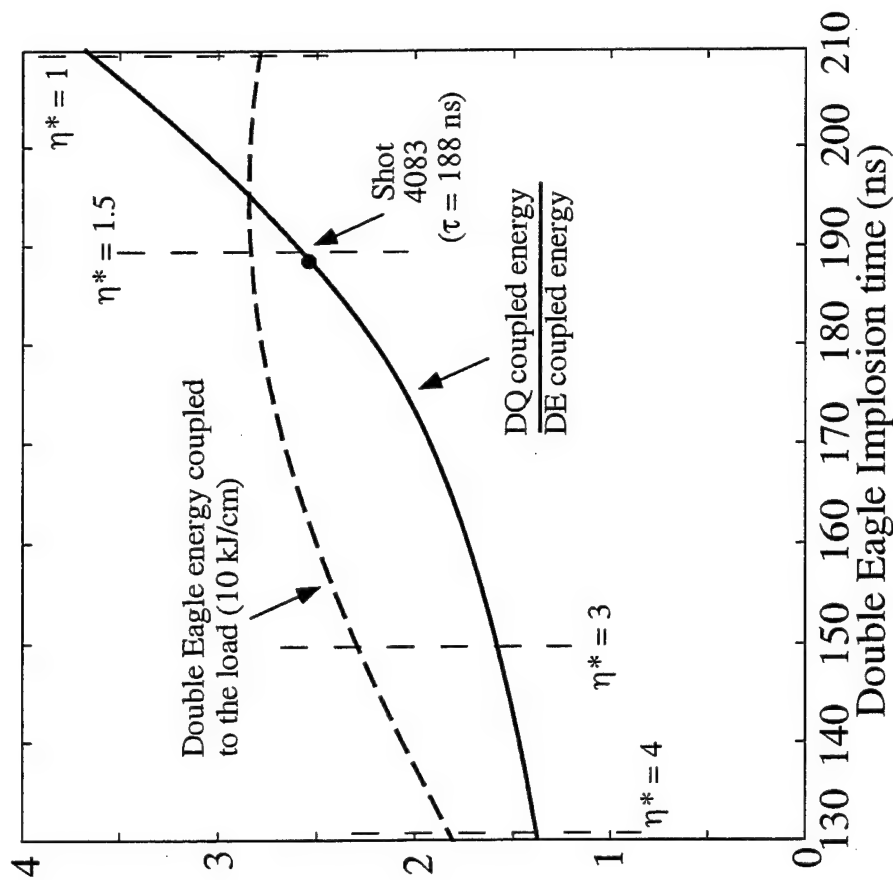


Fig. 12 Calculated Double Eagle energy coupled to the load and ratio of DECADE QUAD to Double Eagle coupled energy as a function of long pulse Double Eagle implosion time. Loads are modeled as enhanced voltage, 4 cm long, 7 cm diameter, uniform fill loads with 12 cm diameter current return posts.

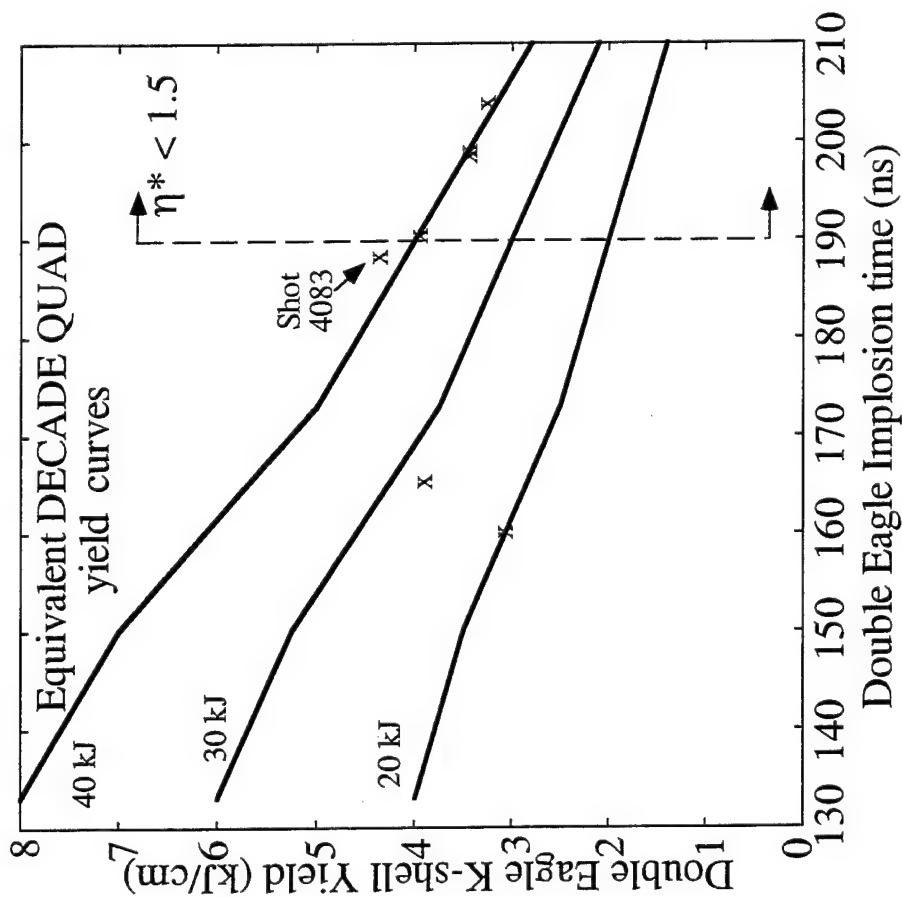


Fig. 13 Equivalent DECADE QUAD yield curves show how the experimental Double Eagle K-shell yields, which are plotted against implosion time, η^2 project to DECADE QUAD. Loads are long pulse, enhanced voltage, 4 cm long, 7 cm diameter, uniform fills.

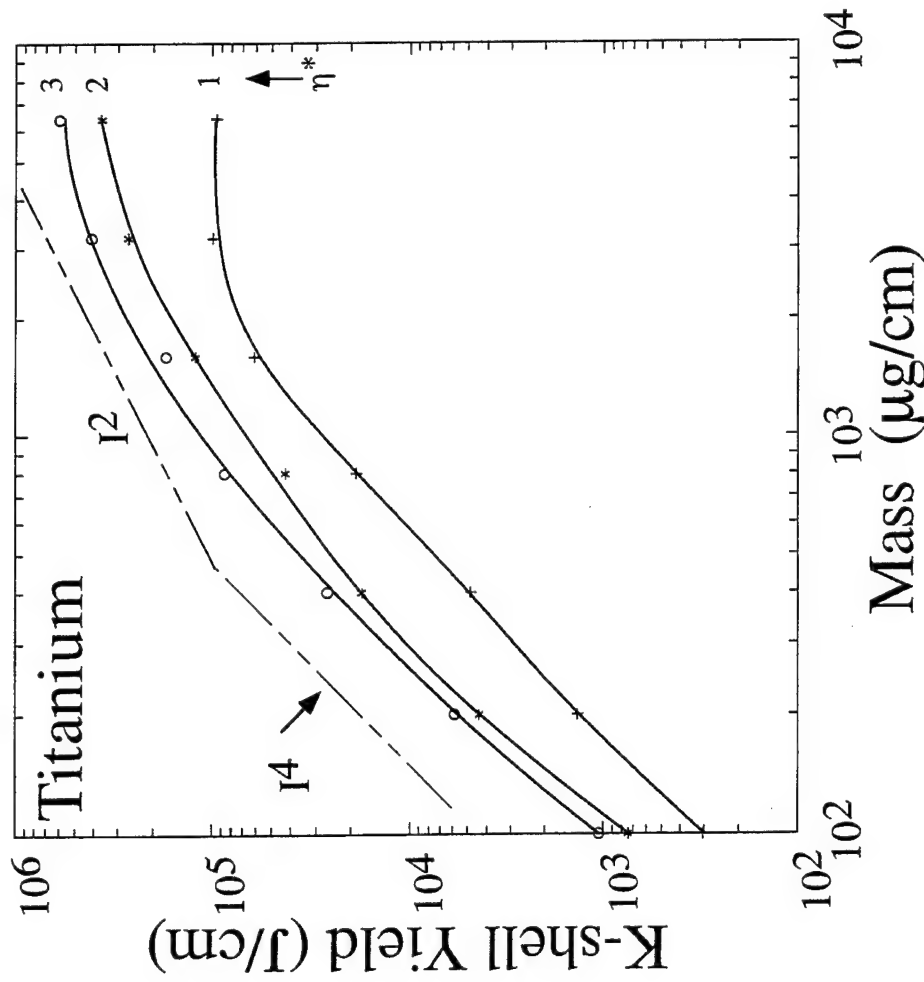


Fig. 14 Calculated titanium K-shell yields as a function of mass load and η^* .

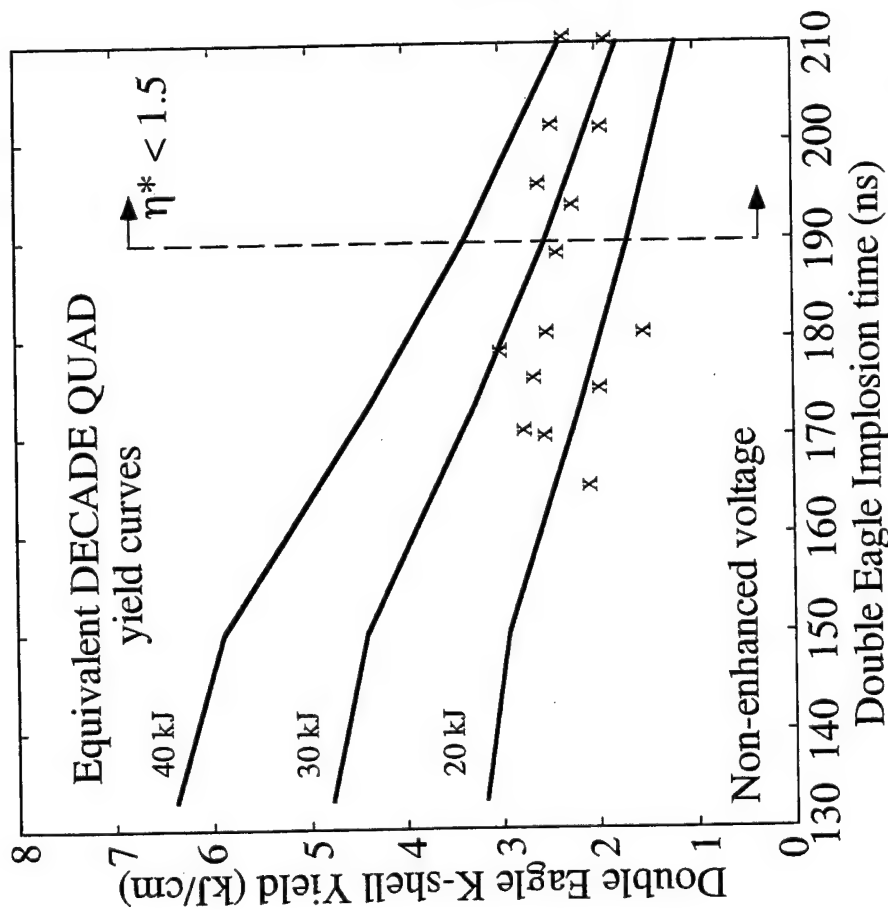


Fig. 15 Equivalent DECADE QUAD yield curve show how the experimental Double Eagle K-shell yields, which are plotted against implosion time, I^2 project to DECADE QUAD. Loads are long pulse, non-enhanced voltage, 4 cm long, 7 cm diameter, uniform fills.

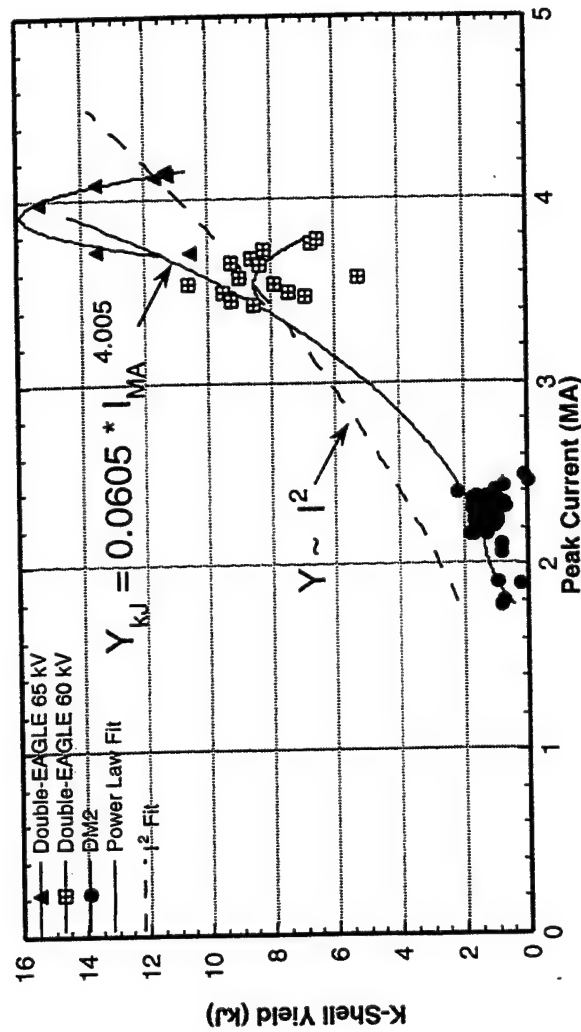


Fig. 16 Experimental Argon K-shell yields as a function of Peak current. Obtained from J. Riordan (Maxwell Tech. / PI)

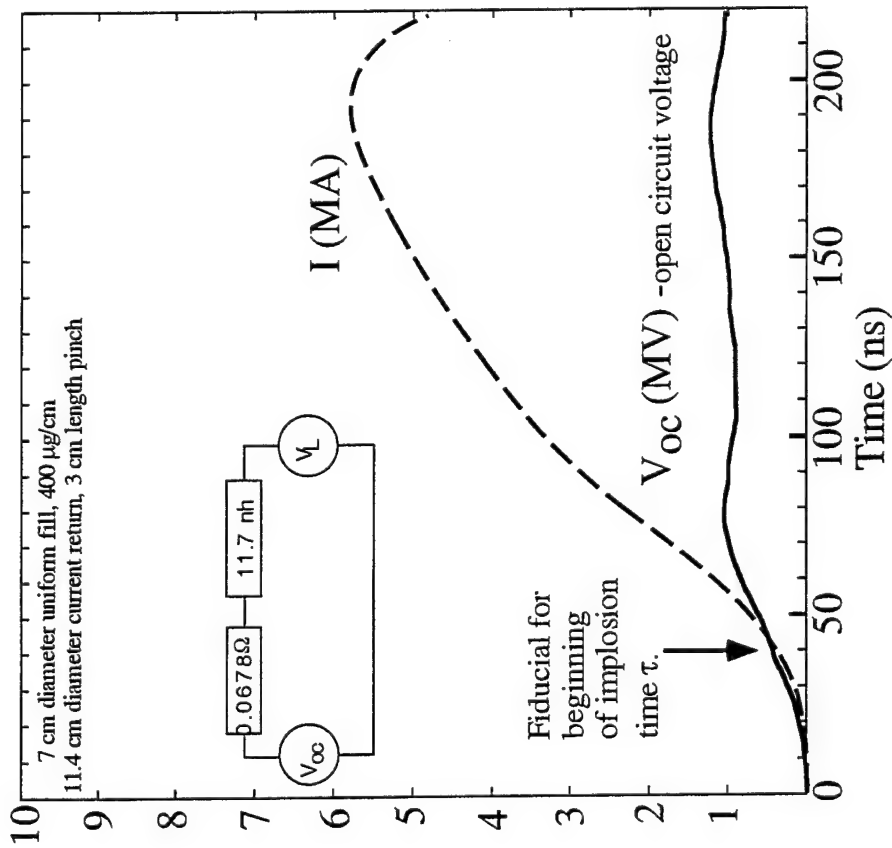


Fig. 17 Saturn long pulse equivalent circuit model and sample calculated current trace.

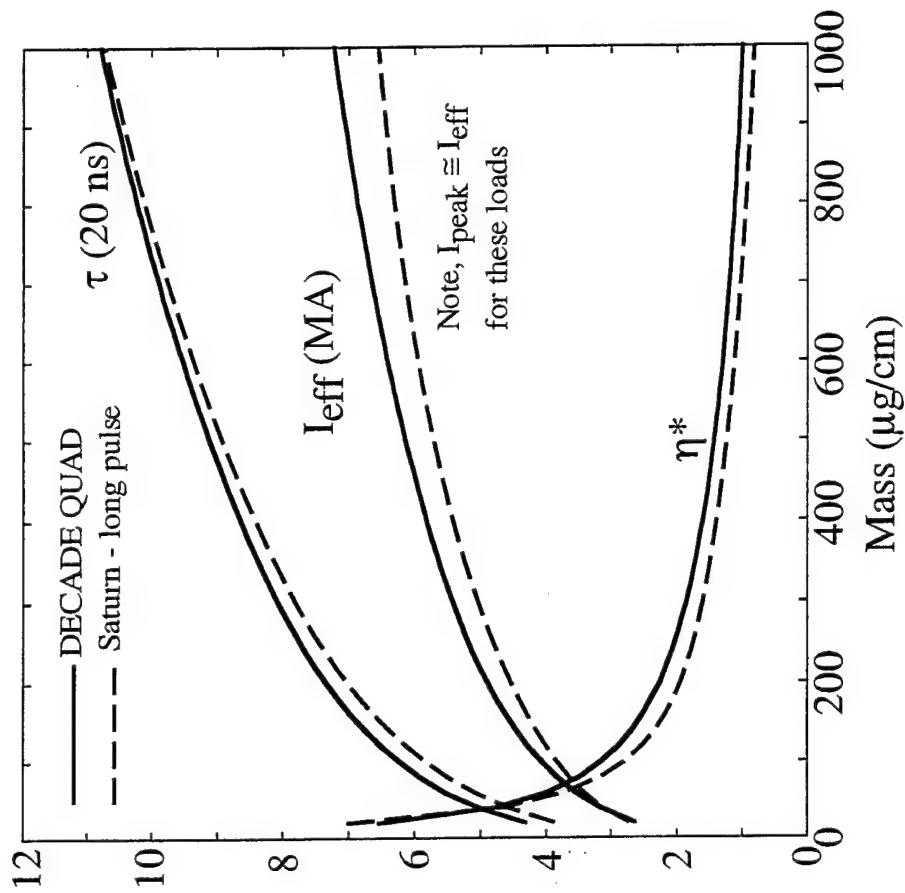


Fig. 18 Calculated DECADE QUAD and long pulse Saturn implosion times, effective currents, and η^* values as a function of load mass. Load is modeled as a 3 cm long, 6 cm diameter, uniform fill with 11.4 cm diameter current return posts.

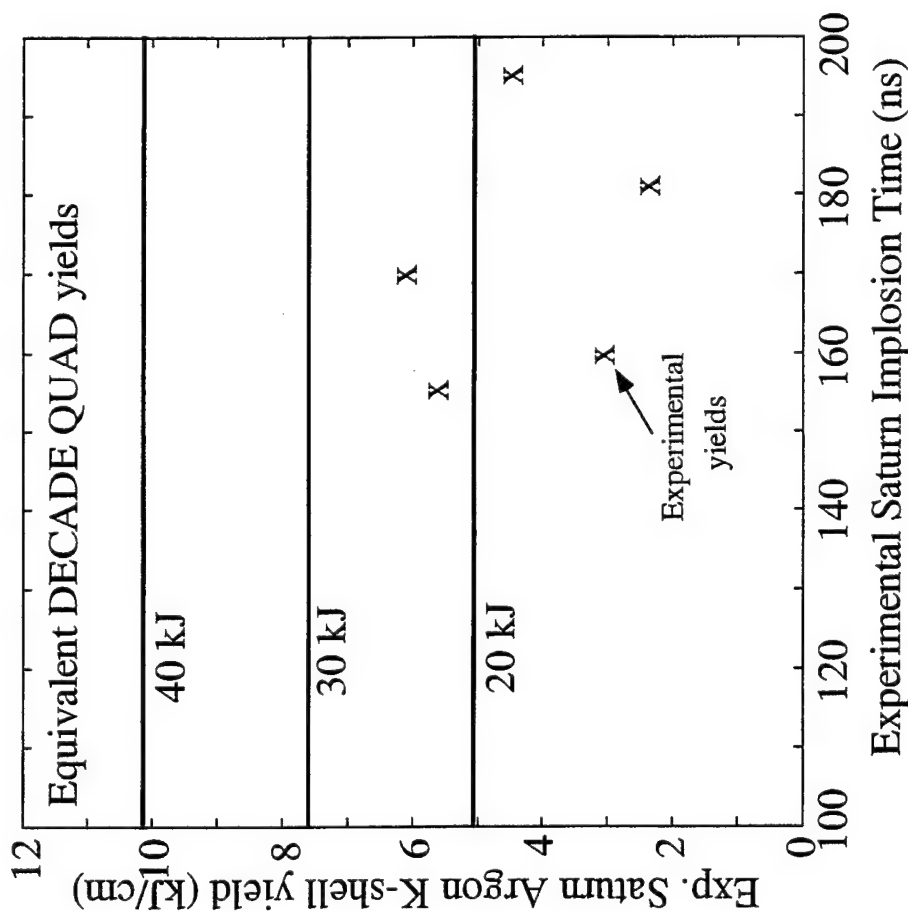


Fig. 19 Equivalent DECADE QUAD yield curves show how the experimental Saturn long pulse K-shell yields, which are plotted against implosion time, I^2 project to DECADE QUAD. Loads are 3 cm long, 7 cm diameter, uniform fills with 11.4 cm diameter current returns.

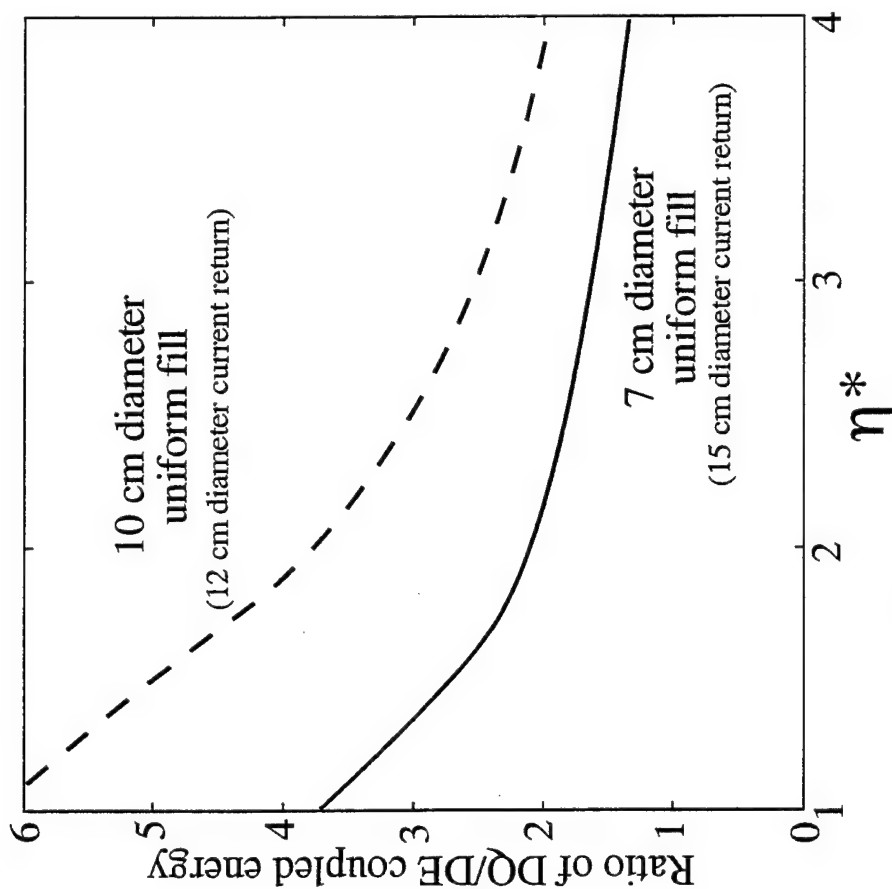


Fig. 20 Ratio of DECADE QUAD to Double Eagle (long pulse enhanced voltage) coupled energy as a function of η^* and uniform fill diameter. Loads are 4 cm long.

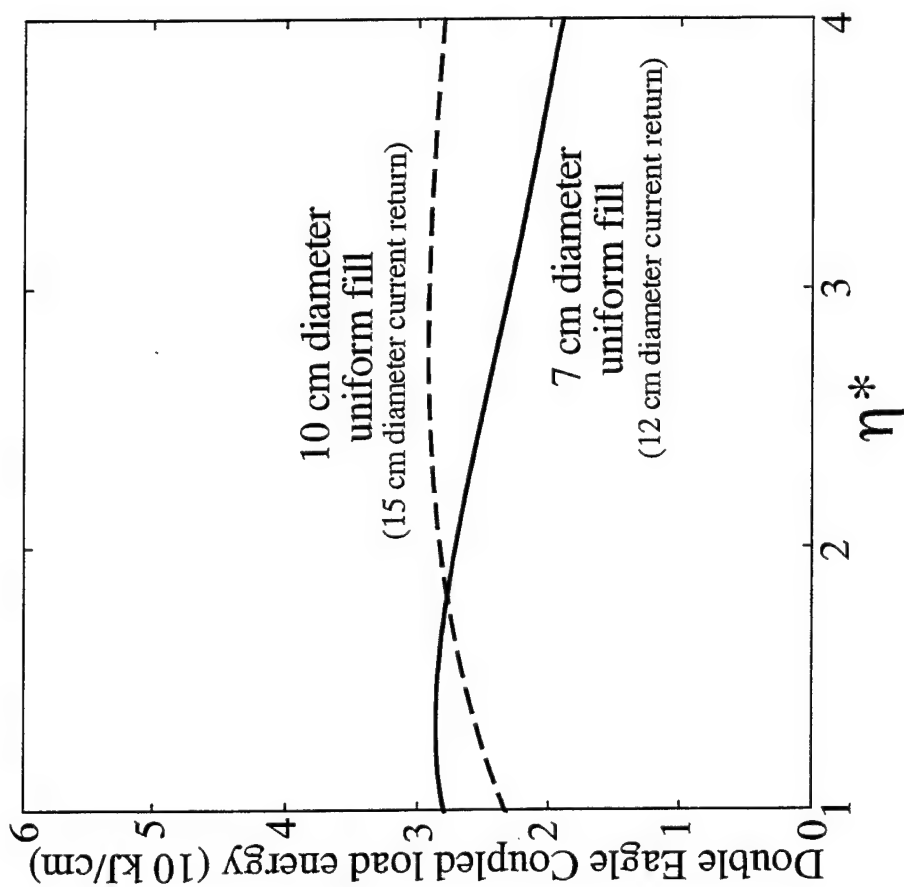


Fig. 21 Calculated Double Eagle long pulse coupled load energy as a function of η^* and uniform fill diameter. These enhanced voltage loads are modeled as being 4 cm long.

V. Wire Dynamics Model with Application to Nested Arrays

1 Introduction

In plasma radiation sources (PRS), Z-pinch loads are imploded to generate a large yield of soft x-rays.¹ The performance of a PRS is known to be very sensitive to the stability of implosions. Better stability often means a tighter Z-pinch at the stagnation phase, a more uniform radiating plasma, and therefore, higher radiative output — particularly in the K-shell. Two- and three-dimensional effects in the form of instabilities and asymmetries can broaden x-ray pulsewidths, lower x-ray powers and lower yields compared to one-dimensional calculations. However these same instabilities can also act, in some cases, to slow the load assembly, limit the dynamic range of load inductance, and allow more energy into the load via a smooth squeezing than is delivered as primary kinetic energy. Thus, while some enhancement of available energy may arise through two- and three-dimensional effects, the higher powers in experiment are seen with tighter pinches. This indicates a considerable potential for improving radiative performance of existing pulsed power facilities by making the PRS implosions more uniform and stable, which has clearly been demonstrated by enhancements in x-ray power through increasing the wire number to improve the initial uniformity of the wire arrays.^{2,3,4}

Early experiments, starting with puff-on-puff⁵ and double puff^{6,7} loads demonstrated the ability of structured Z-pinch loads to increase the uniformity of the stagnated plasma by mitigating the growth of implosion instabilities. Russian experiments with gas-puff-on-wire-array complex loads on the GIT-4 generator have shown a remarkable increase in the aluminum K-shell yield and radiative power due to fast switching of the pinch current from the outer gaseous shell to the inner wire array.^{8,9} Recent efforts on this path have been fielded on the "Z" facility¹⁰ at SNL, using fully nested wire array loads^{11,12,13} and showing radiated powers greater than any other style of PRS load.

As discussed by Deeney *et al* and Douglas *et al*, 2D r-z radiation-MHD modeling of the nested wire implosions on Z captured some of the dynamics

and the trends in power increase and pulsewidth decrease. However, there were some unexplained differences between the experiment and the calculations. In agreement with recent puff-on-puff experiments¹⁴ where the mass layers cannot interpenetrate, r-z modeling generally predicts better yields for a *higher* mass fraction on the interior, while nested wire shots showed higher yields for a *lower* interior mass fraction. Therefore, to describe the nested array experiments accurately, we must include the effects of current commutation caused by a mass interchange, or subduction, when the drive array is swept inside the target array. Clearly such modeling is outside the scope of a 2D r-z code.

To analyze these effects, we first discuss a wire dynamics model for this type of load design. A practical wire dynamics model (WDM) treats the individual wire segments of an array load as a fully self-consistent electrical and mechanical ensemble. From a mechanical viewpoint the segments are mutually interacting particles driven by Biot-Savart force to attract or repel one another according to the currents each carries. Electrically, the segments are viewed as mutually inductive circuit elements that remain connected in parallel to the driving circuit but are otherwise free to move about the solution domain and free to partition the input current among all the parallel paths. Complete electrical and mechanical self-consistency is an absolute requirement for the accurate modeling of the experiment. Two versions of the wire dynamics, non-collisional and collisional, are discussed.

We next discuss the evolution of the nested wire arrays in early, first strike, and stagnation phases, comparing expectations from two simplified dynamics limits: filamentary (the WDM picture) and annular (conventional 0D picture). We compare the two models with a set of experiments. The best yield and power case expected from the filamentary model agrees with the experimental observations. The annular model fails to describe the observed trends in the implosion kinematics. Next we discuss the fraction of mass transmitted as nested arrays collide within the context of a collisional WDM, and develop a simple rule for assessing that fraction when the ensemble's motion is fairly regular. Finally we apply the full model to the problem of filamentation in a wire array load and show how modest mass perturbations can drive noticeable levels of instability.

2 Wire Dynamics Model

Both the wires and the back current posts are considered an ensemble of straight conductors, parallel to the axis, carrying currents, \mathcal{J} . A return current post is equivalent to a wire of enormous mass and reversed current in terms of formulating the model, but in practice a population of return current posts is simply held fixed. If such posts are input to a given calculation, they are presumed to be distributed symmetrically in azimuth at a fixed radius. Any such regular placement of array properties serves to define a “symmetry group” within the ensemble; the symmetry groups thus show a multiplicity (\mathcal{M}), e.g.

$$\mathcal{I} = \sum_{is=1,1}^{\mathcal{N},\mathcal{M}} \mathcal{J}_{i,s} = \mathcal{M} \sum_{i=1}^{\mathcal{N}} \mathcal{J}_i .$$

The number of linked “symmetry groups” in a calculation is always equal to the post number if posts are used, but may become a free parameter when a continuous return current “can” is employed.

The particulate circuit elements within a symmetry group must be electrically and mechanically indistinguishable, meaning here that $m_{is}, \delta_{is}, \mathcal{Z}_{is}$, representing mass, wire radius, and wire impedance are *invariant* over the group index, s . Once distributed at symmetric locations, $[x_{is}^0, y_{is}^0]$, the evolved velocities and positions $[x_{is}, y_{is}, \dot{x}_{is}, \dot{y}_{is}]$ will preserve this symmetry around in azimuth and bring all particles in the symmetry group to the same evolved radius — *for all possible currents, and pairwise interactions among these particles.*

2.1 “Transparent” Wire Model

When the wires are not allowed any interaction, viz. when they are viewed as uniformly massed rods carrying current at some radius δ that simply pass through one another, then the model equations depend upon only the set of wire locations, masses, radii and currents. The trajectories of this wire element ensemble are followed, integrating

$$m_{is} \ddot{\mathbf{x}}_{is} = \left(\frac{\mu_0}{2\pi} \right) \left(\sum_{p,j \neq i} \frac{\mathcal{J}_{i,s} \mathcal{J}_{j,p}}{r_{ij}} \hat{\mathbf{x}}_{ij}^{sp} + \sum_{p \neq s} \frac{\mathcal{J}_{i,s}^2}{r_{ii}} \hat{\mathbf{x}}_{ii}^{sp} \right) .$$

Here we have used the unit vectors:

$$\hat{\mathbf{x}}_{ij}^{sp} = \frac{(x_{jp} - x_{is})}{{}_{sp}\mathcal{R}_{ij}} \quad \hat{\mathbf{y}}_{ij}^{sp} = \frac{(y_{jp} - y_{is})}{{}_{sp}\mathcal{R}_{ij}} ,$$

and the distance variable:

$${}_{sp}\mathcal{R}_{ij}^2 = (x_{is} - x_{jp})^2 + (y_{is} - y_{jp})^2 .$$

Of course the wire arrays used as PRS are predominantly inductive loads, and accordingly a major feature of our model is a self-consistent calculation of the current distribution over the wires and the back current posts due to inductive coupling. Early linear stability analysis¹⁵, and estimates for compression ratio limits¹⁶ associated with azimuthal asymmetries, were obtained under the assumption that the current distribution over the wires is either uniform or otherwise prescribed. Other linear stability analysis¹⁷ included perturbations on the inductance and current, but was limited to small excursions from equilibrium and slowly varying background conditions. Generally all such specializing assumptions are clearly erroneous in the case of dynamic Z-pinch loads and can generate misleading results.

The correct inductive partition of current involves the flux $\Phi(t)$ and an inductance matrix,

$$\Phi(t) = \mathcal{M} \cdot \sum_{j,p} {}_{i,s}\mathcal{L}_{j,p} \mathcal{J}_{j,p} ,$$

with self inductances for wires of radius δ in a return current can of radius a and length h given by ${}_{i,s}\mathcal{L}_{i,s} = (\frac{\mu_0 h}{2\pi}) \cdot (\ln(a^2 - x_{is}^2 - y_{is}^2) - \ln(a\delta))$, and mutual inductances in a return current can by

$${}_{i,s}\mathcal{L}_{j,p} = (\frac{\mu_0 h}{2\pi}) \cdot 0.5 \ln((a^2 - x_{is}x_{jp} - y_{is}y_{jp})^2 + (x_{is}y_{jp} - x_{jp}y_{is})^2) - \ln(a {}_{sp}\mathcal{R}_{ij}) .$$

An external circuit equation serves to update the flux required for the current partition using:

$$V_{oc} - Z_m \mathcal{I} - L_{fe} \frac{d}{dt} \mathcal{I} = \dot{\Phi} .$$

Here the open circuit voltage is V_{oc} , the equivalent machine impedance is Z_m , and the front end inductance is L_{fe} . All of these quantities are derived from machine data.

2.2 “Sticky” Wire Model

For all the simplicity offered in the “transparent” formulation above, the resulting dynamics is unsatisfactory for loads like nested arrays beyond the moment of “first strike”. If a realistic view of mass accretion and inductive current partition is to be had, then a means of dissipating wire kinetic energy when the filaments are close enough must be added. Clearly a full development of such interaction would require a complex 3D hydrodynamic model, but that is too ambitious to be useful. As an intermediate description, and one which can later be extended to a particulate hydrodynamic methodology, consider the addition of a drag force between the wire elements when they are sufficiently close together that a reasonable estimate of expansion speeds would begin to merge the wire coronas.

A pairwise drag force can be derived by separating the heavy wire cores from a common, light coronal “atmosphere”. The merged atmosphere provides a drag medium locked to the center of mass, so that an interacting wire pair will be slowed down with a force proportional to some power of the closing velocity relative to the center of mass. Without going into the full hydrodynamic picture to get all the details, the result is going to be fairly represented by a drag force like,

$$\mathbf{F}_{drag} = \mathcal{S}(\mathcal{R}_{ij}) \mathbf{V}_{ij}$$

with the scalar strength factor, $\mathcal{S}(\mathcal{R}_{ij}/[\delta_i + \delta_j])$, dependent upon the ratio of wire separation to wire diameter. The velocity dependence is linear and directed along the relative velocity $\mathbf{V}_{ij} = \dot{\mathbf{x}}_i - \dot{\mathbf{x}}_j$. The size of the drag region is the characteristic scale height for the strength factor, here taken as Gaussian in shape. It will be apparent below that the strength of the drag is not important once it goes above an easily distinguished threshold level. In a numerical sense the drag force strength calibration is like the selection of an artificial viscosity.

Hence the essential physics of the “Sticky” Wire Dynamic Model (SWDM) can be realized in following the orbit of a pair of wires coalescing in their center of mass frame. In the CM frame, the wire-to-wire distance $\mathcal{R}_{ij} \mapsto r$ the radial coordinate of a reduced mass particle (μ), while the relative velocity $\mathbf{V}_{ij} \mapsto \dot{r} \hat{\mathbf{r}}$. One retains a central force problem because the coronal atmosphere cannot produce a net torque on the system, viz. $\mathcal{L} = \mu r^2 \dot{\theta}$ is

constant. By assumption the atmosphere rotates with the angular momentum \mathcal{L} so that drag is produced only by motions which change the relative separation.

To develop the equation of motion for the radial coordinate it is convenient to introduce a length scale d_0 such that $\mathcal{R}_{ij} = r d_0$, and the average scale radius of a wire pair becomes $r_c = 1/2 [\delta_i + \delta_j]/d_0$. The length scale serves to define two important scale energies: for angular momentum, $e_\theta = \mathcal{L}^2/2\mu d_0^2$; and for the Biot-Savart potential, $\mathcal{V}(\mathcal{R}) = e_{\mathcal{J}} \ln[(\mathcal{R}/d_0)^2]$, with $e_{\mathcal{J}} = \mathcal{J}^2 h/c^2$. Selecting a time scale interval t_0 , and forming a fiducial energy $e_0 = \frac{\mu}{2} d_0^2 / t_0^2$, the complete equation of motion can be cast in terms of three dimensionless parameters,

$$\nu_\theta = \frac{e_\theta}{e_0},$$

$$\nu_{\mathcal{J}} = \frac{e_{\mathcal{J}}}{e_0},$$

and

$$\mathcal{S}\left(\frac{r}{r_c}\right) = \mathcal{S}_0 \cdot e^{\left(-\frac{r(t)^2}{r_c^2}\right)},$$

including in this set the scale factor \mathcal{S}_0 in our model drag force expression. Hence, the decaying orbit one obtains from

$$\ddot{r} = \frac{\nu_\theta}{r(t)^3} - \frac{\nu_{\mathcal{J}}}{r(t)} - \dot{r}(t) \mathcal{S}\left(\frac{r(t)}{r_c}\right)$$

is the primary statement of the sticky model. A typical orbital picture is shown in Fig. [5.1], it includes a plot of the energy dissipated into the drag medium as a function of time while the reduced particle comes to a (spinning) equilibrium. The energy so derived is just the time integral of the Rayleigh dissipation function for this problem, $\dot{T}_{diss} = 0.5 \dot{r}^2 \mathcal{S}(\frac{r}{r_c})$; and it is a well defined fraction of the potential energy available to a collision, $\mathcal{V}_{init} = e_{\mathcal{J}} \ln[\delta_0^2]$, as parameterized by the ratio $\delta_0 = \mathcal{R}_{init}/d_0$. As the colliding wires are brought to rest at an equilibrium radius lower than that for a non-dissipative orbit,

$$r_{eq} \ll \sqrt{\frac{\nu_\theta}{\nu_{\mathcal{J}}}},$$

some of \mathcal{V}_{init} will be dissipated, depending upon the violence of the collision.

2.3 Properties of Binary Encounters in the SWDM

When the relative motion of sticky wires is examined on the phase space defined by the dimensionless parameters $[\nu_\theta, \nu_J, \delta_0]$, a very regular picture of the dissipated energy emerges, Fig. [5.2].

As shown, a plot of the dissipated energy fraction \mathcal{F}_{diss} gives a regular family of logarithmic curves depending mostly on the angular momentum and weakly on the initial energy. Recall this is not the energy in the rotational degree of freedom, but only that in the radial one. The rms fit to the curve family over the range of δ_0 values cited is just

$$\mathcal{F}_{diss} \equiv \frac{\mathcal{E}_{diss}}{\mathcal{V}_{init}} = 0.20056 - 0.04705 \cdot \ln\left(\frac{\nu_\theta}{\nu_J}\right).$$

When applied in the context of a sticky wire ensemble, this rule of thumb is an accurate predictor of the energy dissipated as the entire group of wires is brought to rest. If the interaction length is large, forcing dissipation at higher values of angular momentum, a low fraction of available energy is lost. As the interaction length is made smaller, forcing collisions at lower angular momentum, more of the available energy is lost to the drag forces.

2.4 Laboratory Frame Implementation of the SWDM

For completeness, the transformation of this sticky wire picture back to the laboratory frame, where the simulation model is posed, results in the following dynamic statement for the wire ensemble

$$m_{is}\ddot{\mathbf{x}}_{is} = \left(\frac{\mu_0}{2\pi}\right)\left(\sum_{p,j \neq i} \frac{\mathcal{J}_{i,s}\mathcal{J}_{j,p}}{sp\mathcal{R}_{ij}} \hat{\mathbf{x}}_{ij}^{sp} + \sum_{p \neq s} \frac{\mathcal{J}_{i,s}^2}{sp\mathcal{R}_{ii}} \hat{\mathbf{x}}_{ii}^{sp}\right) \\ - \left(\sum_{p,j \neq i} \mathcal{S}(\mathcal{R})(\dot{\mathbf{x}}_{ij}^{sp}) + \sum_{p \neq s} \mathcal{S}(\mathcal{R})(\dot{\mathbf{x}}_{ii}^{sp})\right)$$

with the interaction strength and scale height in \mathcal{S} to be calibrated by comparison to experiment. With the addition of a cloud around each wire to represent its “atmosphere”, the model particles pick up an additional radial parameter, a_w , representing the time varying physical diameter of the wire cloud. The current radius δ_{is} still represents the wire inductively, and all

electrical calculations are done as before. The electrical and physical wire radii can evolve according to whatever physical constraints are reasonable. The pairwise interaction scheme is illustrated in Fig. [5.3].

3 Nested Wire Load Startup and Rundown

Initially, the current is mostly driven through the outer array, exploding it. In a typical "Z" shot the time required for this process can be estimated as $\tau_{pop} \approx \sqrt[3]{\frac{3 H_w}{R_w \dot{I}^2}}$ assuming a constant current rise at the rate \dot{I} , a fixed wire resistance R_w , and a known enthalpy H_w for vaporization and ionization of the wire material. For tungsten a typical array load would require $H_w \approx 32$ J, might exhibit an initial resistance $R_w \approx 200\Omega$, and see a current risetime $\dot{I} \approx 10^{13}$ A/s. Under such conditions the wires would be expected to be mostly plasma after a $\tau_{pop} \approx 2$ ns. If, as is likely, the wire resistance is not fixed but drops precipitously due to surface plasma expansions, then the time to deliver the energy dose needed for vaporization and ionization of the complete wire might stretch τ_{pop} out to ten ns.

In lower I -dot wire explosion experiments^{18,19}, each wire is observed to take on a very short range axial modulation in density, characterized by flares and pinched regions. A coronal plasma forms and expands many wire diameters, but the thin exterior plasma may carry little of the current while the wire array resistance remains small. At a typical expansion velocity of $1.5 \cdot 10^6$ cm/s, a 4 cm diameter, 240 wire array would see the gaps begin to close in perhaps $17 \rightarrow 25$ ns. This time frame is less than the timescale (approx 50 ns) for the array to begin to move significantly. As the coronal flares from the individual wires mix together, the current paths diffuse away from the wire cores, producing a nearly uniform plasma annulus. The time scale for such mixing and global diffusion is still an open question, and it certainly has not been measured on Z.

Once the drive array, or the annular plasma shell formed from it, approaches the target array, two distinct limits in the dynamics are possible. The sheet of drive array plasma might hit and stick to the target array material with significant, immediate energy and momentum transfer to the interior mass, depending on the expansion of the inner shell. Alternately, the imploded drive array plasma might penetrate through the gaps between the

target array's wires. In this case, as the drive plasma's subduction proceeds, the azimuthal magnetic field is stripped away —due to both the conductivity of the inner wires and the inductive coupling between the two arrays. Any interpenetration of the arrays thus causes a rapid switching of most of the total current to the (originally) interior target array. Moreover, the rapidity of such current transfer is all the greater as the drive array plasma is more completely smoothed out to a continuous annulus, because smoothing the drive array produces a more effective early screening of the current from the target. In contrast, the transfer of momentum after the driver's subduction is far from instantaneous, because the target array wires must be exploded and accelerated from zero velocity.

If a typical nested array shot is simulated with the WDM, the extent of current shielding of the target array is seen to be progressively more complete as the drive array wire number is increased. At 240 wires in the driver, ≤ 1 MA of current is seen in the target until the drive array is more than half way to the target. Such behavior is mirrored in a typical experimental shot by the observation of very low currents (≤ 300 kA) in an intermediate B-dot monitor until the drive array is seen to be very close to the detector location. Evidently the use of a filamentary model for the drive array has no appreciable effect on the precursor leakage current to the interior array. Precise agreement in leakage current requires more filaments in the drive array model than are initially present in the experiment, viz. one must account for the increased shielding caused by the early time expansion of coronal plasmas from the wires in the outer array.

If a typical nested array shot is simulated with an annular, snowplow model that accretes mass but holds the current in the outer layers, the current shielding of the target is perfect apart from any resistive diffusion. In contrast, an annular model has no mechanism for anything other than an instantaneous transfer of momentum from the driver to the target at the moment of initial contact, or "first strike". The dissipation of energy required by the conservation of momentum tends to make the annular model's kinematics diverge from that inferred in the experiment.

Beyond first strike the wire dynamic and annular models diverge further. The filamentary WDM generally tends to collect at peak compression in excellent agreement with the observed time of peak radiative power. It also absorbs more than enough energy from the generator to account for the observed radiation yields. The annular picture generally continues to collapse

too fast and show less energy coupling from the generator.

4 Analysis of Nested Array Shots

Modeling a mass scan series of Double Array experiments on "Z" at SNL, we sought to explore variations in compression and energy coupling as the mass ratio of drive and target arrays was changed. Each of the wire loads was modeled in detail with regard to the number and placement of the wires, the wire length and diameter, and the driving voltage waveform. In the WDM the drive array was collected and held fixed once its mass averaged radius was confined to a 1 mm radius; the wire elements were otherwise collisionless. In the annular model the two shells were assigned masses equal to the full drive and target arrays and placed at a 2 cm and 1 cm radius, respectively, and also imploded to a 1mm radius.

4.1 First Strike

Table I. Double Array Shots

Case	1	2	3	4
m_{in}/m_{out}	0.25	1.0	1.3	2.8
Exp. τ_{FS}	-16.5 ns	-26.5 ns	-30.5 ns	-38.0 ns
Exp. Y_{Total}	1.801 MJ	1.528 MJ	1.419 MJ	1.365 MJ
Exp. Y_{FS}	0 kJ	< 60 kJ	< 80 kJ	< 100 kJ
WDM τ_{FS}	-17.0 ns	-26.0 ns	-29.2 ns	-37.5 ns
WDM KE_{max}	1.506 MJ	2.355 MJ	2.358 MJ	2.304 MJ
WDM KE at τ_{FS}	445.5 kJ	398.6 kJ	385.3 kJ	321.7 kJ
Annular τ_{FS}	-18.0 ns	-23.0 ns	-25.5 ns	-31.5 ns
Annular KE_{max}	1.160 MJ	1.090 MJ	1.060 MJ	0.900 MJ
Annular $\mathcal{E}_{rad,FS}$	24 kJ	48 kJ	63 kJ	68kJ

Table I. compares the experimental delay between first strike and peak radiation τ_{FS} to the WDM and annular model's equivalent delay time, viz. the interval between the first array strike and the peak compression. Comparing the time delays, the WDM comes remarkably close to the data, while the

annular model generally shows too quick a rundown. The direct comparison of WDM trajectories and the timings with respect to the radiation pulses is shown in Fig. [5.4(a,b,c,d)]. When the mass ratio is larger so that a well defined XRD pulse is seen at first strike, the lift-off of the inner Compton diode signal is essentially coincident. Hence, for the case of weak or nearly absent first strike XRD signal, the Compton diode lift-off is used to time the first strike.

As the mass weighting changes from the drive to the target array, it is clear that the kinetic energy available at the time of first strike serves to order the observed yields well in the WDM case. The fact that the first strike energies from the WDM should be left in the energy accounting in order to predict the peak yields indicates that energy should not be removed early on by an annular mode collision. The WDM "peak kinetic energy over the whole trajectory", KE_{max} moves through a local maximum for case 3, as does the peak energy drawn from the driver circuit into the load. For case 1 the WDM picture captures the marked increase in available (first strike) kinetic energy at the low mass ratio, in resonance with the observed yield and power enhancement there.

The annular KE_{max} in contrast shows a similar variation to the experimental yields, but this trend is with the first strike energy removed and, as expected from theory [c.f.ref 12], the predicted maximum kinetic energies are *less than the observed yields!* Moreover, the fraction of that first strike energy required to be radiated away in the annular model, $\mathcal{E}_{rad,FS}$, is generally larger than or comparable to the listed upper bound estimate to the observed yield at the first strike. The annular model also shows no enhancement of available energy for mass ratio case 1.

4.2 Interior Array Wire Number Effects

In Fig. [5.5] are shown the soft x-ray XRD traces for a mass ratio case 1 series for target arrays with variable wire number and diameter but fixed mass. Comparing the first strike soft x-ray signature for the cases of 60, 120, and 240 wire target, the first case shows a virtually absent first strike signature while the last shows a clear, rather sharp step in XRD signal at first strike. The second, 120 wire target corresponds to the best yield and power observed in the mass ratio series and the best shot among the case 1

examples. It also shows the weakest first strike radiation, indicating a more complete degree of mass subduction. Geometrically mass subduction is at least four times easier in the low wire number case. In the high wire number target clocking variations between the driver and target might allow the 240 wire driver to slip through, but at least half the driver mass must impinge directly on the location of a cold wire. In the annular limit of two plasma sheets colliding, one and two dimensional MHD calculations generally predict a fairly sharp pulse at first strike, quite different than what is observed and in general agreement with the annular snowplow model used for comparison here.

5 Calibrating the SWDM

As just noted above, in a low wire number target array the opportunity for mass to push through to the interior of the target is much greater than for a high wire number target. In order to quantify the extent to which wire collisions might allow or retard such mass subduction, the situation for Z shot 179 was used as a test bed, as shown in Fig. [5.6a]. The diagram depicts the relative size of the return current, drive array, and target array. A 1 cm grid is included for scale. The mass ratio here was somewhat higher (0.556) than for the first case in the mass scan examined above, but the model dynamics is similar with the drive array pushed well inside the target. The commuted current then implodes the target down on top of the driver and, with no perturbations, the final stagnation radius is well inside the experimental estimate of 0.5 mm.

Here for calibration purposes, the wire positions and properties for drive and target were held fixed, but the value and interaction radius for the sticky drag force were varied. The results are summarized in Table II.

Table II. Transfer Fraction

entry is \mathcal{F}_{tr}	$a_w/2\delta=$ 100	\rightarrow 20	10	5	1
$S_0=10^4$	0.00	0.50	0.50	0.50	1.00
$S_0=10^3$	0.00	0.50	0.50	1.00	1.00
$S_0=10^2$	1.00	1.00	1.00	1.00	1.00

If the drive and target wires line up on one another, then in this case half the target wires will intercept an incoming drive wire, since the drive contained twice as many wires as the target. It is this “clocked” configuration that is used as our baseline here. Clearly as $S_0 \geq 10^3$ there exists a regime where a wide range of wire size provides the same fraction of mass transferred, viz. $\mathcal{F}_{tr} = 0.5$ — the geometrically expected result. As a rough approximation to the expected dynamics, the domain $[S_0 \geq 10^3, 20 > a_w/2\delta > 5]$ defines a sort of “shadow regime”. Imagine the target array to be illuminated from the axis, then, in this domain of size and force parameters, a drive and target wire pair will capture *if the drive wire rests in the “shadow” of the target wire*.

More complex initial conditions will modify the simplistic predictions of such a “shadow” construction. Subtle changes in wire clocking, mass, and radius can admit more or less mass to the interior; however, as shown in Fig. [5.6b], the basic accuracy of the shadow limit is clear. In that figure, a series of variations about the Z shot 179 paradigm shows that a slight interlacing of the wires would allow all of them through. Yet change the drive array with a small mass perturbation and some will be stopped.

The shadow limit has very clear implications for energy transfer as well, c.f. Fig. [5.7]. Here the left scale shows the “total” energy delivered from the “Z” driver compared to the “magnetic” energy for two wire cloud sizes. The right scale shows the kinetic energy accumulated in the whole wire load for the same two cases. Getting the current into the array is virtually independent of wire size, but getting that field energy into kinetic energy is very sensitive to the choices made in the wire’s drag cloud size. In the shadow limit $2\delta \approx 10 a_w$, one finds a smooth interchange from field to flow energy, with a clearly defined signature of first strike as half the drive wires are snagged on a target. If the drag clouds (or interaction length) were larger by tenfold however, the machine’s energy would be mostly left in the magnetic field. The behavior just described is of course *predicted* by the rule of thumb developed in §2.3.

6 The Problem of Filamentation

As known since late 1950s (see [20,21]), a diffuse steady-state is stable with respect to small perturbations with azimuthal wave numbers , so that the

only MHD instability modes are those with $m = 0$ (sausage) and $m = 1$ (kink). In late 1980s, it was noticed by a number of Russian authors, that this conclusion is no longer valid if the pinch plasma is accelerated, and that its hydrodynamic instability was primarily of Rayleigh-Taylor (RT) origin²²⁻²⁵, but not constrained to just axial and radial modes, c.f. Fig. [5.8].

In particular, an imploding Z-pinch is unstable with respect to so-called filamentation instability modes that correspond to the axial wave number $k = 0$ and azimuthal wave number $m \gg 1$. The RT instability might be the most natural explanation of the current filamentation observed in many experiments on plasma focus devices²⁶. This is a strong filamentation instability that acts at the level of one-fluid MHD. Note that before this fact was noticed, people tried to explain the observed filamentation in plasma focus experiments by weaker two fluid²⁷ or dissipative²⁸ effects.

It is natural to expect the filamentation instability to develop in imploding wire arrays, where initially the filamentation mode with $k = 0, m = N_{wires}$ undoubtedly has the largest amplitude. The growth rate of this mode was estimated²⁹ on the basis of the ideal MHD model. Applying the Lagrangian perturbation analysis, traditional for laser fusion-related studies³⁰ to self-similar MHD implosion of an annular Z-pinch shell, the authors found a simple expression:

$$\Gamma = \sqrt{\sqrt{2} - 1} \cdot \sqrt{g k_{eff}},$$

for the fastest RT filamentation mode growth rate —localized at the inner surface of the imploding shell in the short-wavelength limit ($m \gg 1$). Here g is the acceleration, and $k_{eff} = m/R$ is the effective wave number [cm^{-1}]. The same relation in this limit was first obtained by E. G. Harris who used a thin-shell model³¹. The factor 0.644, which is smaller than (but of order) unity is due to the fact that filamentation perturbations bend magnetic field lines, which requires additional energy, and hence, slows down the perturbation growth. For the same reasons, the fastest growing filamentation perturbations tend to localize near the inner surface of the imploding shell, to minimize the energy expenditure on bending of magnetic field lines. However, since for an imploding multi-wire array the initial amplitude of at least one high-order filamentation mode, $m = N_{wires}$, is much larger than the amplitude of any other perturbation of comparable wavelength, we can expect this to compensate for a relatively small difference in exponential growth

rates. Consequently, at early time the development of the RT filamentation mode could be dominant, or, at least, significant.

Thus, filamentation is an x-y counterpart to the Rayleigh Taylor mode in r-z and it grows at *similar* rates in an accelerated pinch. The wire model will mimic this filamentation process by accreting clumps of wires during the rundown if an azimuthal force imbalance arises. The well-known progression of the RT instability to lower wavenumber in the non-linear phase implies that, in the transverse (xy) plane, such clumps are energetically favorable. Hence, in the context of our SWDM, one might expect perturbations in mass and radius to excite lower azimuthal wavenumbers as the wire load runs down to the axis or to the target array.

We compare (in Fig. [5.9a]) three cases: no perturbation, a 10 % mass perturbation (ΔM), and an added 10 % radius perturbation (ΔR & ΔM). By the time of first strike in a Z-179 scenario a clear filamentation mode is seeded by the perturbation, but is absent without it. Moreover, while the mode seed is at the symmetry group wavenumber ($\pi/6$), the dynamics chooses a slightly higher mode ($\pi/12$) to cascade down to from the original ($\pi/120$) mode of the individual wires. Circled on the figure (at about 4 o'clock in each array image) are regions where shadow limit particles have been recolored to indicate collision, even before the wire arrays hit.

We have begun a study of azimuthal modulation before stagnation due to initial array mass and position variations [" ΔM ", " ΔR "] to see how filamentation can be quantified and how it changes the subduction of mass in nested arrays. One requirement for such comparisons is a quantitative diagnostic of the filamentation process based upon the wire dynamics during an implosion. Similar to RT calculations in the r-z plane, what we find is that an inventory of the kinetic energy orthogonal to the implosion direction, viz. $e_\theta = \sum_i m_i v_{\theta,i}^2 / 2$, is a good indicator of the time and amplitude of filamentation. An example is shown in Fig. [5.9b] for the case of a pure mass perturbation. Like the earlier illustration on energy transfer (Fig. [5.7]), the machine input energy and total magnetic energy are shown on the left scale; while, on the right, are the various components of drive (D) and target (T) kinetic energy. The full kinetic energy traces [$e_{k,T}$, $e_{k,D}$, e] show the general timing and relative strength of the kinetic energy as it interchanges between the drive and the target. The magnified traces [$e_{\theta,T}$, $e_{\theta,D}$] show pulses of azimuthal action corresponding to three clumping events in the drive wires and one in the target wires. The last surge of filamentation being just before

stagnation in drive and target. Ongoing work seeks to correlate these energy surges with measures of the filamentation amplitude.

7 Conclusions

An accurate picture of the observed kinematics of a nested array load is outside the scope of common r - z 0D, 1D and 2D codes, requiring techniques that (i) capture the subduction of driver mass to the target's interior, (ii) calculate the proper inductive current partition and current commutation, and (iii) account for the time delay for boosting the target array to speed. A collision model based on two annular layers will predict that the load implodes too quickly with respect to the experiments. The annular collision mode also tends to deliver too little energy to the load to match the observed radiative yields from the nested array loads. In contrast, puff-on-puff experiments, which cannot show any mass subduction, do follow the yield trends in mass ratio expected from an annular collision model.

Control of target density through wire number to allow more mass subduction provides a means to enhance the radiation power from a nested array. The performance at low mass ratio (case 1) shows that mass subduction was a factor and that more complete subduction tended to produce the best yields and powers. When mass subduction is obtained, the early accumulation of the driver mass near the axis has two useful properties—it provides a stagnation point, and forces the current to be commuted to the target mass.

The mass subduction apparent in the experiments can be captured by the SWDM with a fair level of accuracy once the drag model is calibrated. We have shown a well defined "shadow" regime for the model wherein the dynamics is not strongly dependent on the strength of the drag force or the size of the drag region—allowing physically grounded models of the wire diameter to be developed and tested on their own merits. Evolution of filamentation modes can be captured by the model and at least one means of quantifying their influence has been identified.

We wish to acknowledge useful discussions with M.R. Douglas, R.B. Spielman and K.W. Struve of SNL. This work was sponsored by Defense Threat Reduction Agency.

References

1. N. R. Pereira and J. Davis, J. Appl. Phys. 64 R 1 (1988).
2. T.W.L. Sanford et al, Phys Rev Lett 77, 5063, (1996).
3. C. Deeney et al, Phys. Rev. E 56(5-B), 5945, (1997).
4. R. B. Spielman et al, Phys. Plasmas 5(5), 2105, (1998).
5. T.-F. Chang, A. Fisher, and A. Van Drie, J. Appl. Phys. 69, 3447 (1991).
6. R. B. Baksht, A. V. Luchinsky, and A. V. Fedyunin, Sov. Phys. - Tech. Phys. 37, 1118 (1992).
7. R. B. Spielman, T. Nash, and M. Krishnan, Bull. Am. Phys. Soc. 37, 1578 (1992).
8. R. B. Baksht, Bull. Am. Phys. Soc. 40, 1852 (1995).
9. R. B. Baksht, I. M. Datsko, A. A. Kim, A. Yu. Labetsky, S. V. Loginov, V. I. Oreshkin, A. G. Roussikh, A. V. Fedyunin, and A. V. Shishlov, Plasma Physics Reports 21, 907 (1995).
10. T. W. L. Sanford, D. Mosher, J. S. DeGroot, J. H. Hammer, B. M. Marder, S. Maxon, T. J. Nash, R. B. Spielman, P. T. Springer, K. Struve, R. S. Thoe, D. R. Welch, W. E. Alley, C. Bruns, J. D. Eddleman, J. Emig, T. L. Gilliland, J. Hernandez, D. Jobe, J. S. McGrun, R. C. Mock, J. F. Seaman, M. Vargas, and G. B. Zimmerman, "X-ray emission from a high-atomic-number z-pinch plasma created from compact wire arrays," Sandia report SAND96-0222, March 1996. Copies may be ordered from the NTIS, Springfield, VA 22161.
11. C. Deeney et al, "The enhancement of x-ray powers from a z-pinch using nested wire arrays", accepted for Phys. Rev. Lett., (1998).
12. M.R. Douglas, et al, "Computational modeling of tungsten Z-pinchs with tuning layers" accepted for Phys Rev E.
13. J. Davis, N.A. Gondarenko, and A. L. Velikovich, Appl. Phys. Lett., v. 70, p. 170 (1997).
14. R. B. Baksht, private communication
15. F. S. Felber and N. Rostoker, Phys. Fluids 24, 1049 (1981).
16. See National Technical Information Service Document No. PB95-144317 (D. Mosher, "Plasma radiation source implosion limits due to azimuthal asymmetries," in Proc. of the 10th Int. Conf. on High Power Particle Beams, 20-24 June 1994, San Diego, CA, p. 159). Copies may be ordered from the NTIS, Springfield, VA 22161.
17. A. A. Samokhin, Prikl. Mat. Tekh. Fiz., no. 2, 89 (1988).
18. F. N. Beg, J. Ruiz, A. E. Dangor, Dense Z-Pinchs, AIP Conf Proc 409, 1997
19. S. V. Lebedev, et. al., private communication.

20. B. B. Kadomtsev, in *Reviews of Plasma Physics*, ed. by M. A. Leontovich (Consultants Bureau, New York, 1966), Vol. 2, p. 153.
21. J. P. Freidberg, *Rev. Mod. Phys.* 54, 801 (1982).
22. A. B. Bud'ko, A. L. Velikovich, A. I. Kleev, M. A. Liberman and F. S. Felber, *Sov. Tech. Phys. Lett.* 14, 817 (1988).
23. S. V. Bulanov, *Sov. Phys. - Lebedev Institute Reports*, issue 2, p. 12 (1988).
24. A. B. Bud'ko, A. L. Velikovich, A. I. Kleev, M. A. Liberman, and F. S. Felber, *Sov. Phys. JETP* 68, 279 (1989).
25. A. B. Bud'ko, F. S. Felber, A. I. Kleev, M. A. Liberman, and A. L. Velikovich, *Phys. Fluids B* 1, 598 (1989).
26. N. V. Filippov, *JETP Lett.* 31, 120 (1980); V. Nardi, W. H. Bostick, J. Feugeas, and W. Prior, *Phys. Rev. Lett. A* 22, 2211 (1980); M. Sadowski, H. Schmidt, and H. Herold, *Phys. Rev. Lett. A* 105, 117 (1984); H. Herold, A. Jevzykiewicz, M. Sadowski, and H. Schmidt, *Nucl. Fusion* 29, 1255 (1989).
27. H. J. Kaeppler, in *Plasma Focus and Z-Pinch Research*, Proc. of 5th Int. Workshop, Toledo, 1987 (Imperial College, London, 1987), p. 59; B. E. Meyerovich, *J. Plasma Phys.* 29, 361 (1983).
28. V. S. Imshennik and S. V. Neudachin, *Sov. J. Plasma Phys.* 13, 703 (1987); *ibid*, 14, 393 (1988).
29. A. I. Kleev and A. L. Velikovich, *Plasma Phys. Contr. Fusion* 32, 763 (1990).
30. R. Kidder, *Nucl. Fusion* 16, 3 (1976); D. L. Book and I. B. Bernstein, *Phys. Fluids* 22, 79 (1979); *J. Plasma Phys.* 23, 521 (1980); S. J. Han and B. R. Suydam, *Phys. Rev. A* 64, 3831 (1982).
31. E. G. Harris, *Phys. Fluids* 5, 1057 (1961).

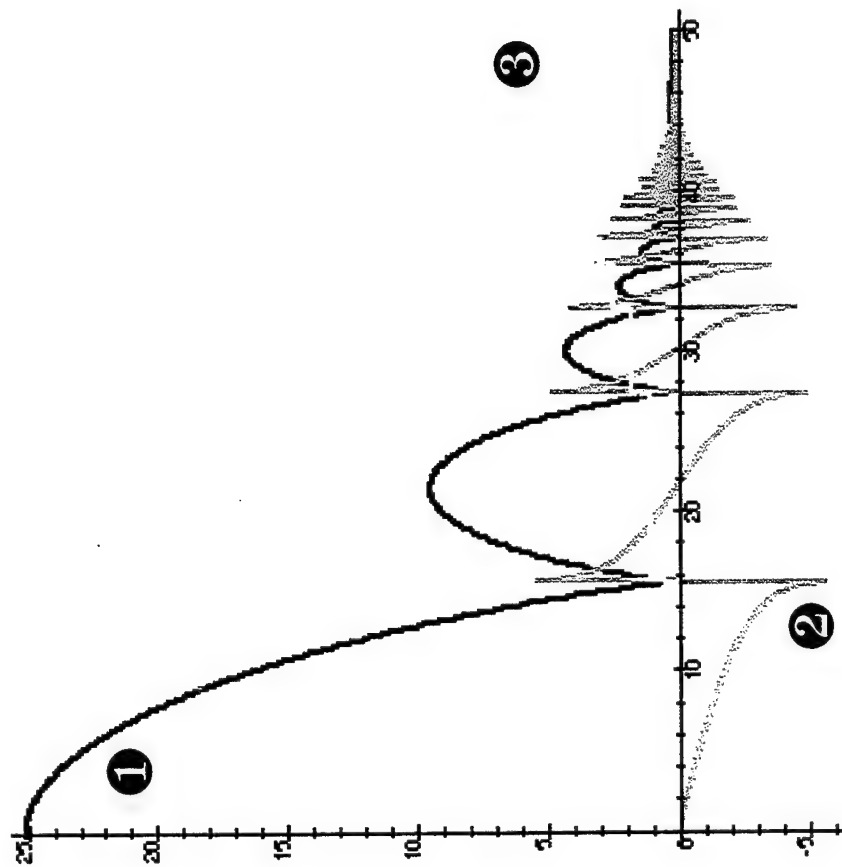


Fig. 5.1 Radial trajectory [1], velocity [2], and dissipated energy [3] for a two wire system with relative angular momentum 0.1 and a viscous drag localized to a radius $1/20$ of the initial separation in the CM Frame. The final energy dissipated is a weakly varying fraction [0.451 ... 0.474] of the change in potential energy during the collision.

Fig. 5.2 Dissipated Energy with Angular Momentum

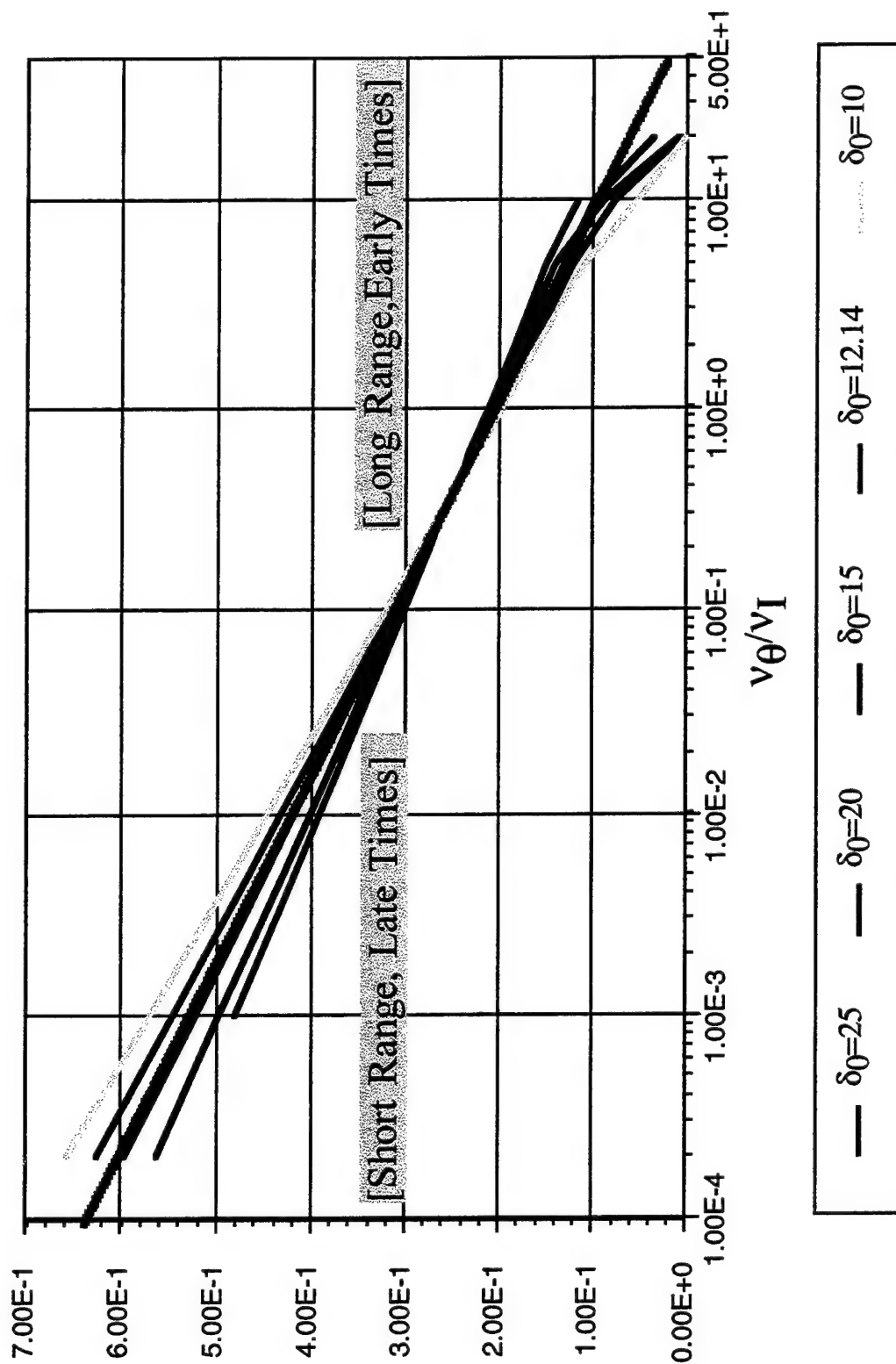
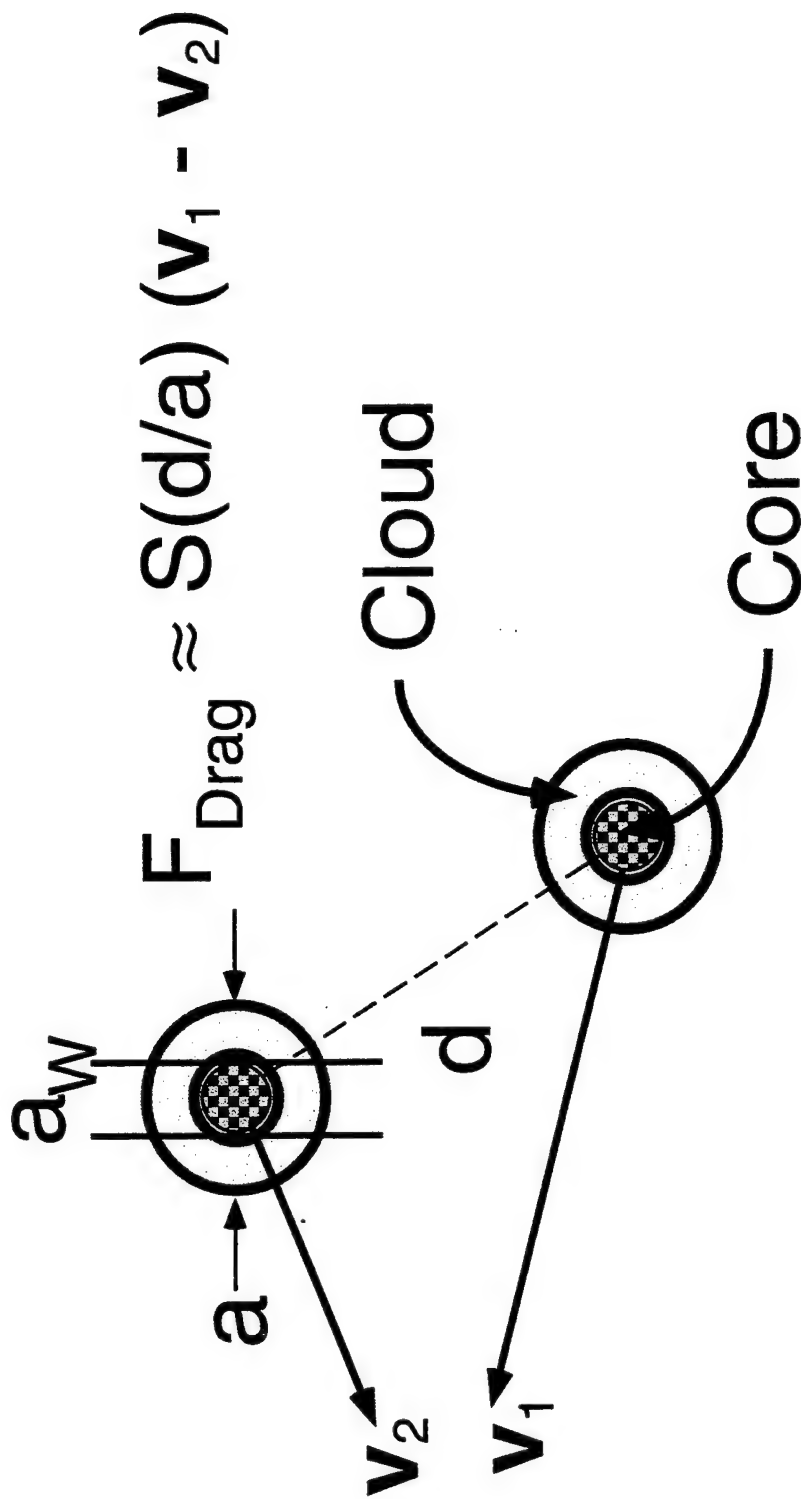


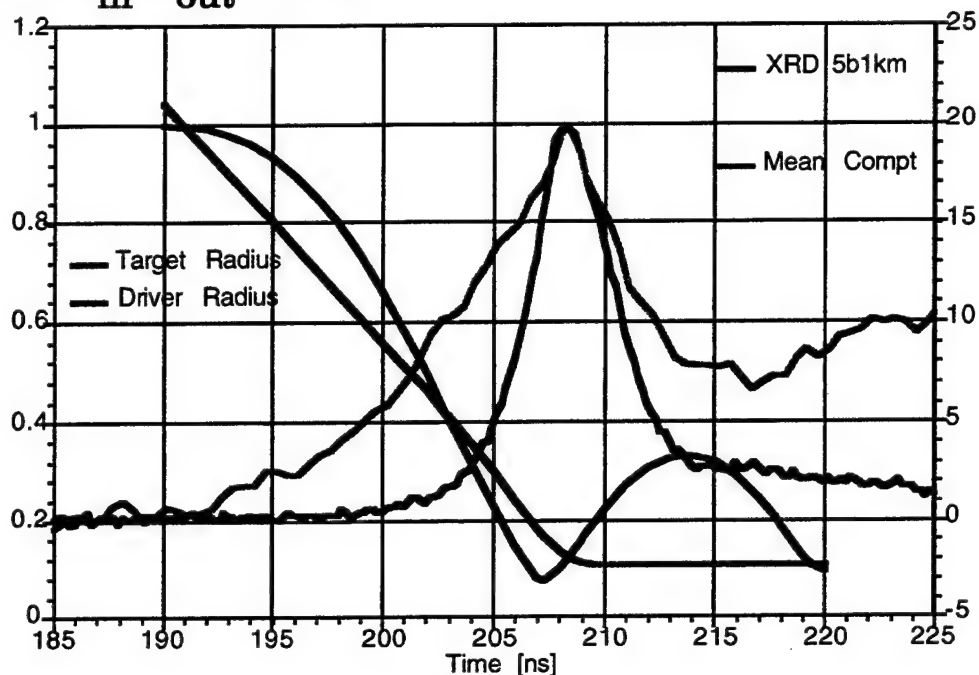
Fig. 5.3 "sticky wire" Drag Force Model



Wire cores hold current and show the usual Biot-Savart dynamics; clouds must overlap to turn on the drag force smoothly.

Fig. 5.4(a,b) Comparison of WDM and experimental radiation signatures for cases 1 and 2.

Case 1: $m_{in}/m_{out} = 0.25$



Case 2: $m_{in}/m_{out} = 1.0$

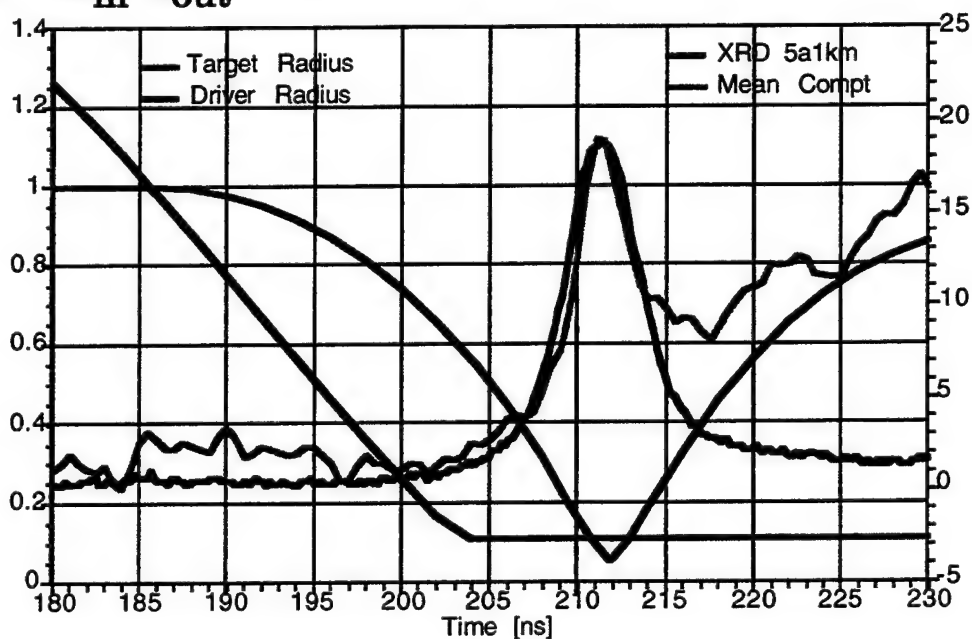
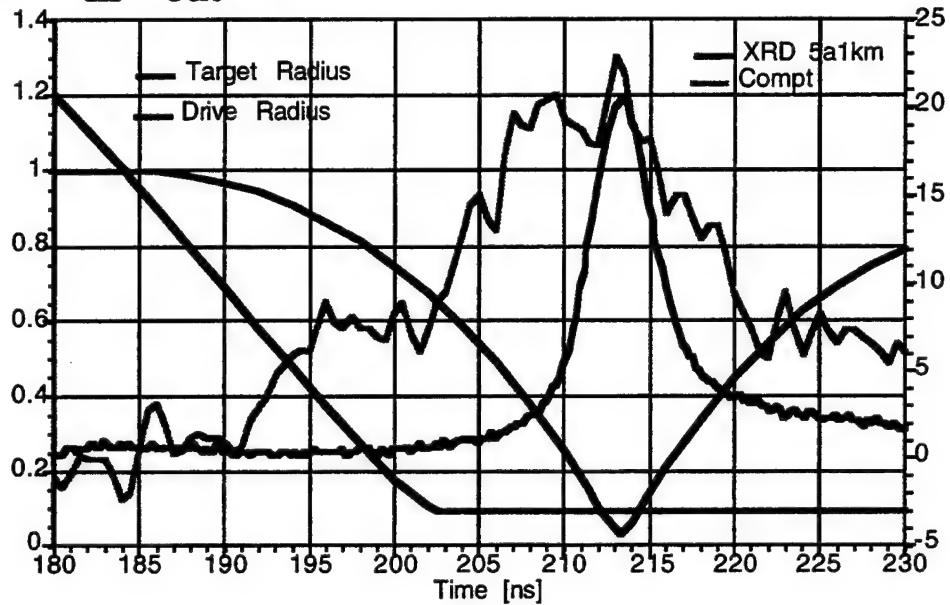
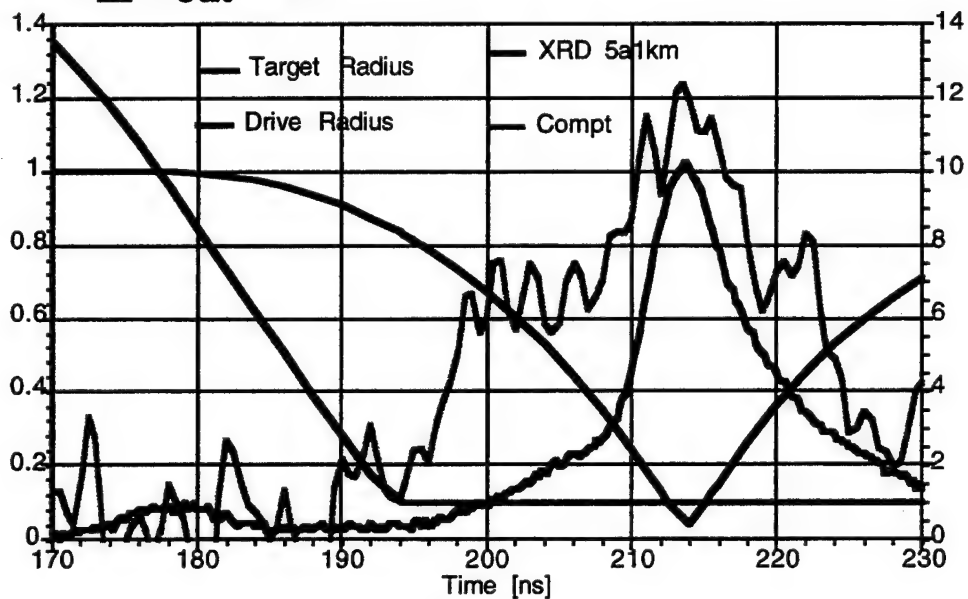


Fig. 5.4(c,d) Comparison of WDM and experimental radiation signatures for cases 3 and 4.

Case 3: $m_{in}/m_{out} = 1.3$



Case 4: $m_{in}/m_{out} = 2.8$



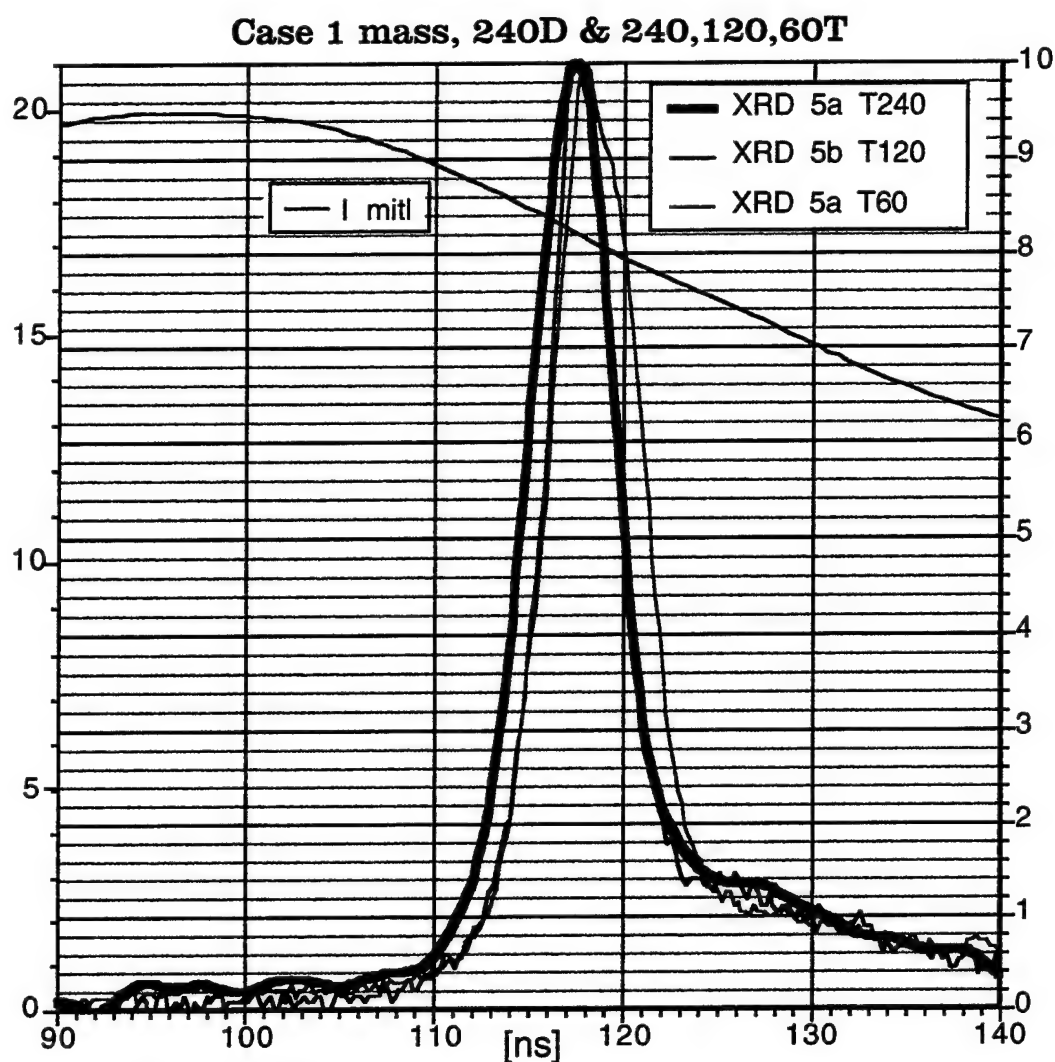


Fig. 5.5 Comparison of experimental radiation signatures for varying wire number in the Target array. The resolution of a more annular first strike in the T240 case is clearly seen.

Fig. 5.6a Common initial state for the study

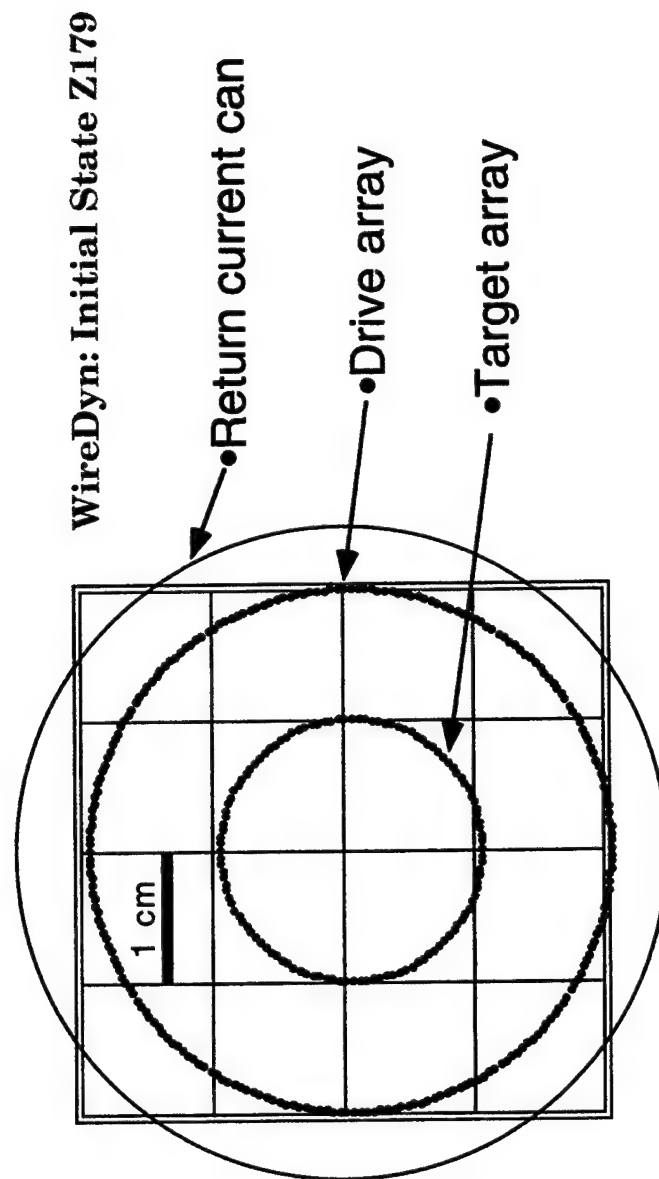


Fig. 5.6b Shadow Regime Mass Transfer Dependence on "Clocking"

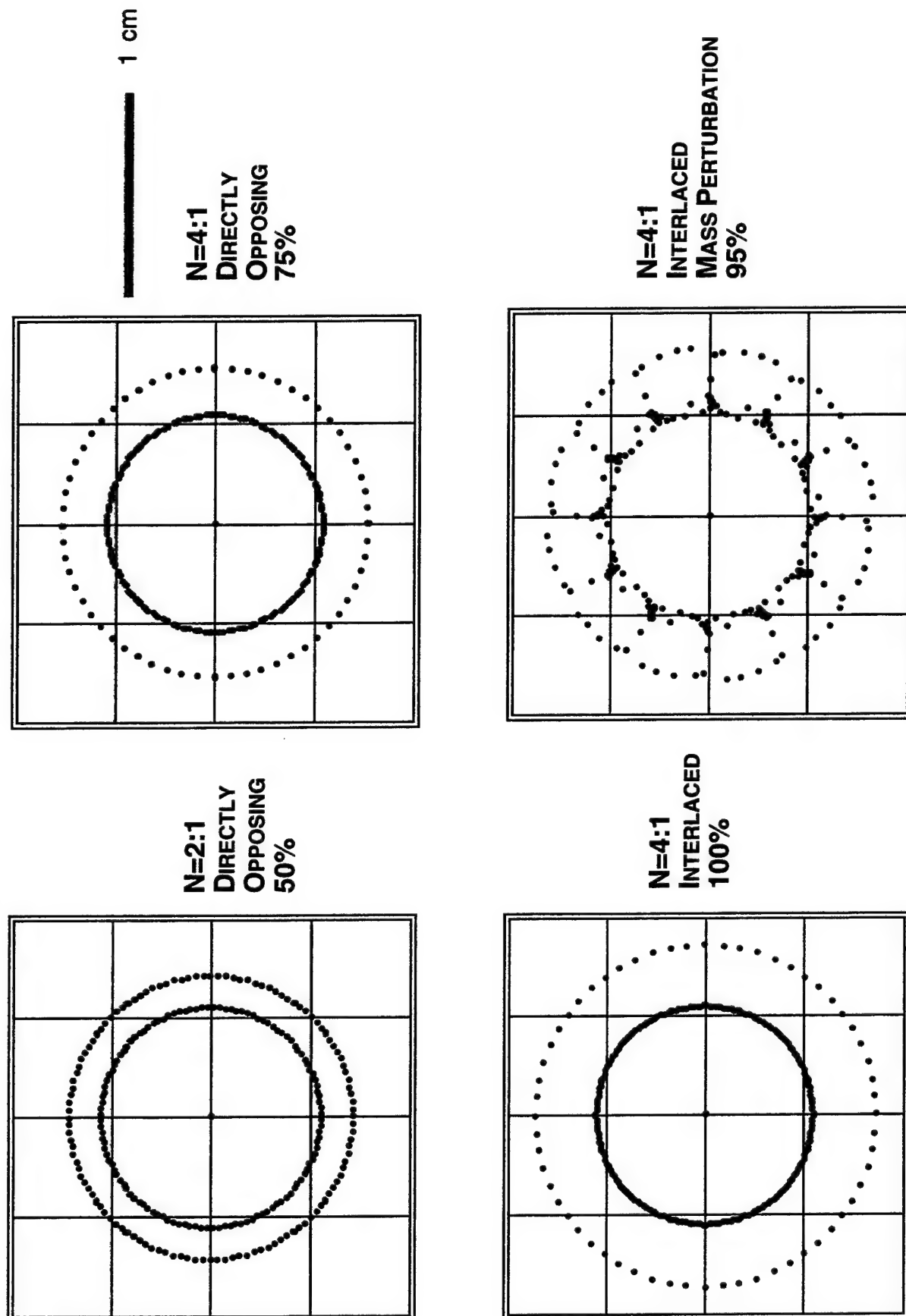


Fig. 5.7 Kinetic Energy Transfer Depends on "Drag Zone" Size

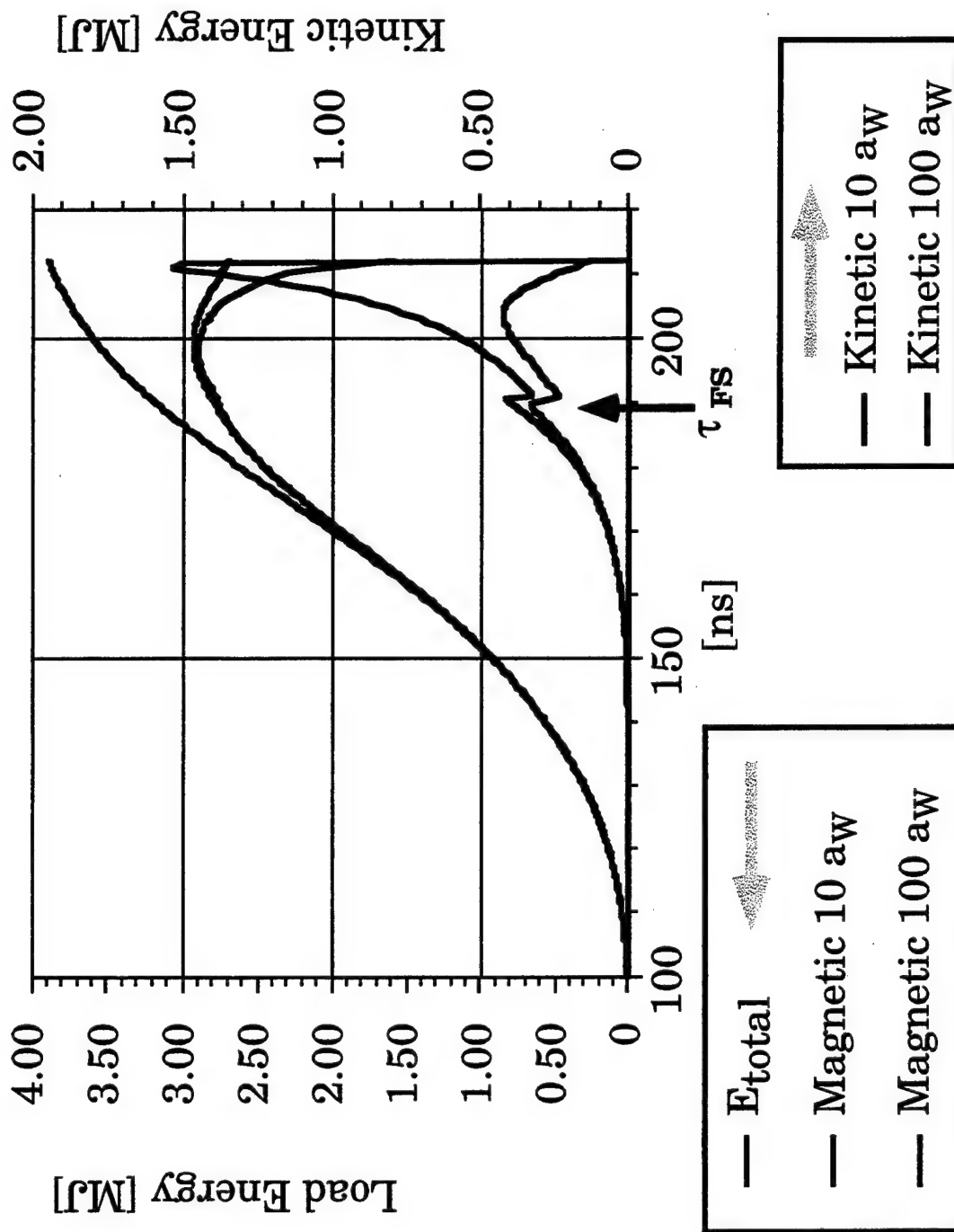


Fig. 5.8 Normalized Growth Rates for an Accelerated Pinch

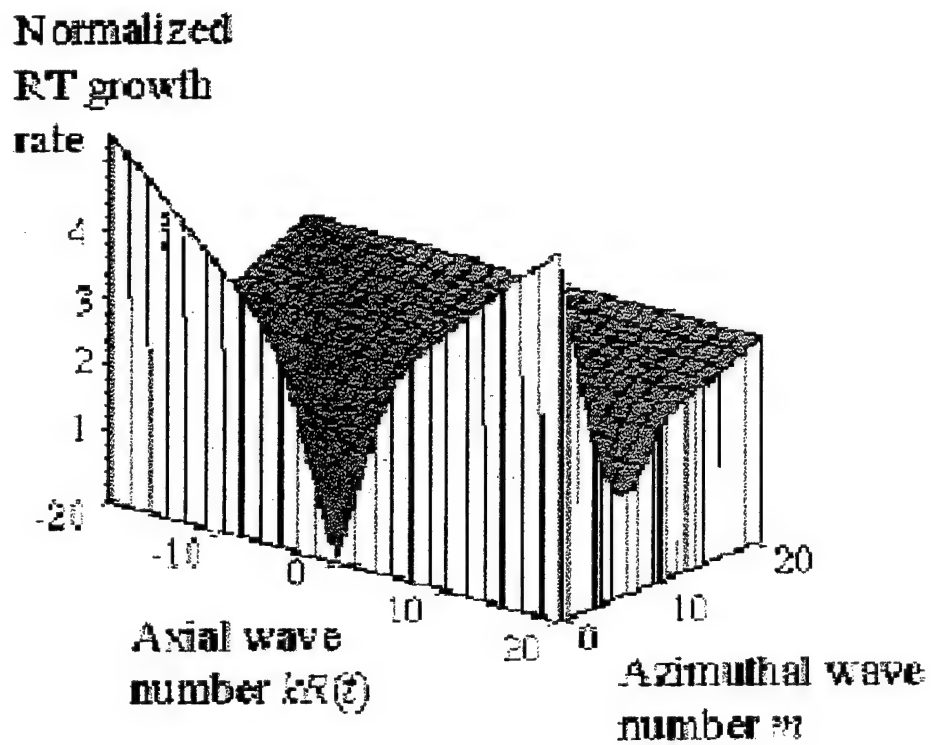


Fig. 5.9a Filamentation Examples at First Strike

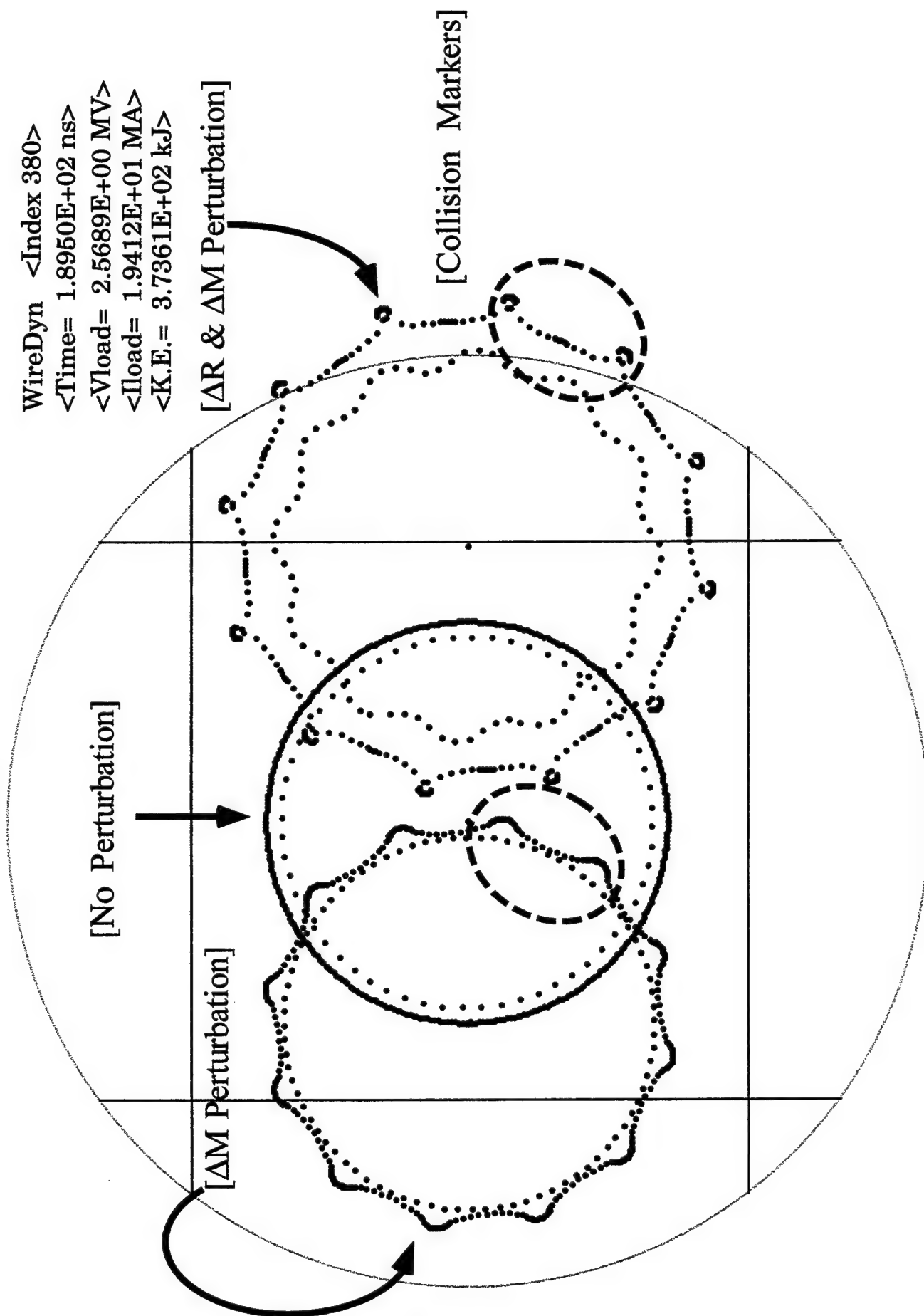
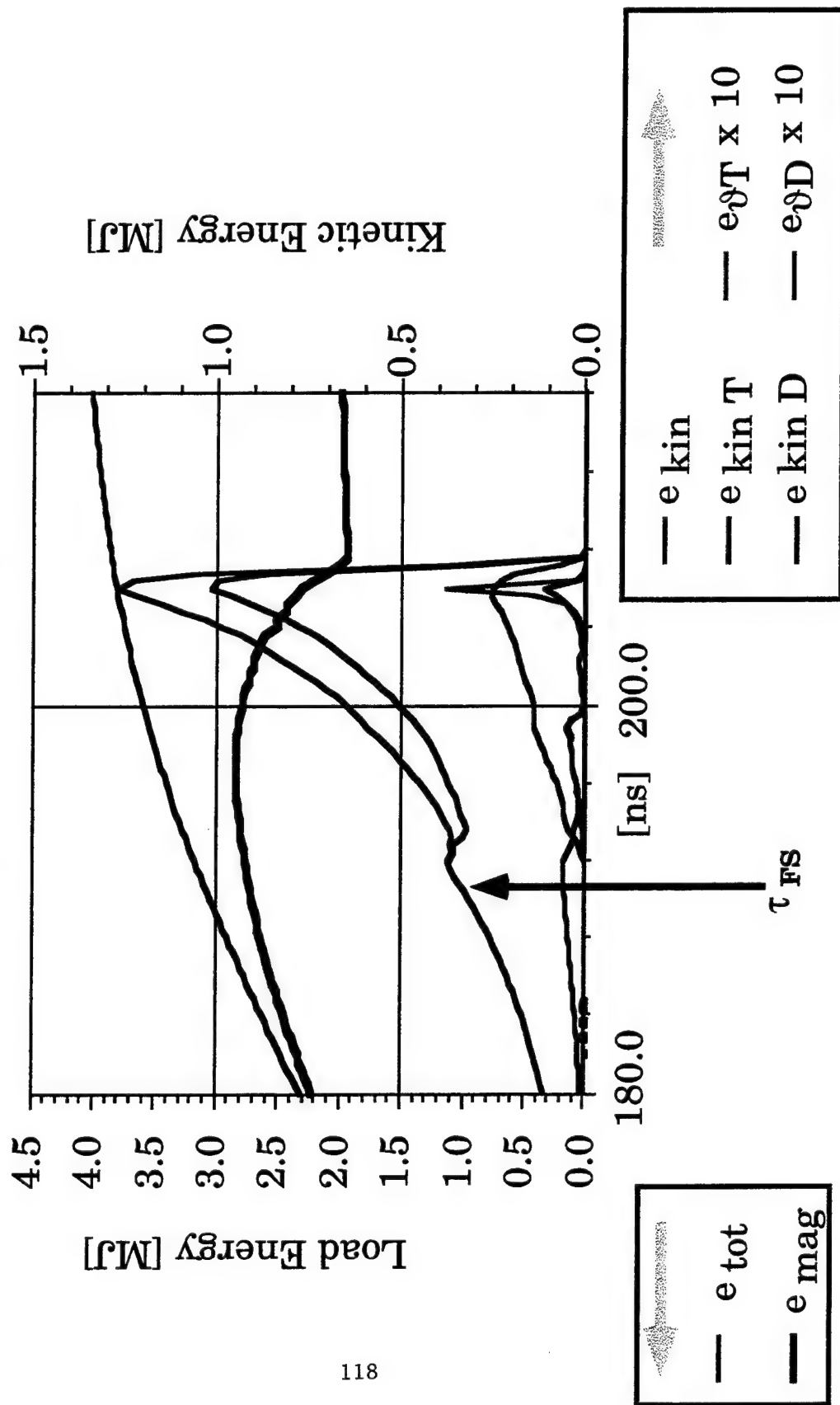


Fig. 5.9b Diagnostics of Filamentation

$$e_{\vartheta} = \sum_i 1/2 m_i v_{i\vartheta}^2$$

[ΔM Perturbation only]



VI. Two-Dimensional Simulations

(a) Two-Dimensional Code Development

In the past year, we enhanced our two-dimensional (2D) code, PRISM, with the inclusion of radiation diffusion. Previously, we had been using a "local approximation" scheme where the transport was only accounted for within each zone and the remainder of the plasma was assumed to be thin to that zone. While not perfect, the diffusion model does allow dense radiating regions of the 2D mesh to exchange energy. This method works well in both the LTE limit and in the thin limit but has problems in the regime between these two extremes. It is also commonly used in "three temperature" codes where the radiation energy is treated like a third temperature in a diffusion equation and then coupled to the electrons through an energy exchange term.

In our approach, we do not advance a third or, radiation, temperature, T_r , but instead use the Code 6720 atomic physics tables to determine the radiation energy density in each zone. This quantity is then transported within the diffusion approximation. In the LTE limit, this gives the same result as is obtained when using a third temperature and diffusing, σT_r^4 . In the thin limit, the diffusion length is larger than the computational region of interest. The result is equivalent to calculating the radiation power in each cell and allowing the energy integrated over a time cycle to completely leave the plasma. A flux limiting term is used to help bridge the gap between these two extremes. We have used the flux limiting method specified by Pomeraning¹. The opacities used to determine the diffusion length are generated from the SESAME tables at the Los Alamos National Laboratory.

The calculational sequence for transporting the radiation energy, as well as the ion and electron internal energies, in the 2D code proceeds as follows: (1) From the internal electron energy and density, equation of state values are calculated. These include ionic charge, Z , electron temperature, radiation power (the analogue to σT_r^4 in three temperature codes), and Roseland and Planck opacities. (2) The electron, ion, and radiation components are each transported over a half-timestep and are used to calculate new time centered transport coefficients on the half-timestep.

(3) The original quantities calculated in step (1) are then transported over a full-timestep. (3) In the case of the radiation energy, the amount which escapes the computational region (this depends on the boundary conditions) is calculated and included in the total radiated energy calculations. The remaining radiation energy, which can be greater than the original energy in the case of absorption, is used to increase or decrease the electron energy. This is in contrast to a thin calculation where the electron energy is always decreased due to the loss of the entire amount of the radiated energy.

We also moved the 2D code, PRISM, from the Cray YMP at LANL to the 32 processor SGI/Cray Origin 2000 (machine theta) at LANL. This required some code conversion but the first attempt at moving the code proved much easier than anticipated. With some minor tuning and making use of the facility for automatic parallel code generation, PRISM can now be run in production mode at higher speeds than are typically achieved on the YMP.

(b) Two-Dimensional Simulations For Double Eagle In Long Pulse Mode

During this past year we used the 2D code, PRISM, to run long current pulse simulations of Double Eagle. In the long pulse mode, the Double Eagle current rises to roughly 4 MA in about 200 ns and mimics the rise of the Decade current pulse. The version of the code used for these simulations incorporated the radiation diffusion transport scheme rather than a "thin" or "local" approximation. This transport method is detailed in the previous section.

All of the simulations assumed an Argon uniform fill load. The simulation region extended over an axial length of 1 cm and no provisions were made for expansion of the gas after exiting the throat of the nozzle. That is, the plasma column is modeled as a straight annulus. The initial radius of the gas fill was taken to be 4 cm with the load inductance based on a total column length of 4 cm and a return current radius of 7.5 cm. The current was determined self-consistently from a polynomial fit to the long pulse voltage waveform. The simulations were run with three initial mass loadings (150 $\mu\text{gm}/\text{cm}$, 200 $\mu\text{gm}/\text{cm}$, and 250 $\mu\text{gm}/\text{cm}$). A density perturbation was applied to the load mass after the back edge of the shell has started to accelerate inward but well before final implosion. Different magnitudes of the perturbation level were used with a single mode wavelength of 3 mm.

The calculated K-shell yields are shown in Fig. 1. The best yield was produced by the 250 $\mu\text{gm}/\text{cm}$ load with the smallest perturbation. Although not shown in the figure, additional simulations showed that there was a falloff in K-shell yield with larger masses. It can be seen that the yield falls dramatically as the perturbation level is increased. This is an indication that there is a breakup of the plasma column which becomes more severe with increasing perturbation level. In Fig. 2, two density contour plots at 242 ns are shown for the 250 $\mu\text{gm}/\text{cm}$ load and different initial density perturbation levels. The classic R-T (Rayleigh-Taylor) instability bubble and spike can be seen in both cases. In the larger perturbation case, however, very elongated spikes have developed. If this was a shell load rather than a uniform fill, the shell would be close to breaking apart at this time. The accretion of

mass into the bubble and subsequently out into the spike region prevents this from happening. In the smaller perturbation case, the bubbles and spikes are not nearly as pronounced at this time. The accretion shell is also relatively broad compared to that of the second case. The result is that the radiating region will tend to be broader and more uniform rather than highly localized or made up of "spots". Any technique which can reduce the initial perturbation may have a significant effect on the final implosion state. These might include pre-ionization in the case of gas fill loads or a large number of wires in wire-array loads. The best yield between 5 kJ/cm and 6 kJ/cm would correspond to about 20 kJ over a 4 cm length.

Additional simulations of these loads and double shell loads were in progress at the end of this fiscal year. The results from these studies were scheduled to be presented at the DTRA PRS Workshop in December 1998 and will be included in next year's (FY 1999) final report.

References

1. G. Pomeraning, JQRST 27, 517(1982).

Figure Captions

1. Yield as a function of mass perturbation level (percent) for several mass loadings are shown.
2. Density contours just prior (242 ns) to final implosion for the 250 $\mu\text{gm}/\text{cm}$ load. The 5 percent and 10 percent mass perturbation cases are shown.

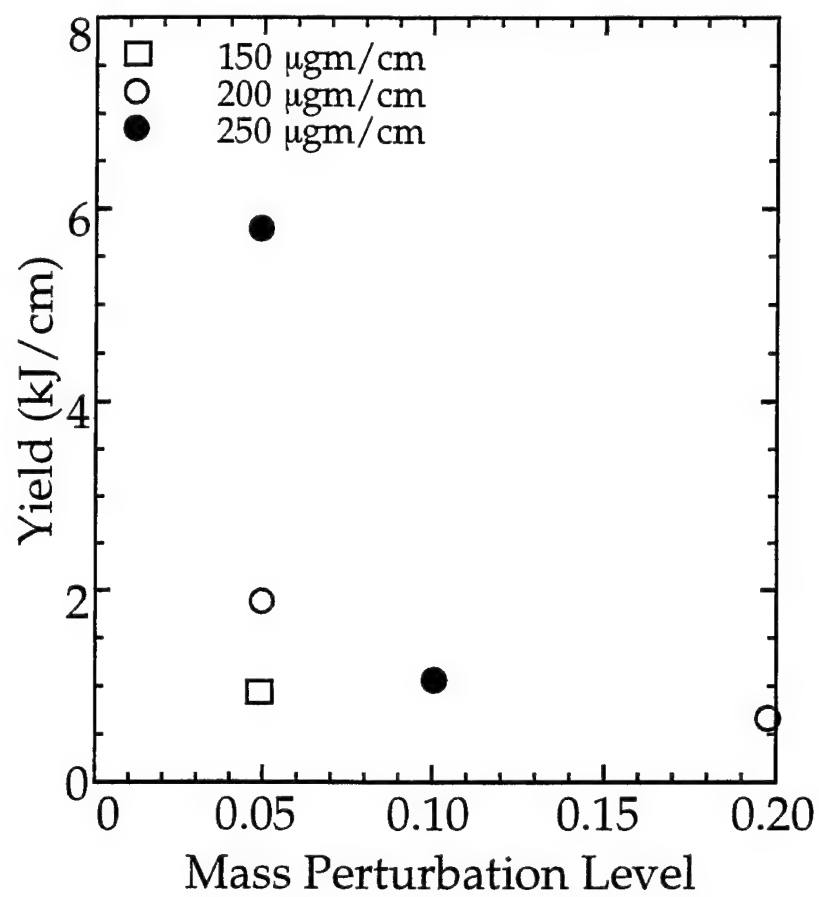


Figure 1

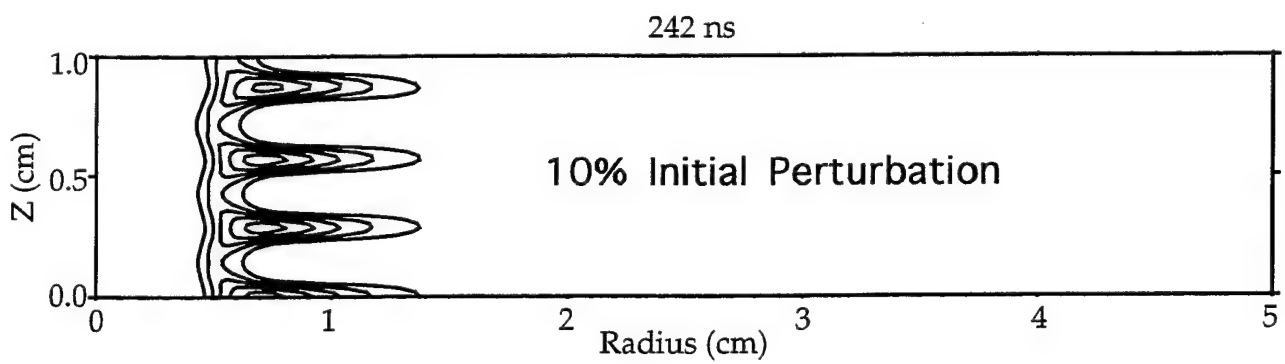
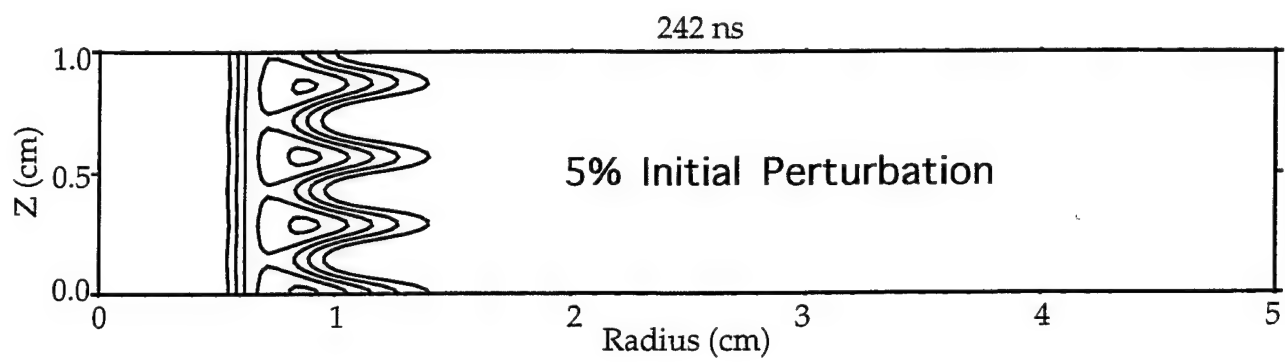


Figure 2

VII. D-T Fusion in 40 and 60 MA Z-Pinches

ABSTRACT

With the Sandia "Z" facility operational and the expectation of even larger Z-pinch devices in the concept and design phases, there is renewed interest in exploring the feasibility of creating conditions conducive to nuclear fusion in a pulsed Z-pinch. Experiments have been performed with a D-D plasma on Sandia's Saturn facility, producing up to 3×10^{12} D-D neutrons from a near-Maxwellian plasma. For peak currents in excess of 20 MA, the magnetic field may be sufficient to confine the α -particles. Even in the absence of breakeven, substantial increases may be obtained in radiative yield and photon energy.

1. INTRODUCTION

Over the last two decades, considerable attention has been devoted to Tokamak-style magnetic confinement nuclear fusion. Indeed, most of the national fusion budget was expended in the construction and operation of these very large devices. Now, the National Ignition Facility is under the microscope, and promises to consume a sizable fraction of the funding for fusion research. The recent successes with large Z-pinch devices such as the Saturn and "Z" facilities at Sandia National Laboratory have renewed interest in Z-pinch fusion. Before any resources are committed to Z-pinch fusion devices, some very basic questions need to be addressed. Can substantial thermonuclear burn be expected in such devices? Will the energy produced in the α -particles be confined in the plasma, or will they escape? If magnetic confinement of the α -particles is possible, how big do the fields (and currents) have to be? Is breakeven necessary, or can the additional fusion energy provide enhanced Plasma Radiation Source (PRS) output? We have arrived at several conclusions (which will be discussed below): (1) A quasi-steady radiative-collapse Z-pinch scheme will not work; it would be worthwhile to complement the extensive indirect Z-pinch fusion studies with an investigation of the dynamic "direct-drive" option. (2) Conditions for fusion may be satisfied for peak currents exceeding 30 MA. (3) Low-Z Bremsstrahlung radiation (characteristic of fusion plasmas) may be an alternative to high-Z K-shell radiation for PRS applications. (4) Early-time stabilization, mid-implosion transfer of kinetic energy and current to an inner mass shell and, ultimately, super-compression

(exceeding the Bennett equilibrium conditions) in the final stage is a promising path to Z-pinch fusion.

- **Indirect-drive and radiative-collapse:** The indirect drive scheme requires conversion of the pinch energy into hohlraum radiation, only a small fraction of which ($\sim 15\%$) is actually incident on the compressed pellet. As in laser fusion, it would be natural to seek increased energy efficiency (and hence, increased gain) by investigating the direct-drive option, where the energy is directly deposited into a Z-pinch driven D-T plasma. A quasi-steady radiative collapse fusion scheme, on the other hand, being the most simple and best-studied example of the direct-drive approach, requires an unrealistically high radial compression. For cylindrical symmetry and Bennett equilibrium, the Lawson criterion requires that

$$\rho R = \frac{M}{2c} \left(\frac{n_0}{\pi} \right)^{1/2} \frac{I}{T^{1/2}} = 6.5 \times 10^{-4} \frac{I(\text{MA})}{T(\text{keV})^{1/2}} \frac{R_0}{R}$$

which requires $R/R_0 > 120$ and ion densities of order 10^{27} to achieve $\rho R > 1$ for $I = 40 \text{ MA}$ and $T_i = 10 \text{ keV}$. However, these requirements are relaxed if the α -particles can be magnetically confined. In this case, ion densities of 10^{24} and confinement times of 1 ns might be sufficient.

- **Peak current must exceed 30 MA:** Conditions for fusion require peak currents exceeding 30 MA for the following reasons: (a) The magnetic field produced by a 20 MA current may be sufficient to contain the α -particles, and (b) a 30 MA current is sufficient for the inertial confinement of a complex load. Simple estimates of α -particle confinement give

$$I \geq \frac{v_\alpha m_\alpha c^2}{4e\delta} = \frac{1.35 \text{ MA}}{\delta},$$

where δ is a factor which is (using Tokamak theory) approximately 0.0674, and v_α and m_α are the α -particle velocity and mass. Then $I \geq 20 \text{ MA}$. Furthermore, as described in Gol'berg *et al.*¹, inertial plasma confinement can be achieved in a complex load (where the D-T inner plasma shell is first compressed and then contained by an outer shell of larger mass). For this case, the Lawson criterion reduces to

$$I > c(6\sqrt{2}\pi L)^{1/2} \frac{T^{3/4}}{M^{1/4}} \frac{R_0^{1/2}}{k^{1/4}(N \log N)^{1/2}}$$

where $N = R_0/R$ is the compression ratio, $L = n\tau$ is the Lawson number, and $k = M_{\text{outer}}/M_{\text{DT}}$ is the mass ratio. For $T = 10 \text{ keV}$, $R_0 = 1.0 \text{ cm}$, $N = 30 - 40$, and $k = 4$ we

obtain $I = 30 - 40 \text{ MA}$. These parameters should not be impossible to achieve; e.g., fortyfold compressions have been reported in recent experiments with nested wire arrays at SNL².

• **Low-Z Bremsstrahlung radiation:** As the requirement for x-ray radiation progresses to shorter wavelengths, higher atomic number radiators are required. Conditions required for efficient x-ray production become inconvenient at higher atomic numbers. First, the electron-ion equilibration time is proportional to atomic weight, and at sufficiently high Z , the electrons cannot heat rapidly enough. Second, with high- Z ions, there are too many energy sinks; thermal energy is efficiently radiated away in L- or M-shell radiation, and the K-shell emission is correspondingly reduced. However, low- Z Bremsstrahlung does not have these difficulties. It does have the problem of being inefficient compared with line radiation. Requiring that a substantial part of the thermal energy be radiated away, we can write $P_r^{Brems} \tau \geq \frac{3}{2}(1+Z)nT$, where P_r^{Brems} is the Bremsstrahlung power:

$$P_r^{Brems} = \frac{16}{3} \left(\frac{2\pi}{3} \right)^{1/2} \frac{e^6 Z^3 n^2 T^{1/2}}{m_e^{3/2} c^3 \hbar}$$


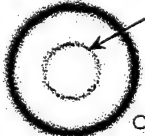
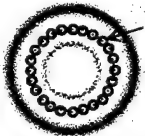
and the inertial confinement time can be estimated $\tau = R(m_i/2T)^{1/2}$. These considerations lead to a compression ratio criterion as a function of atomic number Z and drive current I :

$$R_0/R = \frac{3^{5/2} m_e^{3/2} c^4 \hbar}{8 m_p^{1/2} e^6 n_0^{1/2}} \frac{(1+Z)T^{3/2}}{A^{1/2} Z^3 I} = 276 \frac{(1+Z)T^{3/2}}{A^{1/2} Z^3 I}$$

for T in keV and I in MA. For pure D-T ($A=2.5$, $Z=1$) and $I=40 \text{ MA}$, the required compression ratio exceeds 275, which is forbiddingly high. However, for carbon ($A=12$, $Z=6$), the ratio must merely exceed 2. As we shall see below, complex loads can be devised which take advantage of these considerations.

In order to check these estimates in a more detailed manner, we have performed a series of simulations with a radiation-hydrodynamics model. Four sets of simulations were performed: (1) a single shell of D-T for a 20, 40 and 60 MA driver, (2) a single shell of D-T at 60 MA for three different masses, (3) an inner shell of D-T and a massive outer CH shell at 40 and 60 MA, (4) the same D-T/CH configuration with a B_z interlayer at 40 and 60 MA. The initial conditions for these simulations are summarized in Table 1, which describes the mass, composition, shell configuration and maximum driving current for each case.

Table 1: Initial configurations for D-T Z-pinch implosions

Configuration	Mass DT	Mass CH	Current	$B_z(t=0)$	neutron Yield		
D-T shell	60abb	0.015g	60 MA	0.00 MG	6.27×10^{17}	<div style="text-align: center;"> $2R_0 = 4 \text{ cm}$  DT </div>	
	60bbb	0.030g	60 MA		1.54×10^{18}		
	60cbb	0.060g	60 MA		1.30×10^{18}		
	40bbb	0.030g	40 MA		2.82×10^{17}		
	20bbb	0.030g	20 MA		6.43×10^{14}		
D-T shell + CH pusher	6206w	0.0093g	0.085g	60 MA	0.00 MG	2.32×10^{18}	<div style="text-align: center;">  DT CH </div>
	6206r	0.0093g	0.085g	40 MA		5.85×10^{17}	
D-T shell + CH pusher + B_z interlayer	60cbb	0.0093g	0.085g	60 MA	0.05 MG	5.86×10^{18}	<div style="text-align: center;">  Bz </div>
	6206b	0.0046g	0.043g	40 MA	0.05 MG	9.84×10^{17}	

2. MODEL

The ionic populations in the plasmas are characterized by sets of atomic rate equations, linking each of the atomic levels included in the models. The rate coefficients that are used to calculate the populating and depopulating processes are calculated using various scattering techniques and the methods used in calculating the corresponding rate coefficients are summarized elsewhere³.

Radiation emission from the plasma and its opacity are dependent on the local atomic-level population densities. Except for optically thin plasmas, however, the level populations depend on the radiation field, since optical pumping via photoionization and photoexcitation can produce significant population redistribution. Thus, the ionization and radiation transport processes are strongly coupled and must be solved self-consistently. In this model, an iterative procedure⁴ was used, where level populations are calculated using the radiation field from the previous iteration, then using these populations to calculate a new radiation field until convergence is reached.

Detailed atomic models were employed for the materials used in this study. The atomic model for carbon contains a sufficient number of excited levels distributed throughout the various ionized states to adequately describe the energetics and diagnostics. The models for D and T consist of the ground states and excited levels up through $N=5$. Ionization lowering was accounted for by means of an ion sphere model; the bound-free radiation was limited from states which merge with the continuum. Radiation transport was carried out using a probability-of-escape formalism which is described elsewhere⁵.

The dynamics of the radially imploding Z-pinch plasma were calculated using a one-dimensional multi-zone non-LTE radiation-magnetohydrodynamics code, DZAPP⁶, which uses a transmission line circuit model to represent the driving generator. The thermonuclear burn was calculated using rates from Glasstone and Lovberg⁷, and a diffusion model was used for the transport of the α -particles. The diffusion equation for the α -particle energy density takes the form

$$\begin{aligned} dE_\alpha/dt &= (1 - \gamma)E_\alpha(\nabla \cdot \vec{v}) + \nabla \cdot (D \nabla E_\alpha) + S - 2\nu_e E_\alpha \\ D &= \frac{Q/(\nu_e m_i)}{(9 + \Omega_i^2/\nu_e^2)} \\ \nu_e &= \frac{n\Lambda Z^2(m_e/m_i)}{(3.44 \times 10^5 T_e^{3/2})} \end{aligned}$$

where $Q = 3.52 \text{ MeV}$. The α -particle source term is given by $S = -Qd[T]/dt$, where $[T]$ is the local tritium concentration (we assume that $[D] = [T]$). This treatment takes the local transverse magnetic field into account via the term involving the ion cyclotron frequency $\Omega_i = ZeB_\perp/m_i c$ in the diffusion coefficient D . Axial electron energy losses were not included in this study; however, we have verified that these can be neglected for sufficiently long pinches.

3. RESULTS

- **Simple D-T Shell with different drivers:** The first set of simulations involved pure D-T shells having the same mass, imploded with different peak currents. Thin shells of D-T with total mass 0.030 g were imploded with peak currents of 20, 40 and 60 MA. The resulting implosion histories are given in Figs. 1-3. In each figure, the ion temperature, plasma density, α -particle production rate, and α -particle deposition rate are shown as a function of radius [cm] and time [μs]. The contours near the time of peak implosion (and α -particle production) are shown; these times decrease with increasing current. A logarithmic scale is used for each variable, and the scale is indicated to the right of each plot. For the 20 MA case, the peak

DT-20MA-b5b

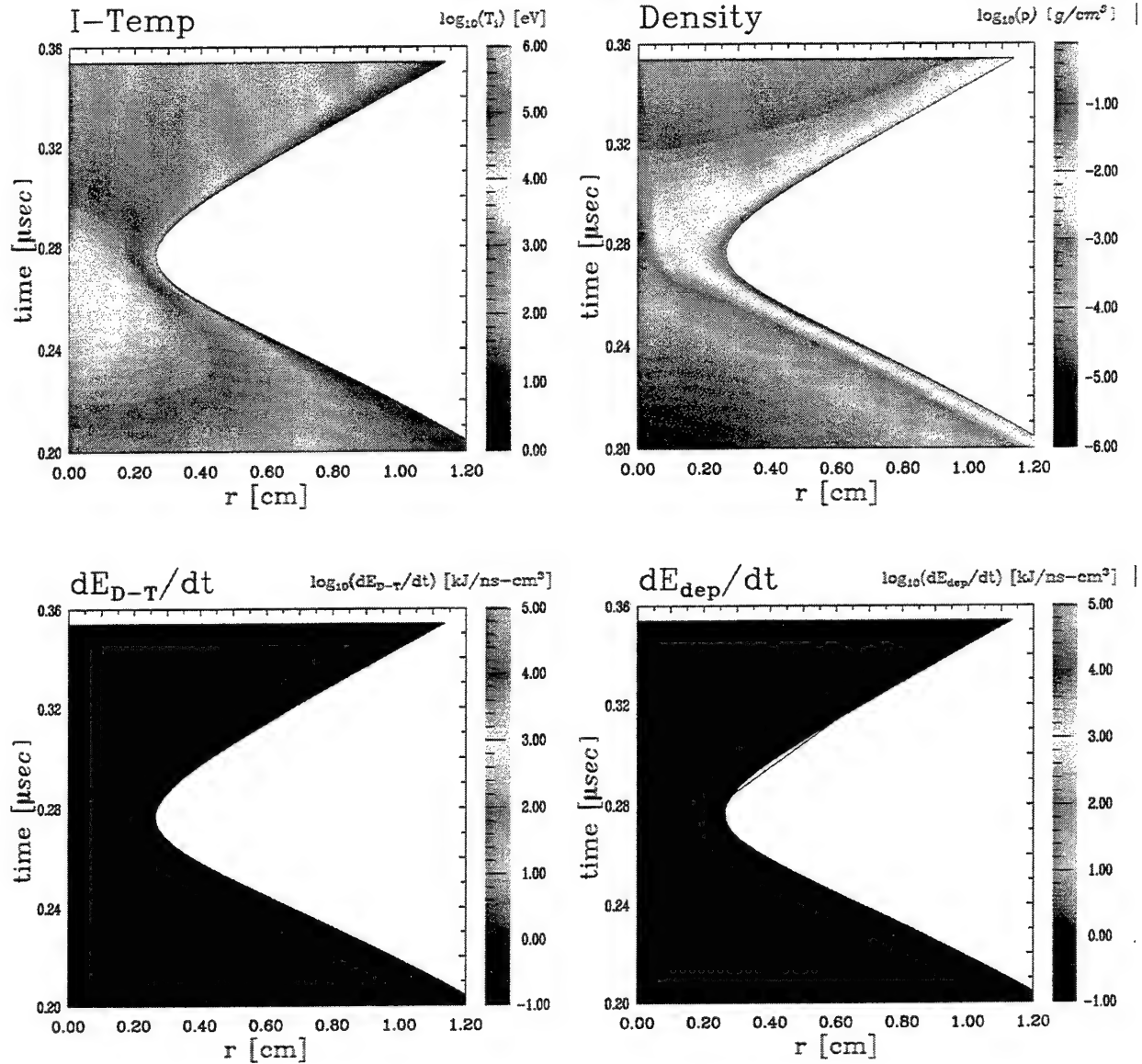


Figure 1. Implosion history of a D-T plasma with a 20 MA drive current. Contours of ion temperature, mass density, α -particle production, and α -particle deposition are plotted as functions of radius [cm] and time [μ sec]. The (logarithmic) values are indicated in the legend to the right of each plot. The times shown (0.20-0.36 μ s) correspond to peak compression and heating during the bounce phase of the implosion.

DT-40MA-bbb

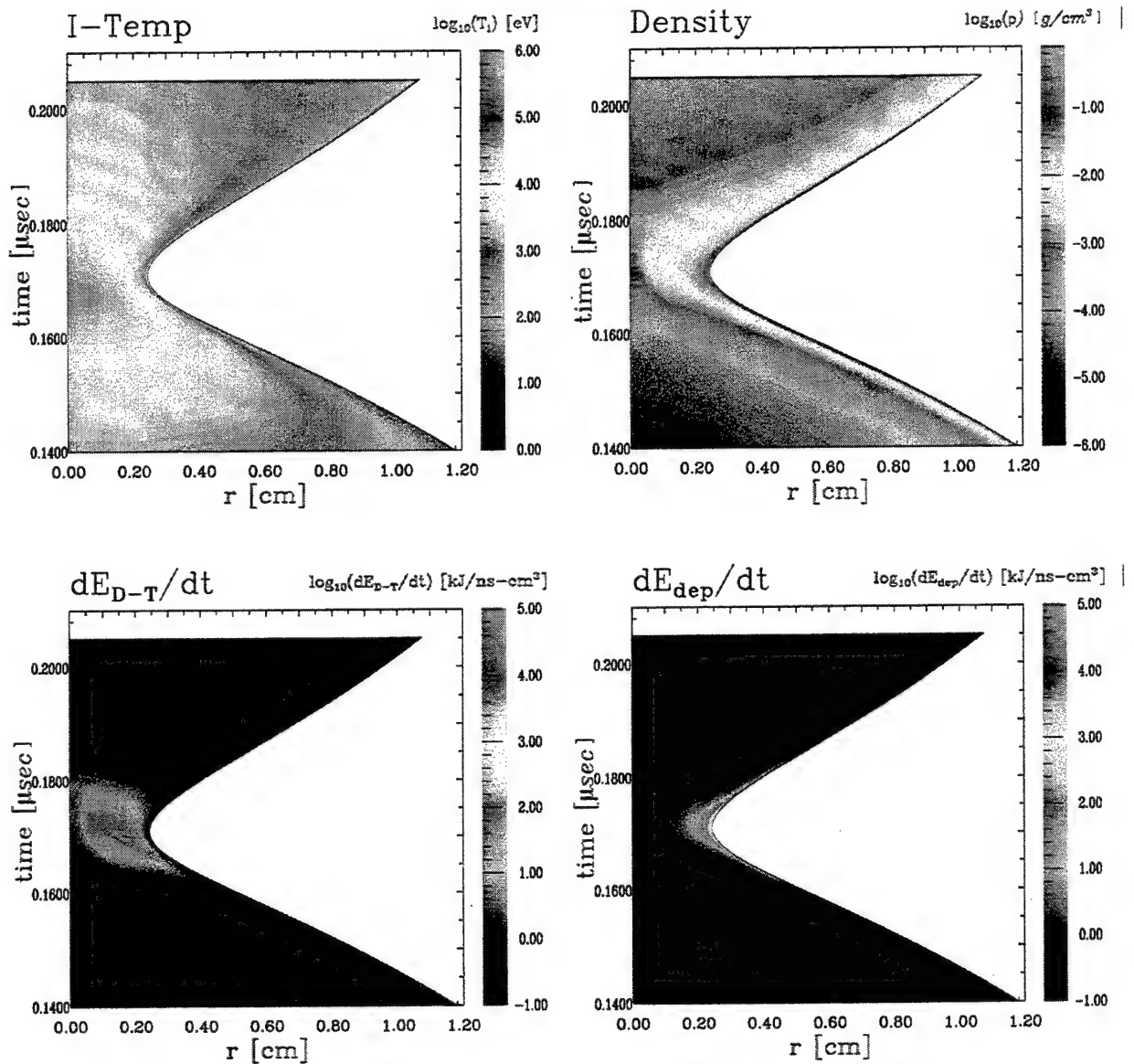


Figure 2. Implosion history of a D-T plasma with a 40 MA drive current. Contours of ion temperature, mass density, α -particle production, and α -particle deposition are plotted as functions of radius [cm] and time [μsec]. The times shown (0.14-0.22 μs) correspond to peak compression and heating during the bounce phase of the implosion.

DT-60MA-bbb

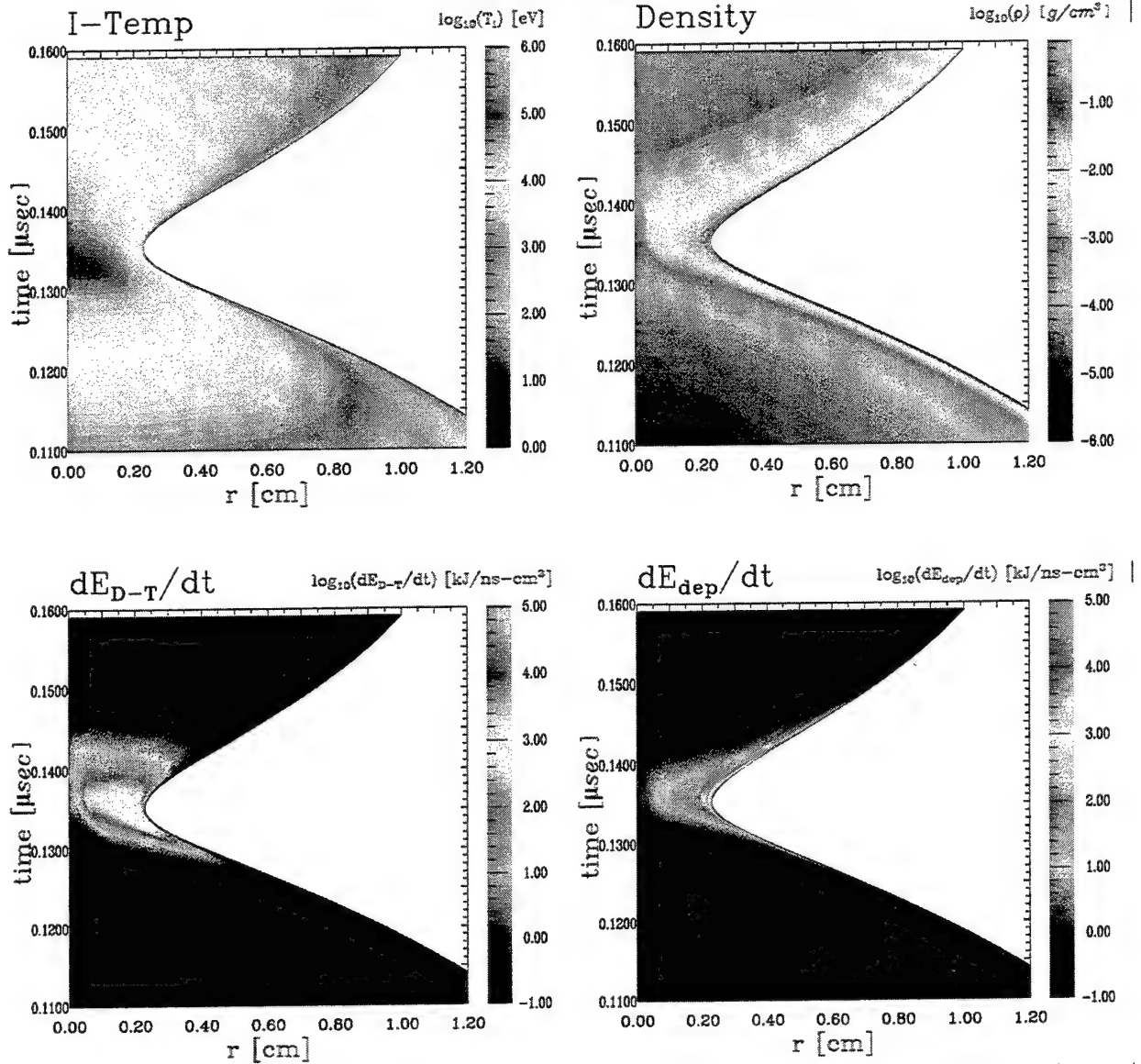


Figure 3. Implosion history of a D-T plasma with a 60 MA drive current. Contours of ion temperature, mass density, α -particle production, and α -particle deposition are plotted as functions of radius [cm] and time [μsec]. The times shown (0.11-0.16 μs) correspond to peak compression and heating during the bounce phase of the implosion.

ion temperature is somewhat less than 10 keV, and the α -particle production (and deposition) is negligible. For the 40 MA case, the peak ion temperature exceeds 30 keV and the pinch is a little tighter; the α -particles are produced within a few nanoseconds around 170 ns (peak implosion). Maximum production is centered near $r = 0.17\text{ cm}$, where the ions are still above 10 keV and the density is fairly high. At smaller radii, the density becomes substantially smaller; at larger radii, the temperature drops. In contrast, the α -particle deposition occurs mostly near the outer edge of the plasma, where the density is the highest. For the 60 MA case, peak ion temperature approaches 100 keV, and strong α -particle production occurs (near peak implosion) at a somewhat larger radius: since the ions are substantially hotter, and the fusion cross-section does not increase very rapidly above 20 keV, efficient burn is possible at higher densities, even though the temperatures are substantially reduced from peak values. Again, the deposition occurs mostly in the very dense outer layer of D-T. The total α -particle yield (equal to the neutron yield) is given in Table 1 for these three cases. The yields for the 20, 40 and 60 MA cases are 6.43×10^{14} , 2.82×10^{17} and 1.54×10^{18} , respectively.

- **Simple D-T Shell with different masses:** For an optimized yield, the mass must be made larger as the drive current increases. In the preceding series of simulations, the masses were held constant as the drive current was varied; this was done to simplify the analysis of the results. The mass for the 60 MA case was chosen to be near the optimum value for burn; to verify this choice, a series of 60 MA simulations was performed with different total masses: 0.015, 0.030 and 0.060 g. The details of the simulations will not be included in this report; however, the α -particle yields are of interest. From low to high mass, the α (neutron) yields were: 6.27×10^{17} , 1.54×10^{18} , and 1.30×10^{17} . Thus, the intermediate mass (0.030g) is close to the optimum value for this (60 MA) D-T configuration.

- **D-T Shell with CH Pusher:** In the simple D-T implosions, the thermonuclear burn is inefficient, even at the highest currents. The ion temperature, which approaches 100 keV for the 60 MA case, is certainly sufficient to provide nearly optimum D-T reaction cross-sections. Unfortunately, the plasma density is not very high in the hottest regions. Also, the plasma bounces, quickly reducing the temperature and density; the D-T becomes too cool for fusion after only a few nanoseconds. A mechanism which could delay the bounce, even by a few nanoseconds, would likely improve the burn efficiency. An outer shell of CH was added to the D-T load, as shown in Table 1. It was hoped that the inertia of this surrounding plasma could help to contain the D-T. Several mass ratios were tried; we will present results with the CH/DT mass ratio slightly less than 10. Simulations for 40 and 60 MA were performed for this double

shell configuration. The implosion history for the 60 MA case is shown in Fig. 4; one complete bounce and the beginning of a second are shown. The initial distribution of mass in the two shells can be seen in the density plot. The D-T plasma is seen to be completely oblivious to the implosion until about 150 ns, when the CH shell crashes onto it. The situation near the first bounce is given in Fig. 5. Higher D-T densities are achieved in the hottest part of the pinch compared with the pure D-T implosion, but the peak ion temperature is somewhat reduced (to about 50 keV). As anticipated, the bounce is less rapid; the result is a modest (approximately 50%) increase in neutron yield, as seen in Table 1. For a 40 MA driver (Fig. 6), the peak ion temperature is reduced to about 20 keV, and the D-T density is slightly less in the hot region. The region of α -particle production is substantially smaller (confined to a region near the axis) than the 60 MA case. However, the bounce is even slower. This is because the mass was unchanged from the 60 MA case; inertial forces are correspondingly more effective with a reduced drive current. The neutron yield is about one-fourth of the 60 MA yield, as seen in Table 1.

- D-T Shell with CH Pusher and B_z Interlayer:** The most complex (and most successful) series of simulations involved concentric D-T and CH shells (as in the previous section) separated by a B_z interlayer. The axial magnetic field is embedded in the plasma at time $t=0$, such that it is uniform between the D-T and CH shells and zero elsewhere. It may be difficult to produce this exact situation experimentally, but it has been shown, for example, that such a field configuration can be established between two wire arrays if they are twisted slightly in opposite directions⁸ (Fig. 7). (It has been pointed out to us, however, that natural tritium decay makes cryogenic D-T wires impractical.) The initial magnitude of the B_z interlayer was varied over a fairly large range, and it was found that (a) large values (i.e. B_z approaching a megagauss) resulted in a larger minimum radius and reduced neutron yields, (b) small values (i.e. B_z substantially smaller than 50 kilogauss) gave results similar to the zero- B_z limit, (c) values of B_z near about 50 kilogauss gave the best yields. We will present results for $B_z(t=0) \sim 50kG$, for peak currents of 40 and 60 MA. In all cases, as the implosion progresses, the axial field diffuses into (and eventually through) the D-T and CH shells. In addition, when the CH shell impinges on the underlying D-T plasma, the B_z interlayer is compressed until it is comparable in magnitude to the azimuthal field B_θ driving the implosion. Thus, the B_z interlayer ultimately becomes quite thin. The pinch histories near peak implosion for the 60 and 40 MA cases are shown in Figs. 8 and 9. At 60 MA, the ion temperature exceeds 100 keV on the axis near 160 ns. The D-T mass density peaks a little later (on axis), at about 165 ns; there is strong D-T burn at this time extending over about a millimeter. The CH plasma

DT-60MA-BZq6qz

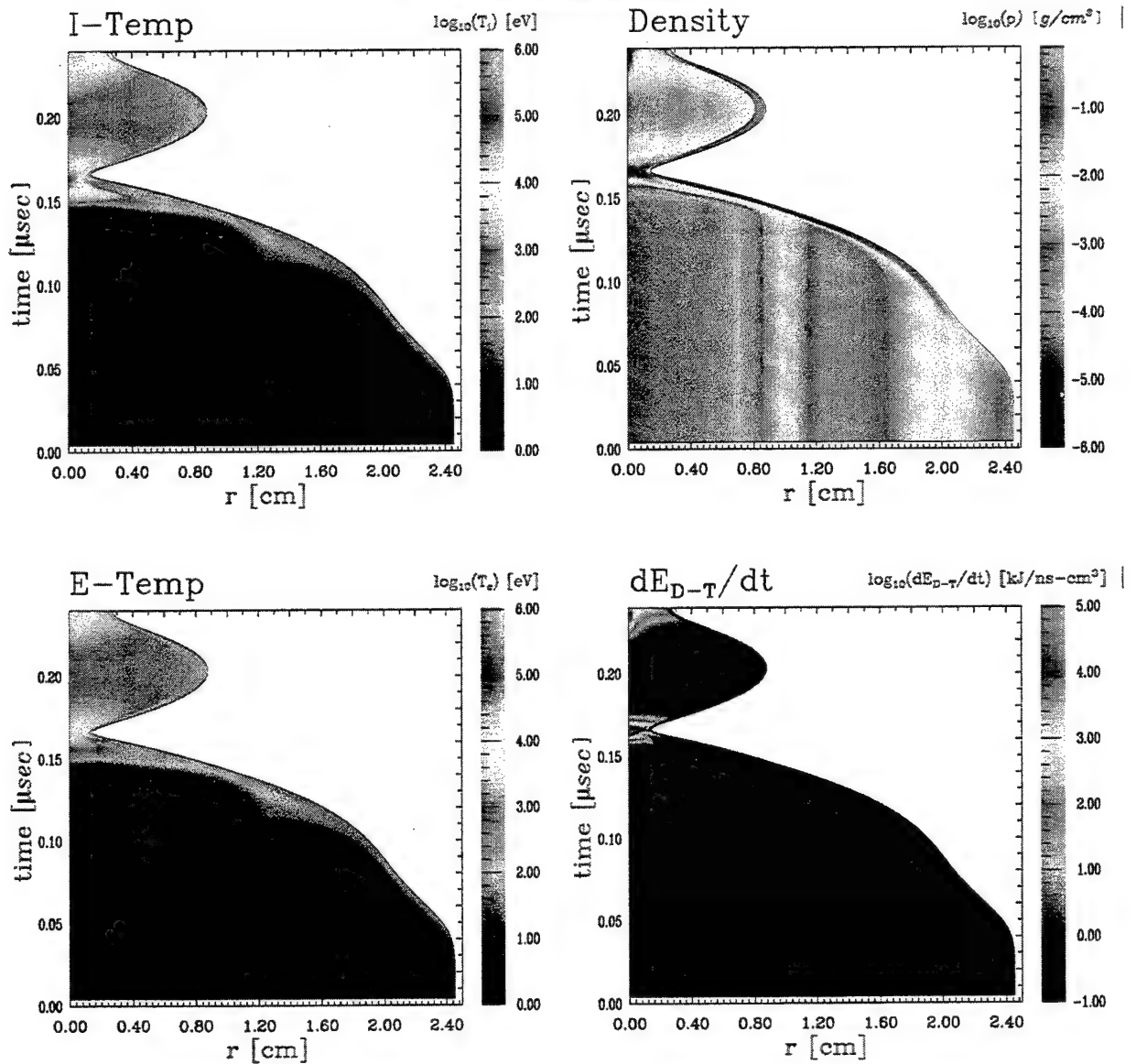


Figure 4. Implosion history of a D-T plasma with a pusher. A CH outer shell is imploded onto a D-T inner shell with a 60 MA driver. Contours of ion and electron temperature, mass density, and α -particle production are plotted as functions of radius [cm] and time [μ sec]. The entire pinch history is shown, from $t=0$ to $t=240$ ns.

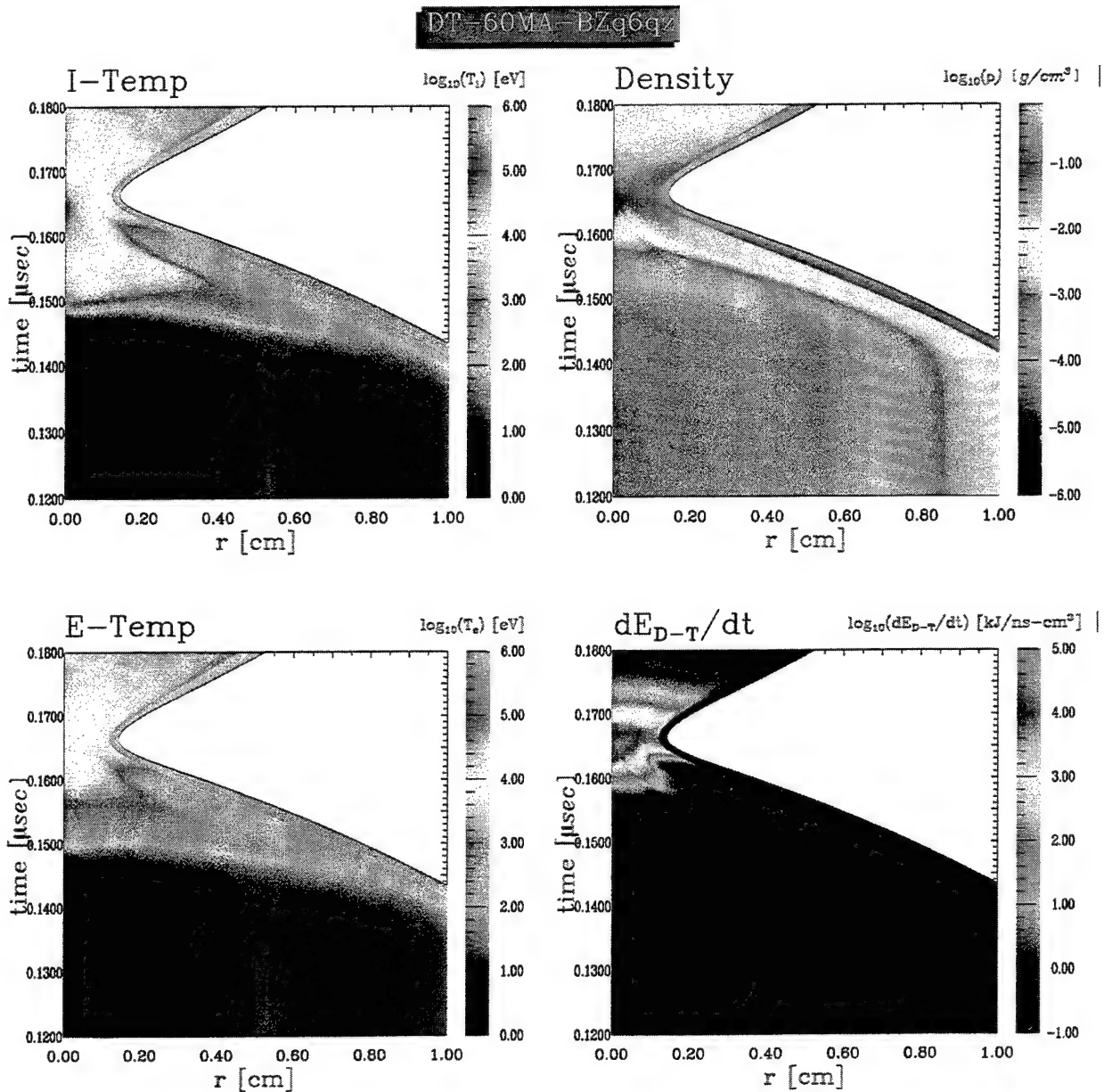


Figure 5. Implosion history of a D-T plasma with a pusher. A CH outer shell is imploded onto a D-T inner shell with a 60 MA driver. Contours of ion and electron temperature, mass density, and α -particle production are plotted as functions of radius [cm] and time [μsec]. The times shown (0.12-0.18 μs) correspond to peak compression and heating during the bounce phase of the implosion.

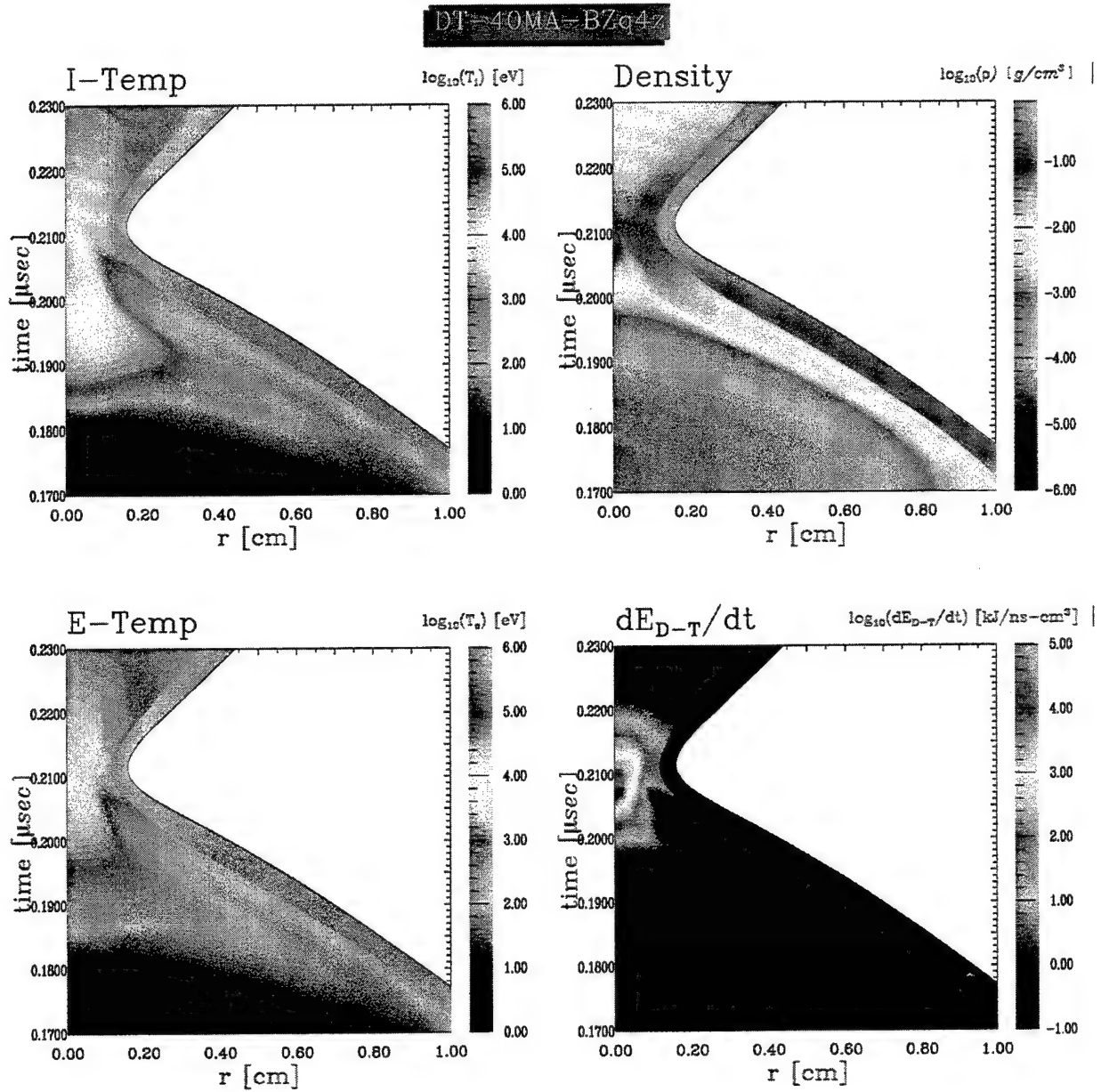


Figure 6. Implosion history of a D-T plasma with a pusher. A CH outer shell is imploded onto a D-T inner shell with a 40 MA driver. The times shown (0.17-0.23 μ s) correspond to peak compression and heating during the bounce phase of the implosion.

(about 90% of the mass) is confined to a very narrow and highly compressed region at the outer edge of the pinch. The ion and electron temperatures in the CH plasma remain about 100 eV during the bounce phase. From Table 1, it can be seen that 5.86×10^{18} neutrons (α -particles) are produced. This is about 2.5 times the number produced without the B_z interlayer. For the 40 MA case, we reduced both the D-T and the CH masses by a factor of two to compensate for the decreased drive current. It was thought that the decreased mass would produce a more optimized implosion and burn. The result is shown in Fig. 9. the peak ion temperature is about 50 keV at 178 ns, and the peak density is about 0.05 g/cm^3 at about the same time. The yield is 9.84×10^{18} neutrons, about 1.68 times the yield without the interlayer.

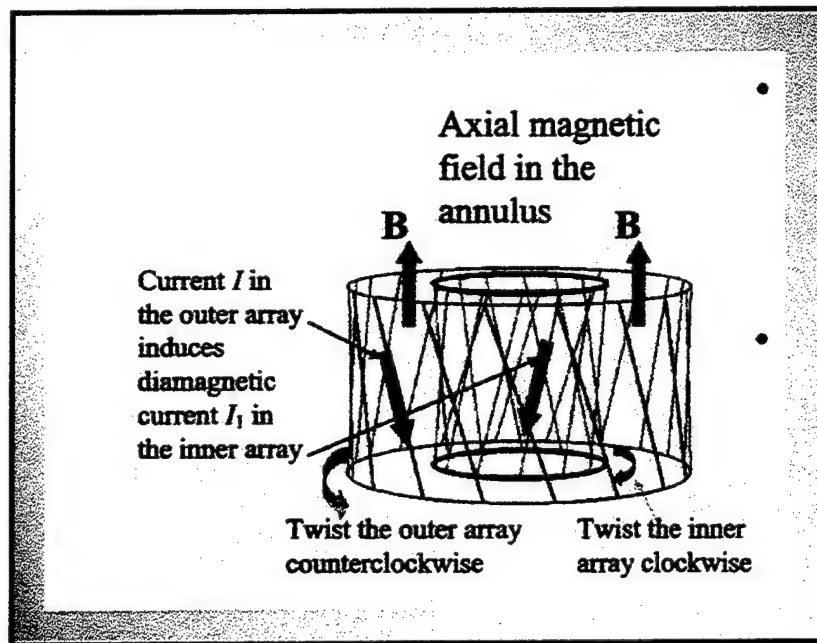


Fig. 7: Method of producing B_z interlayer with concentric twisted wire arrays.

DT-60MA-BZq6b

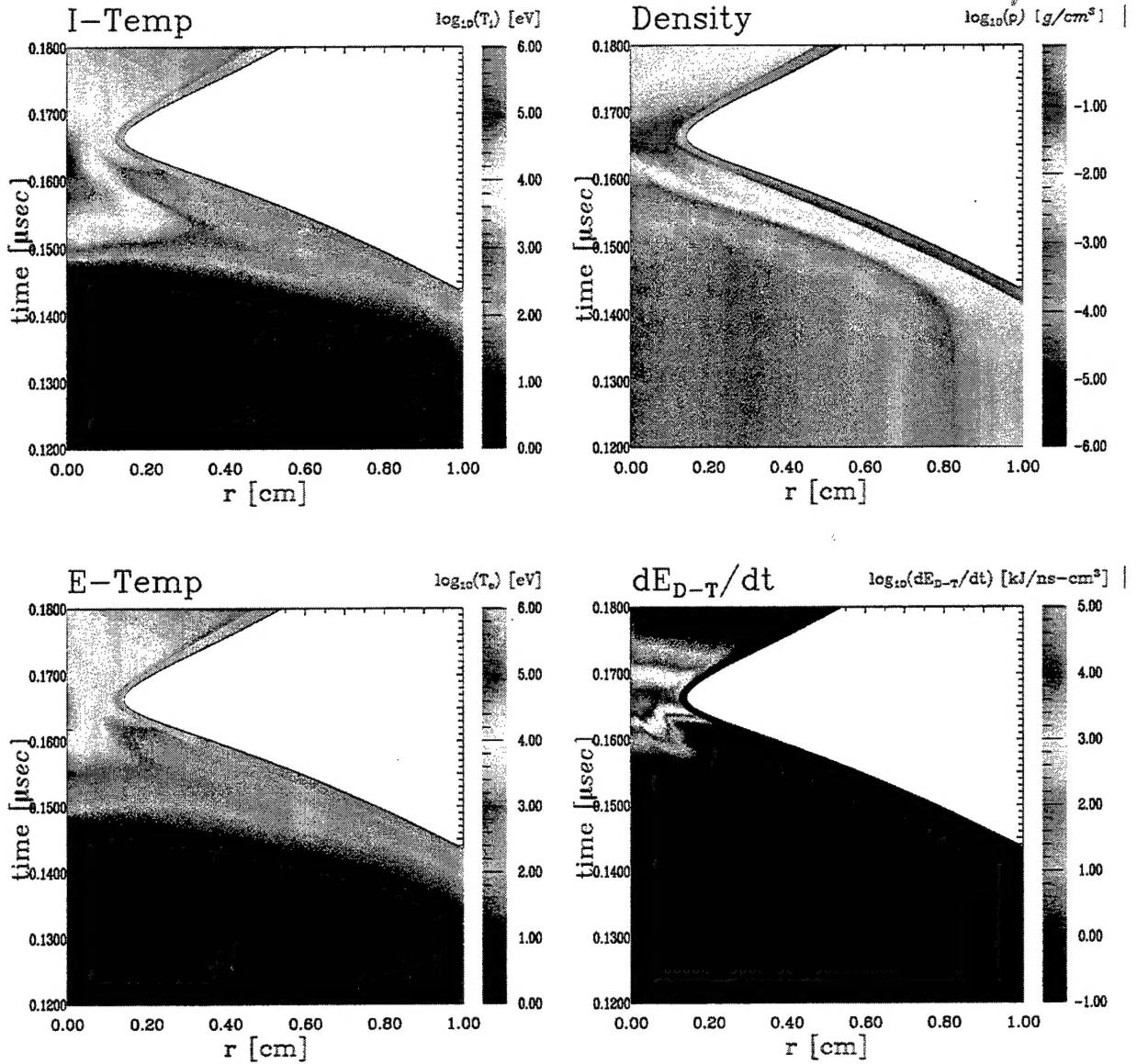


Figure 8. Implosion history of a D-T plasma with a pusher and B_z interlayer. A CH outer shell is imploded onto a D-T inner shell with a 60 MA driver. Contours of ion and electron temperature, mass density, and α -particle production are plotted as functions of radius [cm] and time [μsec]. The times shown (0.12-0.18 μs) correspond to peak compression and heating during the bounce phase of the implosion.

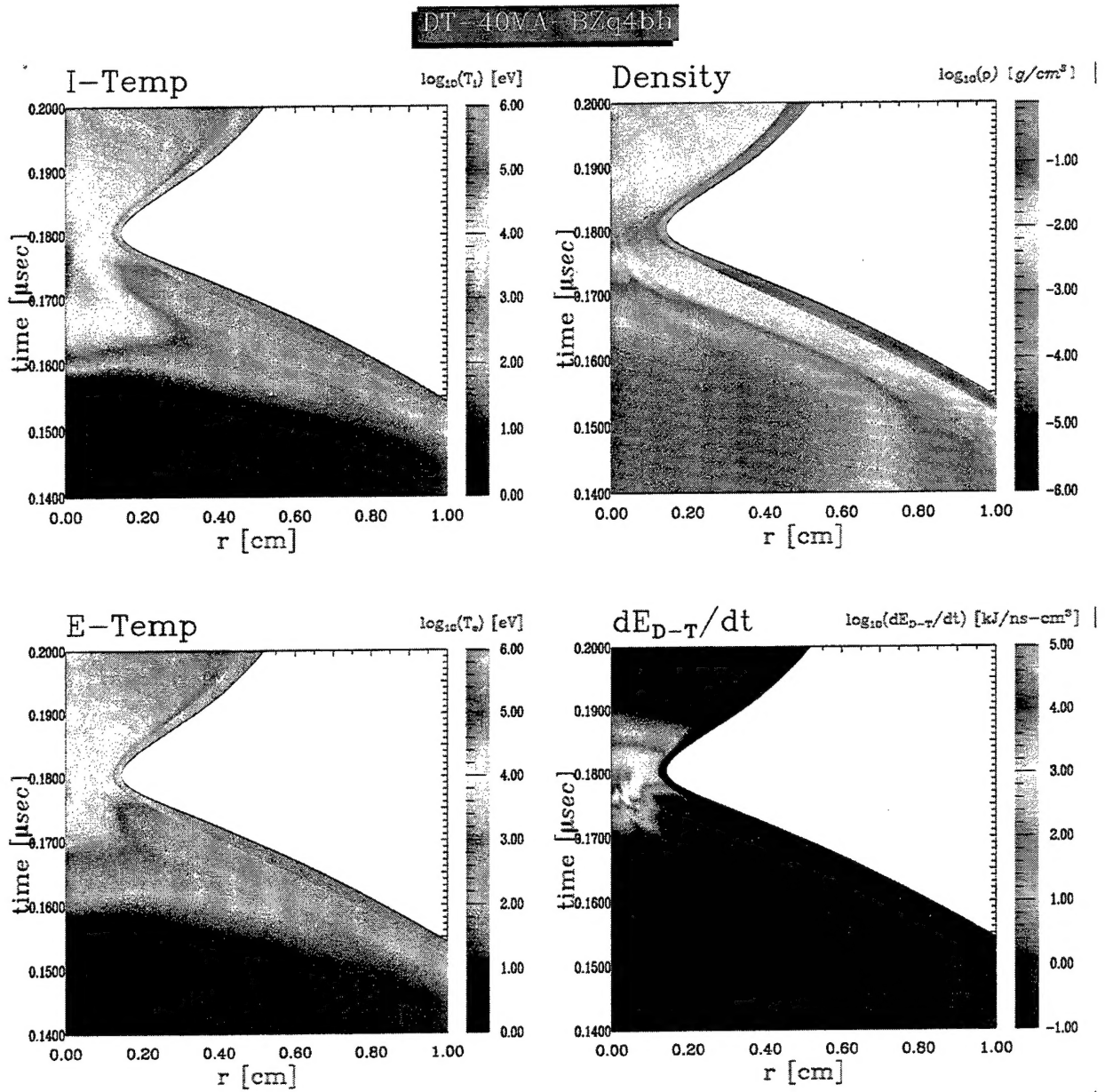


Figure 9. Implosion history of a D-T plasma with a pusher and a B_z interlayer. A CH outer shell is imploded onto a D-T inner shell with a 40 MA driver. The times shown (0.14-0.20 μ s) correspond to peak compression and heating during the bounce phase of the implosion.

4. CONCLUSIONS

We have looked at a number of configurations which might be employed to produce D-T fusion in proposed Z-pinch devices. Even the simplest configuration was capable of yielding in excess of 10^{18} neutrons at 60 MA. We have demonstrated that high currents ($I \simeq 40$ MA) reduce α -particle losses, but that they are not necessarily deposited where they will do the most good (in terms of increasing the burn fraction). The α -particle deposition occurs mostly in cool, dense plasma near the outer edge of the pinch. D-T burn in these devices seems to be limited more by density (and the rapidity of the bounce) than by the ion temperature. At the highest currents, it was easy to obtain 100 keV ions near the axis. The yield was improved with a massive CH pusher. It was improved still further when an axial magnetic interlayer was introduced. The magnitude of the initial B_z was critical, however; yields were degraded when the field was too large or too small.

ACKNOWLEDGMENTS

We would like to thank Dr. P. Kepple for making the atomic database available, Dr. R. Terry for his insights into twisted wire cages, and to Dr. J. Sethian for useful discussions concerning cryogenic D-T. This work was supported by DTRA.

REFERENCES

1. S. M. Gol'berg et al., "Compression, heating and fusion in Megagauss Z-Q pinch systems", in *Dense Z-Pinches*, ed. N.R. Periera, J. Davis and N. Rostoker (AIP, NY, 1989).
2. C. Deeney et al., "Enhancement of X-ray Power from a Z-Pinch Using Nested-Wire Arrays", *Phys. Rev. Lett.* **81**, 4883 (1998).
3. D. Duston, R. W. Clark, J. Davis and J. P. Apruzese, *Phys. Rev. A* **27**, 1441 (1983).
4. J. P. Apruzese, J. Davis, D. Duston and R. W. Clark, *Phys. Rev. A* **29**, 246 (1984).
5. J. P. Apruzese, *J. Quant. Spect. Rad. Transf.* **34**, 447 (1985).
6. J. Davis, J. Giuliani, Jr., M. Mulbrandon, *Phys. Plasmas* **2**, 1766 (1995).
7. S. Glasstone and R. H. Lovberg, in "Controlled Thermonuclear Reactions", (Van Nostrand, NY, 1960), Chapt. 2.
8. R. E. Terry, (private communication).